SELF-ASPIRATED VORTEX GENERATOR JET APPLICATION FOR PROPELLER BOUNDARY LAYER SEPARATION SUPPRESSION

By

ANDREW C. BELLCOCK

Bachelor of Science in Mechanical Engineering

Oklahoma Christian University

Edmond, Oklahoma

2016

Submitted to the Faculty of the
Graduate College of the
Oklahoma State University
in partial fulfillment of
the requirements for
the Degree of
MASTER OF SCIENCE
May, 2018

SELF-ASPIRATED VORTEX GENERATOR JET

APPLICATION FOR PROPELLER

BOUNDARY LAYER SEPARATION SUPPRESSION

Thesis Approved:

Dr. Kurt P. Rouser

Thesis Adviser

Dr. Richard J. Gaeta

Dr. Jamey D. Jacob

ACKNOWLEDGEMENTS

First and foremost, I am thankful to God for creating the complex and beautiful laws of physics and mathematics that make engineering possible, and for creating me with both a capacity and desire to pursue such a worthy endeavor.

Second, I would like to thank Tyler Zimbelman for going through grad school with me. There were many long days (and nights) that I would not have made it through by myself, but studying with you gave me confidence that a master's degree was possible. You have been an encouraging classmate, reliable workout partner, and excellent friend.

I would also like to thank Nick Redmond and Kylar Moody for their work on the CAD models used in this thesis. They gave up time working on their class assignments to make this research possible.

Next I would like to thank Taylor Mitchell for manufacturing all of the test articles used in this study. His expertise in SLA 3D printing prevented many failed prototypes and accelerated the pace of my research significantly.

Real KC and Nick Lucido helped me to set up, calibrate, and run the water tunnel and PIV system. Thank you both for the putting in long nights of work, solving mind-bending calibration problems, and keeping me at least somewhat sane in the process.

Finally, I would like thank my advisor, Dr. Rouser. I wasn't always sure what direction our research was going in, but I always knew that I wanted to follow your lead. You truly care about your students and genuinely enjoy both learning and teaching. You have taught me how to be a scholar, improved my writing abilities tenfold, and imprinted a standard of excellence on me. I am grateful to have spent the last two years under your mentorship.

Name: ANDREW C. BELLCOCK

Date of Degree: MAY, 2018

Title of Study: SELF-ASPIRATED VORTEX GENERATOR JET APPLICATION FOR PROPELLER BOUNDARY LAYER SEPARATION SUPPRESSION

Major Field: MECHANICAL & AEROSPACE ENGINEERING

Abstract: This paper presents a novel propeller flow control design to suppress boundary layer separation for improved propeller performance at low Reynolds number conditions or highly loaded operation. The design includes a series of self-aspirated vortex generator jets across a propeller suction surface, to entrain freestream momentum into the boundary layer flow. The jets are supplied by airflow obtained through inlets arranged on the propeller pressure surface and channeled through the propeller blade. The objective of this jet blowing flow control technique is propeller wake drag reduction and enhanced lift, which leads to greater propeller efficiency. A scaled version of the airfoil cross section at the mid-span of a 10-inch diameter thin electric propeller was manufactured with various vortex generator jet configurations. These 3:1 scale airfoils were evaluated in a closed loop, 30x30x100 centimeter (11.8x11.8x39.8-inch) water tunnel with chord-based Reynolds number ranging from 15,000 to 90,000 and angles of attack ranging from 0° to 30°. Each experimental configuration was characterized by jet penetration distance and separation bubble thickness. The momentum coefficient of each jet configuration was estimated, to allow for comparison with other flow control methods. The study revealed that self-aspirated vortex generator jet arrays located at or just upstream of the separation chord location on a propeller airfoil are effective at creating vortices which suppress boundary layer separation under certain flow conditions.

TABLE OF CONTENTS

LIST OF TABLES

Table Page

LIST OF FIGURES

Figure Page

Figure Page

Figure Page

Figure Page

Figure Page

Figure Page

1 INTRODUCTION

Propellers, such as those used on small unmanned aircraft systems (sUAS) with diameters less than 12-in, are susceptible to boundary layer flow separation at highly-loaded and/or low Reynolds number operating conditions. Highly loaded conditions may result at take-off, where maximum thrust is required. Additionally, the low forward velocity of the aircraft during this stage of operation increases the relative angle of attack of the blade, potentially causing stall at some speeds. Another flight condition where high loading may occur is during climb/acceleration phases, where the rotational speed is rapidly increased, which increases the relative angle of attack experienced by the blade. Low Reynolds number (Re_c) operation can be associated with low density (ρ) at high altitude, low relative velocity (V_{rel}), small chord (l_c), and/or high viscosity (μ) exhaust flow as shown below. Low V_{rel} results from low flight and/or low rotational velocities. A demand for sUAS to achieve low flight speeds stems from the need to increase sensor resolution when mapping, inspecting, or patrolling an area. Additionally, many missions also require quiet operation, which necessitates propeller tip speeds less than 0.3 Mach, achievable with low rotational speeds. Low Reynolds number flow is more susceptible to separation due to lower momentum. Boundary layer flow separation resulting from either of these conditions

significantly reduces the efficiency of the propeller by decreasing thrust produced, increasing drag, or a combination of the two.

$$Re_c = \frac{\rho V_{rel} l_c}{\mu}$$

Aircraft mission capabilities such as range and endurance are highly sensitive to propeller efficiency. Any reduction in propeller efficiency causes significant reduction in the mission capabilities of the aircraft, which in some cases renders the aircraft incapable of completing certain missions. In order to re-enable the desired mission capabilities of the aircraft, more stored energy can be added to the system either in the form of additional batteries or additional fuel. A more desirable method to maintain mission capabilities is to increase propeller efficiency, rather than add additional stored energy to the aircraft. Such an efficiency increase would not require the redesign of structural systems to support added weight, and therefore are simpler to integrate. Increased propeller efficiency may be accomplished by suppressing boundary layer separation.

Various passive and active flow control methods have been studied in the past for suppressing boundary layer separation on airfoils. Examples of passive flow controls are dimples, protrusions, steps, and surface treatments. These techniques, however, cannot be selectively turned on and off, such that under conditions in which the boundary layer is attached, they may increase drag. Active flow control techniques have the ability to be selectively engaged, making them desirable over a range of operating conditions. However, they do require input power or mass flow, which may overcome any performance benefits. Further, the manufacturing difficulty is increased because electricity or high-pressure air must be delivered to the rotating propeller. Examples of active flow control techniques include: plasma actuators, piezoelectric actuators, and vortex generator jets (VGJ's) supplied by high pressure air.

This study presents the design of several self-aspirated vortex generator jet (SAVGJ) arrays integrated into small UAS propellers. The goal of this study is to determine the effectiveness of

certain self-aspirated VGJ configurations at delaying the onset of, decreasing the intensity of, or preventing boundary layer flow separation on a small UAS propeller. To accomplish this, the following objective are set forth:

1. Characterize baseline performance in terms of Reynolds number and advance ratio
2. Characterize the effect of chord location
3. Assess the effectiveness of SAVGJ arrays at suppressing propeller boundary layer separation

In particular, VGJ arrays were integrated into propeller airfoil cross-section models at three different chord locations. Whereas the chord location varied between models, all other VGJ parameters remained constant. Each model was studied using PIV in a water tunnel at various speeds and angles of attack, to simulate different operating conditions which the propeller might experience during a typical UAS mission. The jet penetration distance and separation chord location for each VGJ configuration were measured and compared to a baseline configuration. Further, each VGJ configuration was integrated into an UAS propeller and evaluated on a propeller wind tunnel dynamometer. This experiment provided the thrust and torque measurements at various tunnel speeds and rotational speed settings, which were used to calculate the propeller efficiency at each condition. Results of these experiments revealed that certain configurations of self-aspirated VGJ's create vortices in a 2D flow environment, and have a measurable effect on propeller performance.

2 REVIEW OF LITERATURE

Usage of small UAS is increasing across many industries, including: defense, private security, surveying, pipeline inspection, and search and rescue. Systems are being used to complete tasks such as: mapping, inspecting, or patrolling because of their capacity to accurately and autonomously complete missions with significantly reduced cost. Each industry has a variety of different missions using sUAS, many of which include an extended duration of low-speed flight (less than 40 knots). During these mission legs, the relative angle of attack experienced by the propeller blades can be high causing the flow to separate and the blade to stall. Propeller relative velocity is a function of the freestream velocity (flight speed) and propeller rotational velocity. The ratio of these two velocities is represented by the parameter advance ratio (J), where freestream velocity is V_∞, rotational speed is n, propeller diameter is D, and rotational velocity is (nD) (McCormick, Barnes 1994).

$$J = \frac{V_\infty}{nD}$$

At low flight speeds, the rotational velocity component dominates the relative velocity, causing a small advance ratio. Propellers operating at low advance ratios typically experience a large relative angle of attack (α_{rel}) relative to the blade pitch angle (β), making the propeller susceptible to flow separation, which causes adverse propeller performance.

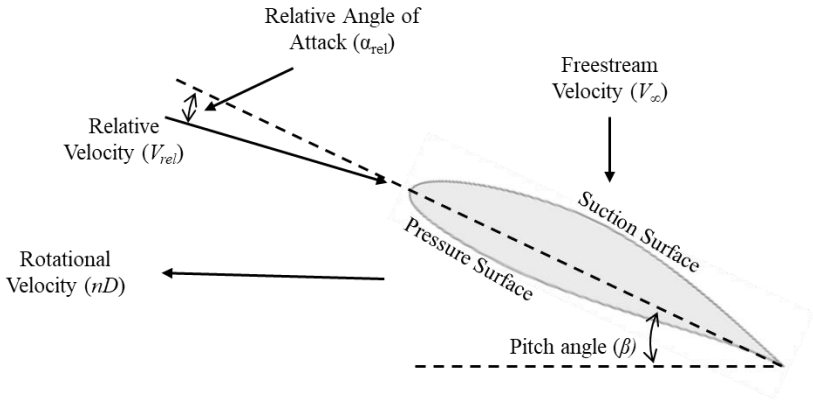

Figure 1. Cross section of propeller with velocities

In order to quantify the effects of flow separation, Propeller Momentum Theory can be used to calculate ideal propeller efficiency ($\eta_{p,i}$). Propeller Momentum Theory assumes the plane of the propeller is an infinitesimally thin disc (referred to as the actuator disc) oriented normal to the flow. Further, this theory assumes that all flow passing through the disc is bounded by a contracting stream tube.

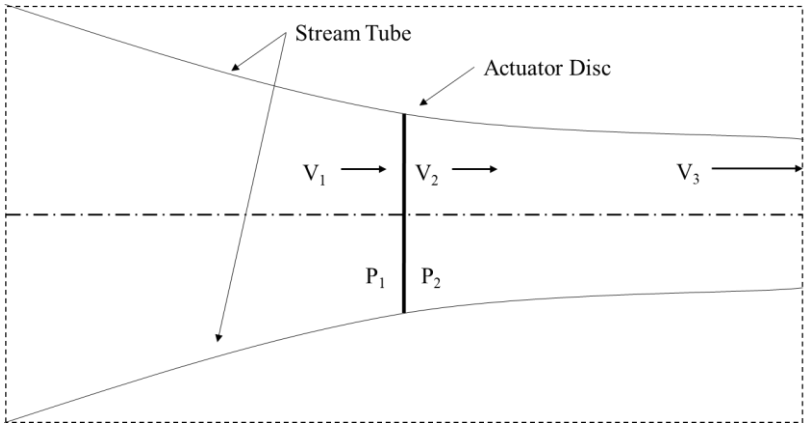

Figure 2. Cross sectional view of idealized flow in propeller momentum theory.

Based on these assumptions, the downstream velocity (V_2) is greater than the upstream velocity (V_1), due to the step change in static pressure produced by the propeller. The difference between these velocities is referred to as the induced velocity (w), which can be used to calculate the

momentum exiting the actuator disc. Ideal propeller efficiency ($\eta_{p,i}$) represents the ratio of momentum entering the actuator disc over momentum exiting the actuator disc. is defined as the momentum entering into the system divided by the momentum exiting the system, where *T* is thrust.

$$\eta_{p,i} = \frac{TV_\infty}{T(V_\infty + w)}$$

Ideal propeller efficiency is the maximum possible theoretical efficiency for the propeller, however it does not consider any of the aerodynamic effects on the blade. Momentum-Blade Element Theory combines the idealized flow shown above in Fig. 1 with an approximate analysis of the propeller airfoil shape. Blade angle pitch angle varies span-wise with increasing radius (*r*) from the centerline. Typical small UAS propellers have a constant pitch (*p*), based on β and *r*, such that the units of pitch are length, indicating the forward distance traveled per revolution.

$$p \equiv 2\pi r * tan\,\beta$$

Whereas, key propeller geometry is defined by pitch and tip diameter, there are three key propeller performance parameters: coefficient of thrust (C_T), coefficient of power (C_P), and propeller efficiency (η_p). All three propeller performance parameters are related to advance ratio.

$$C_T = \frac{T}{\rho n^2 D^4}$$

$$C_P = \frac{T}{\rho n^3 D^5}$$

$$\eta_P = \frac{C_T J}{C_P}$$

Figure 3 shows an example of analytical data for C_T, C_P, and η_p for an Advanced Performance Composites (APC) propeller, having a 10-in diameter and a 5-in constant pitch. The steep drop-off

in propeller efficiency that occurs around an advance ratio of 0.6 is due to flow separation over the suction surface of the propeller.

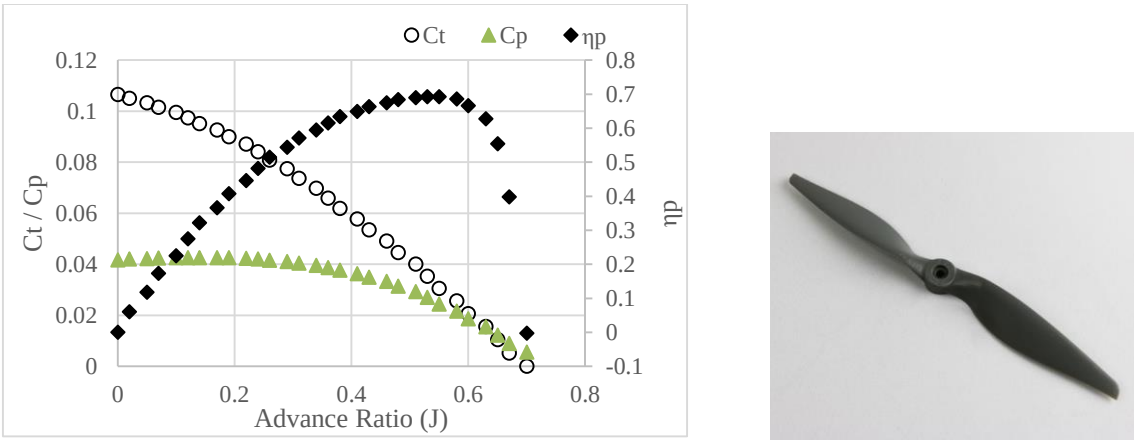

Figure 3. Propeller performance data for APC 10x5e propeller at 5000 rpm.

For low Reynolds numbers (<200,000) as flow over the surface of an airfoil (or propeller) begins to separate, a laminar separation bubble is formed. The laminar boundary layer detaches from the surface due to an adverse pressure gradient, but reattaches downstream due to the turbulent shear layer. The pocket of fluid between the separation location and reattachment point is the laminar separation bubble. As angle of attack changes, the laminar separation bubble can cause hysteresis in the lift (thrust) produced because the drag of an airfoil increases more rapidly before stall with increasing angle of attack than drag decreases after stall with decreasing angle of attack (Gamble, 2009).

Flow control methods to suppress boundary layer separation (BLS) can generally be divided into two categories: active and passive, as aforementioned. Two subcategories include: vortex generators and jet blowing. Passive vortex generators include small shapes applied to an aerodynamic surface. (Lin et al. 1994) studied the use of vortex generators on high lift airfoils using a 3-ft wing in a closed-circuit subsonic wind tunnel operating at M = 0.2. The wing included flaps and a dynamic leading edge, which simulated a highly cambered airfoil when deployed. Small vortex generators (0.18% of chord) were applied to the airfoil suction surface to

mix boundary layer and freestream flows, thus increasing boundary layer momentum to suppress BLS. This technique was proven to delay boundary layer separation

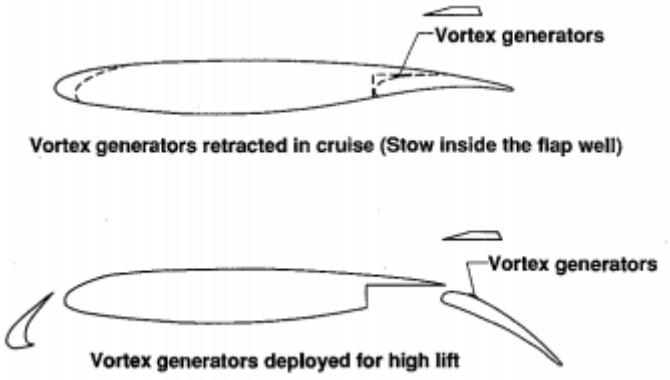

Figure 4. Vortex Generators Applied to High-Lift Airfoil Used as Flap (Lin et al. 1994)

Synthetic jets are another type of passive flow control method. Synthetic jets have a flexible membrane with a small orifice and chamber embedded into a surface. The length of this chamber, along with the modulus of the membrane, are tuned such that certain freestream flow conditions cause the membrane to oscillate, thus producing an unsteady jet into the free stream. This jet promotes mixing of boundary layer and free stream, which has been shown to be effective at suppressing boundary layer separation on wings. Volino and Ashpis (2003) showed synthetic jets to also be effective at suppressing flow separation on low-pressure turbine blades.

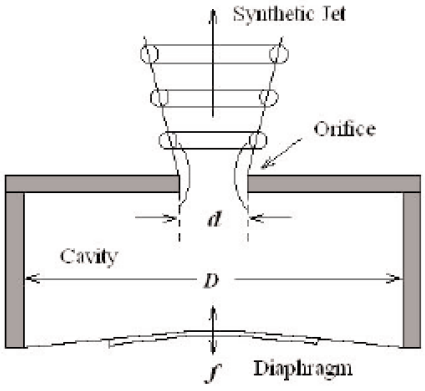

Figure 5. Detail of Synthetic Jet for Boundary Layer Flow Control (Voline and Aspis 2003)

VGJs are an active flow control method that incorporate the effects of vortex generators and jet blowing; however, they also have the added benefit of increasing lift coefficient (C_l). Typical VGJs are driven by a compressed air, thus adding momentum to free stream flow. VGJ's were studied by (Johnston and Nishi, 1990) as a method for controlling flow separation in a turbulent boundary layer. In particular, their study focused on the ability of VGJ's to prevent boundary layer separation in an adverse pressure gradient. A square cross section wind tunnel was used for this experiment where VGJ's were located on the bottom surface of the tunnel with a jet diameter of 0.25-in and a fixed pitch angle of 45° relative to the surface of the tunnel.

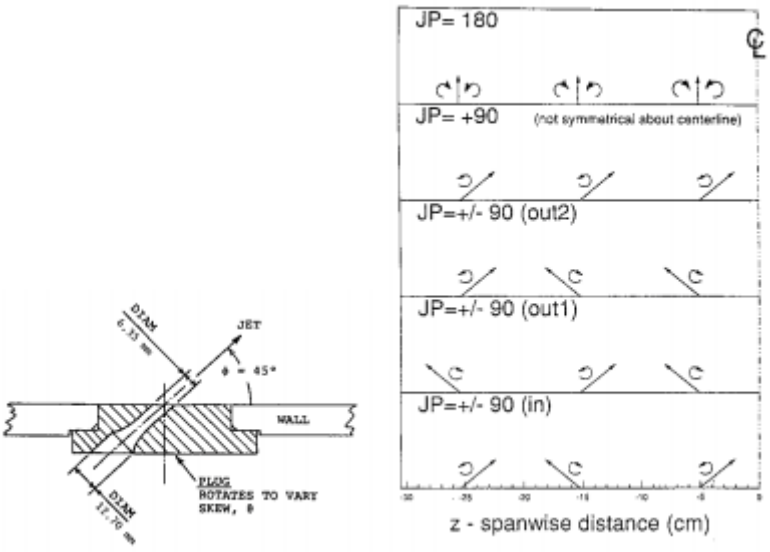

Figure 6. Detail of Skew Angle (left) and Pitch Angle (right) Configurations for VGJ Arrays Studied by Johnston and Nishi

The jets were arranged span-wise with a spacing of 0.40-in center-to-center. Various configurations of skew angles from -90° to 90° relative to the freestream were tested at a mean freestream velocity of 33.6 mph. These tests revealed that jet pairs producing stream-wise counter-rotating vortices cause significant span-wise variations in the separation location. Further, a test was conducted with pitch angle oriented upstream and with no skew angle, which was not

able to prevent boundary layer separation. Finally, each test permutated velocity ratio (*VR*) of the jet velocity to the free stream velocity. Jets with *VR* greater than 0.8 were highly effective at promoting flow reattachment.

Worsop et al. demonstrated that pulsed air jets are significantly more effective at manipulating flow, including boundary layer separation suppression. Their work demonstrated that rapid pulsing (500Hz) achieved using piezoelectric valves created vortices across a range of operating conditions more effectively than steady blowing.

Building on the flat plate boundary layer work, Shaun and Ahmed (2011) examined the use of VGJ's for reducing flow separation on high-lift airfoils. This study examined VGJ arrays with increasing sized orifices placed in close proximity to each other. Each array was located on the suction surface of a NACA 63-421 airfoil and contained four rectangular orifices varying in width from 1.5mm to 4.08 mm, each having 30° pitch and 60° skew angles.

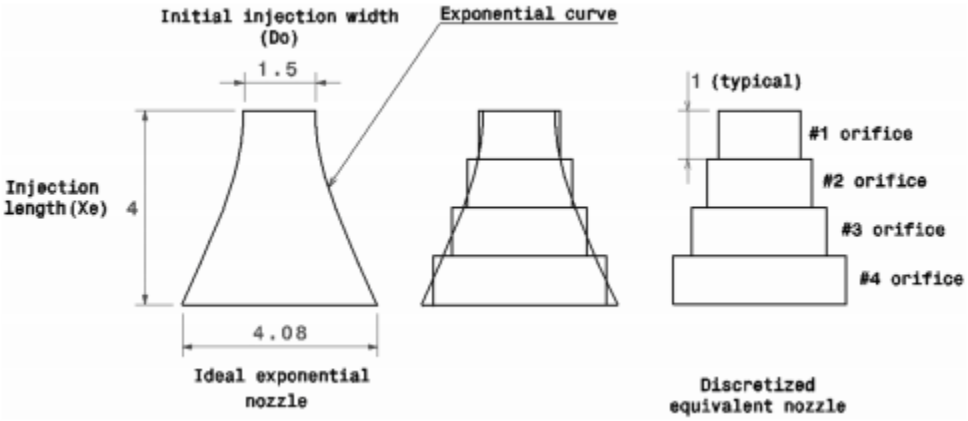

Figure 7. Detail of Discretized Exponential Nozzle (Top View) (Shaun and Ahmed 2011)

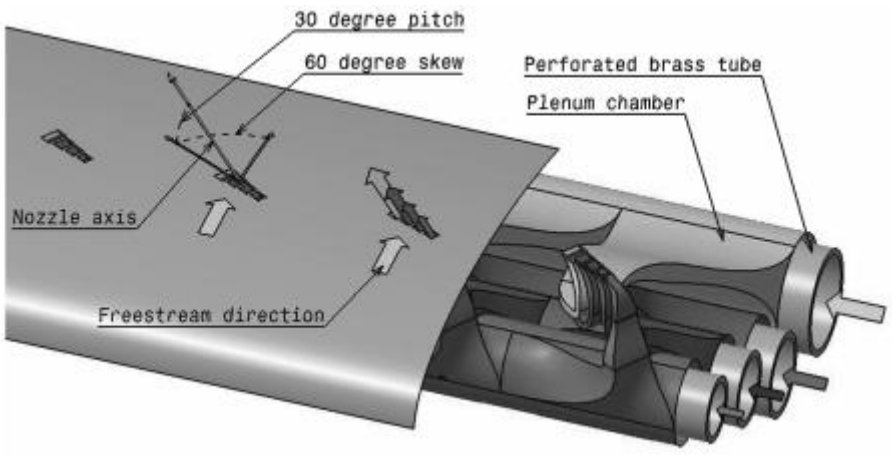

Figure 8. Detail of Discretized Exponential Nozzle VGJ Array and Plenum Chambers (Shaun and Ahmed 2011)

Each orifice was connected to its own plenum, allowing the *VR* to be manipulated independently for each orifice. The 24 arrays were located at 12.5% chord and arranged with span-wise spacing of 1.18-in The 29.1-in span airfoil was equipped end plates to simulate two dimensional flow and placed vertically in a 35.4-in by 47.2-in subsonic wind tunnel at 89.5 mph which produced a Reynolds number of 650k. Further, the exit velocities of each jet were measured using a hotwire. Velocity profiles for each jet in the array were varied using two schemes: 1) variable velocities corresponding to a discretized version of an exponential jet and 2) constant velocity across the entire array. Lift, drag, and momentum coefficients were calculated for each configuration and showed significant increases in $C_{l,max}$ for all configurations, but especially for the two largest constant velocity configurations. Further, these two configurations also significantly delayed stall angle, indicating flow separation. Another performance metric, cost-to-benefit ratio (R_{cb}), was calculated to show the advantage of such a system, where the coefficient of drag (C_d) and coefficient of jet momentum (C_μ) are considered the cost of operating the VGJ.

$$R_{cb} = \frac{C_l}{C_d + C_\mu}$$

For conditions above α=14°, nearly every configuration provided a significant improvement compared to the baseline. The two largest constant velocity configurations indicated no further improvement related to higher jet velocities and demonstrated 30-50% improvement over the baseline configuration. This study revealed that VGJ's significantly improve lift coefficient and suppress flow separation if the jet velocity is great enough.

Prince et al. (2017) applied self-aspirated VGJs to wind turbines in order to increase Cl on the blades, which consequently increased power coefficient for the system. This design utilized passive VGJ's, which included inlets on the lower surface of the blades to collect ram air in order to feed the VGJ's.

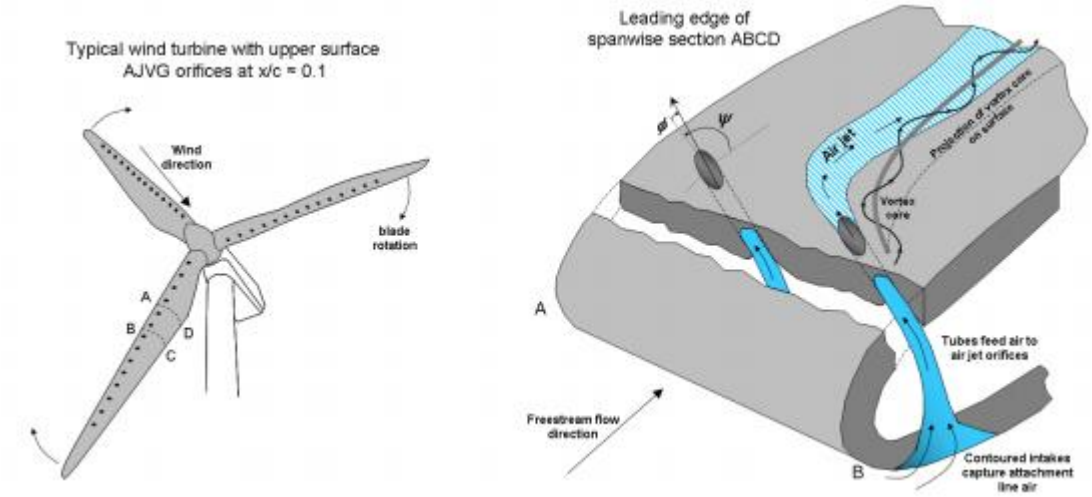

Figure 9. Detail of Passive VGJ for Wind Turbine Applications (Prince et al. 2017)

The 0.079-in diameter jets were located at 17.8% chord and oriented with 30° pitch and 60° skew angles. The 21 VGJ's were evenly spaced 0.60-in apart across the 1.18-ft blade. The turbine was composed of 6 blades and had a diameter of 34.3-in with a 15° twist angle. Wind tunnel tests were conducted from 0-49.5 ft/sec which demonstrated a slight increase in power output and C_p, and delayed blade stall on both acceleration and deceleration for the 0° pitch angle. However, the studied did not consider the effect of varying chord location, as presented here in this study.

In order to quantify the net effect of SAVGJ arrays on propeller performance, dynamometer testing should be conducted to evaluate three parameters: coefficient of thrust (C_T), coefficient of power (C_P), and propeller efficiency (η_p). In particular, the difference between a baseline (unmodified) propeller and a propeller with integrated SAVGJ array should be compared for each parameter. The inclusion of a SAVGJ array should decrease the curvature of peak propeller efficiency, indicating that propeller stall (flow separation) is delayed. The maximum propeller efficiency should have a larger magnitude and occur at a higher advance ratio.

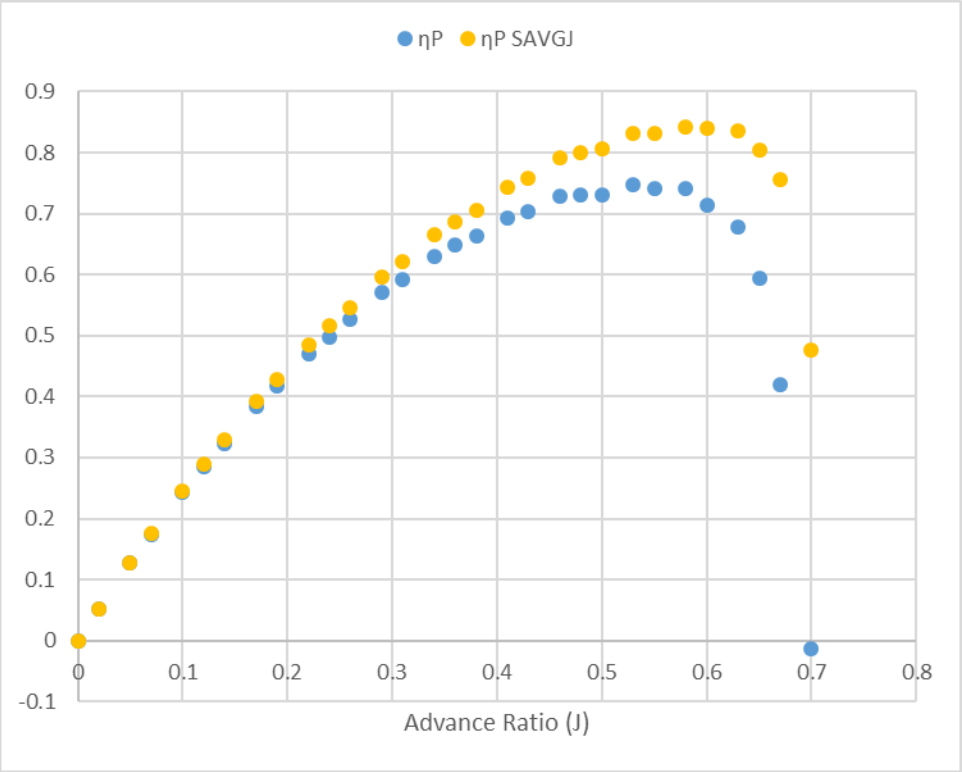

Figure 10. Propeller Performance Curve for Baseline Propeller and Anticipated Propeller Performance Curve for Propeller with SAVGJ Array

3 METHODOLOGY

3.1 Propeller Selection

Many small UAS propulsion systems rely on commercial off-the-shelf components in order to minimize cost. One of the most common hobbyist propeller brands is Advanced Precision Composites (APC), which manufactures propellers ranging in size from 4-in to 27-in in diameter. For this study, a 10-in diameter propeller which produced up to 3.5-lbf of thrust at 10,000-rpm, which is appropriate for a small UAS in either fixed-wing or rotorcraft configuration. In particular, the 10x5 thin electric propeller was selected because its 2-to-1 diameter to pitch ratio, which is typically an available option for all propeller diameters. Further, a propeller of this diameter could easily be manufactured using most 3D printers and could also be tested on a propeller dynamometer inside the Oklahoma State University low speed wind tunnel without risk of wall interactions (wind tunnel discussed in detail later). Additionally, APC provides performance data sheets which detail the expected performance characteristics of their propellers at virtually every flight condition. Further, the University of Illinois propeller database contains experimental data for most APC propellers, including the selected 10x5 thin electric propeller. Baseline propeller performance data from the dynamometer setup can be corroborated by these two sources, making APC an ideal choice for the baseline propeller.

3.2 Flow Control Method Selection:

When considering which flow control method to implement on small UAS propellers, three key factors were considered: manufacturing feasibility, integration feasibility, and potential impact. Manufacturing feasibility pertains to the flow control device itself. Techniques which required complex and/or precise manufacturing were deemed unlikely to be appropriate for application to a propeller because of the high rotational speeds and therefore high stress loading on any device applied to the propeller blades.

Integration feasibility pertains to the simplicity and possibility of integrating the chosen flow control device into the propeller structure. The device must not compromise the structural integrity of the propeller as this could lead to catastrophic failure, which would likely compromise the UAS mission and could present a safety hazard to nearby persons. Further, the device must not add significant weight to the system, because additional weight would likely impair the mission capabilities of the UAS more than the benefit of any propeller flow control system. Finally, any power required by the device must be transmitted to the propeller through the rotating shaft. Examples of power are electricity in the case of plasma actuators and piezoelectric actuators, and high-pressure air in the case of vortex generator jets.

Potential impact is a qualitative comparison that assess the success of a flow control device at suppressing boundary layer separation under conditions similar to what the baseline propeller may experience during certain portions of the UAS' mission. The results of studies of flow control devices on both flat plates and airfoils with similar Reynolds numbers were considered when evaluating the potential impact of various flow control methods for application to small UAS propellers.

Ultimately, an uncommon technique dubbed "self-aspirated vortex generator jets" was selected as the most ideal flow control method for this study. Self-aspirated VGJ's are comprised of three

features: inlets, flow channels, and jets. None of these features have particularly complex geometry and all of them can be manufactured using the propeller blade material, making the manufacturing feasibility very high. In general, the flow channels are relatively small when compared to the chord length, allowing the propeller blade to maintain its structural integrity. Because this technique is self-aspirated, no high-pressure air is required, therefore simplifying integration into the propulsion system and aircraft in general. Integration feasibility is further increased because this technique actually removes weight from the baseline propeller. Finally, the aforementioned study applied self-aspirated VGJ's to a wind turbine and produced significant increases in coefficient of lift (C_L) for high angles of attack, albeit at much higher Reynolds numbers (on the order of 10^6).

One further potential benefit of this technique is that it may self-regulate its actuation, decreasing flow through the jet array when freestream flow is attached to the blade suction surface. This phenomenon may occur because the jet momentum ratio (jet momentum over freestream momentum) is much significantly decreased when the freestream flow is attached. As flow begins to detach, the jet momentum ratio begins to increase, ultimately resulting in a series of span-wise skewed vortices which promote the suppression of boundary layer separation.

3.3 Self-Aspirated Vortex Generator Jet Parameter Selection:

Self-aspirated vortex generator jets have 10 design parameters when applied to propeller blades: number of jets, pitch angle, skew angle, chord location, span location, jet spacing, jet array angle, jet cross-section shape, inlet cross-section shape, and jet area ratio. For this study, an array of four jets was selected in order to localize the effect of the flow control to a particular region of the propeller blade. This was important because the twist of the propeller blade may have a significant effect on the vortices generated by the jets, which could impair the ability to experimentally evaluate various jet configurations.

The jet pitch and skew angles were transferred from a previous self-aspirated vortex generator jet study on wind turbines (Prince et al. 2017). The pitch angle (θ) was set to 30° in order to provide significant jet penetration into the freestream flow, while the jet skew angle (φ) was set to 60° to initiate the creation of a stream-wise vortex. These angles have been shown to produce maximum vorticity (Freestone 1985).

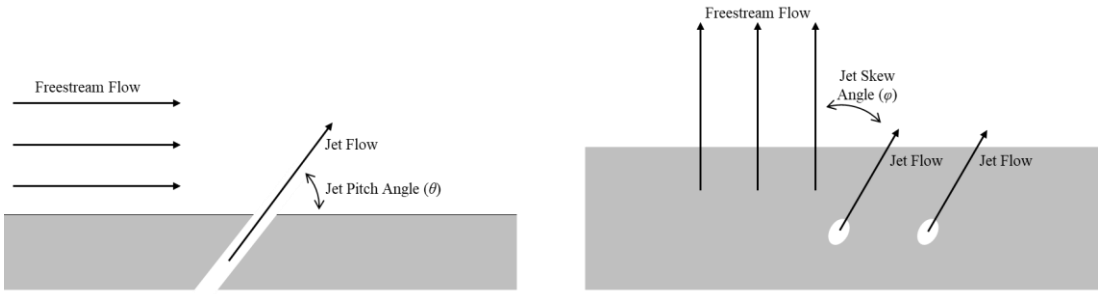

Figure 11. Side view of jet pitch angle (left) and top view of jet skew angle (right)

In the same previous study by Prince et al., the chord location of the jet array was at 12% chord for a NACA 23012C airfoil, which is a modified version of the NACA 23012. While this airfoil is similar to the 50% span cross-section of the APC propeller used in this study, a VGJ location 12% chord is very likely upstream of the flow separation location, which means that attached flow is probably being blown off the blade surface. Consequently, this study evaluates three different chord locations further downstream: 40%, 50%, and 60% of chord length. These locations were chosen to begin parametrically studying the effect of chord location on the effectiveness of self-aspirated VGJ's on a propeller blade.

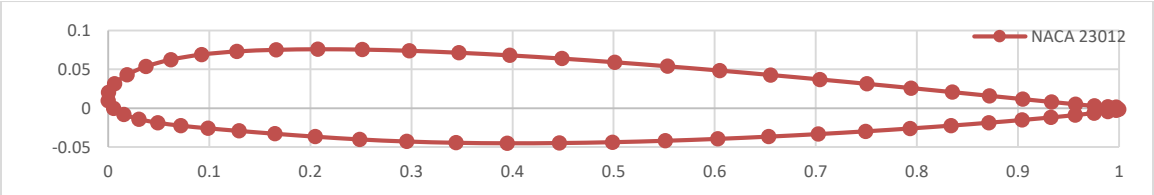

Figure 12. Profile of NACA 23012 Airfoil

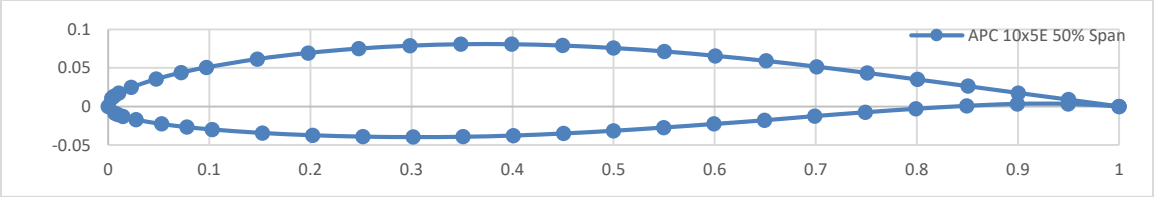

Figure 13. 50% Span Airfoil Cross-Section of APC 10x5E Propeller

Span location of the jet array for this study was set to 50%. While the jet array occupies a range of span locations, it centered around the 50% location, in accordance with notation convention established in previous studies. This location was chosen because it is most likely to have the greatest impact on overall performance. Flow near the blade tips (100% span) is less likely to separate because it has a much higher Reynolds number due to the increased total relative velocity, which is increased by the tangential velocity component of the propeller's rotation. Further, flow near the root of the blade (0% span) produces a very small fraction of the total thrust, therefore any flow control applied to this region of the propeller blade will likely have very little impact on the overall propeller performance.

Jet spacing (s_{jet}) for VGJ arrays can be defined as the ratio of jet diameter (d_{jet}) to distance between adjacent jets (x_{adj_jet}). For this study, s_{jet} was set to 2.5 in order to accommodate the entire array (four jets) without occupying a significant portion of the span, which ensures that the flow encountered by each jet is similar in Reynolds number.

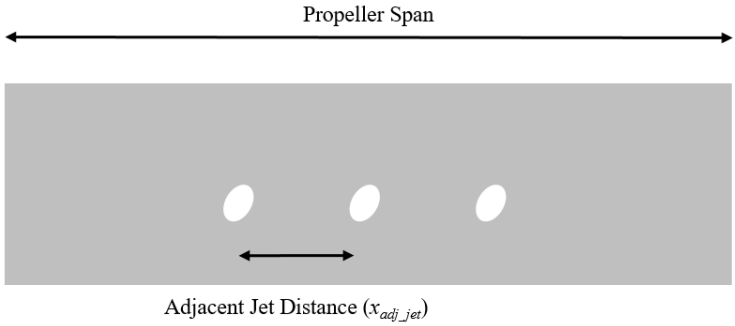

Figure 14. Detail of Adjacent Jet Distance Definition

The jet array angle (β) is defined as the angle between the jet array axis and the span axis. If this angle is non-zero, the chord location of each individual jet will be different, which may be useful to compensate for variations in flow separation location at different span locations. However, for this study, the jet array angle was set to zero for simplicity.

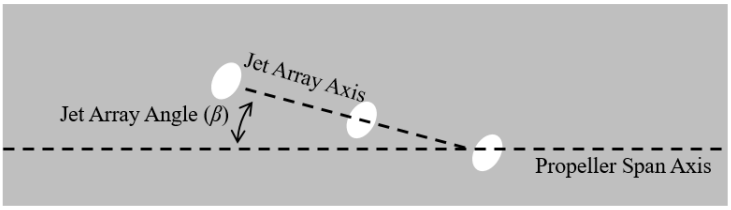

Figure 15. Detail of Jet Array Angle (β) Definition

For this study, the jet area and inlet area cross-sections were both defined as circles, in order to minimize the flow channel wall area to cross-sectional flow area ratio. Minimizing this ratio should also minimize boundary layer growth and therefore pressure loss through the flow channel, thus allowing more mass flow through the jet and consequently increased jet momentum ratio (*MR*). The jet momentum ratio is a function of jet velocity ratio (*VR*) and jet mass flow ($\dot{m}_{jet}$), which is a function of jet area ratio (*AR*). Jet area ratio is the proportion of the jet cross-section area (A_{jet}) to inlet cross-section area (A_{inlet}), and was set to 1 for this study.

3.4: Model Design and Manufacturing:

Two sets of test articles were designed for this study: 1:1 scale propellers for use on the wind tunnel dynamometer and 3:1 scale airfoil cross sections for use in the PIV water tunnel. The actual scale propellers were modeled in SolidWorks base on the geometry data provided by APC. This data included geometry for various airfoil shapes distributed span-wise, which were imported as curves in SolidWorks and the lofted together. To account for the twist of the blade, the angle of each curve sketch was rotated prior to the loft function. The result was a single propeller blades which was then mated to a semicircular base and revolve patterned around the

origin. The hub of each propeller half was modified with either an overhanging or an underhanging groove, to allow for the halves to be printed separately and mated together.

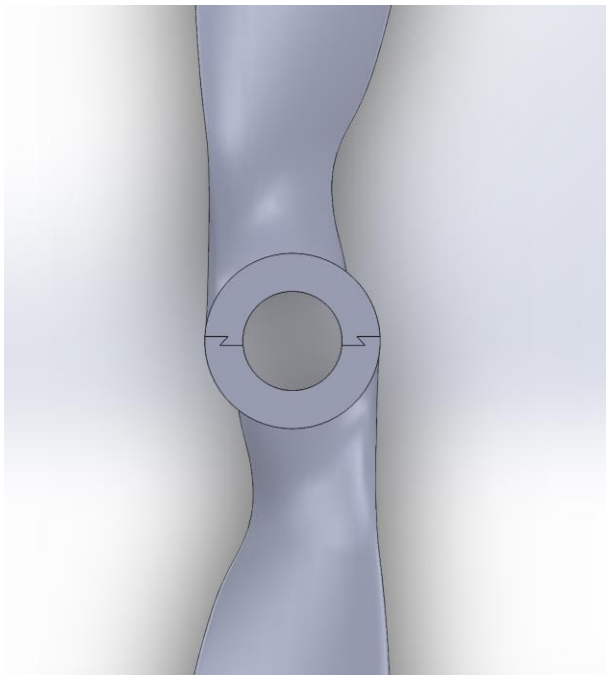

Figure 16. Detail of Propeller Connection Interface in CAD Model

To ensure manufacturing feasibility, the unmodified propeller was 3D printed using a Formlabs Form 2 printer and Tough Resin material for maximum part strength (55.7 MPa). To ensure the smoothest possible surface, this print job was executed at the printer's maximum resolution of 0.05mm. The flat surface of the propeller connection interface was affixed to the print bed, such that the propeller was printed from hub to tip. Immediately after printing, the propeller halves were immersed in an isopropyl alcohol bath for 15 minutes with occasional agitation, then immersed in second identical bath for 15 additional minutes. After the second bath, the parts were allowed to dry for 5 minutes then placed in an ultraviolet curing chamber for 1 hour to harden the material. The two propeller halves were then joined together using a press fit and liquid cyanoacrylate injected around the resulting edges. The adhesive was allowed to cure overnight before handling or testing the model. In order to validate the structural integrity of the test article,

it was place on a propeller dynamometer and spun up to 12,000 rpm for a sustained period of 5 minutes. Visual inspection of the test article showed no signs of cracking or deformation, and the manufacturing process was deemed viable. Because circular cross sections were selected for both the jets and inlets, the internal flow channels were also circular. This geometry minimized stress concentrations along the material edges, which is particularly important for stress in the radial direction.

To model the propeller test articles with self-aspirated VGJ's, several planes and axes were inserted into the baseline propeller SolidWorks model, in order to define the geometry of the self-aspirated VGJ's. The jet cross section was linear patterned span-wise along the jet plane, and then cut at angle using reference geometry from the pitch plane to create the flow channels and inlets.

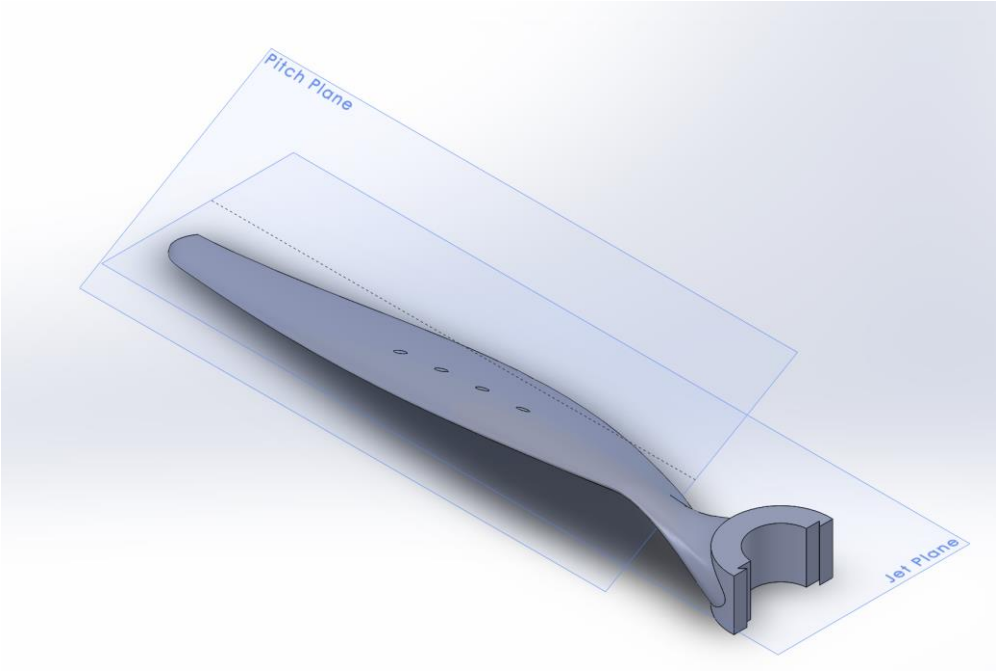

Figure 17. Detail of VGJ Definition in Propeller CAD Model

A nearly identical manufacturing process was used to fabricate the 3:1 cross section models for water tunnel PIV testing. The only difference in manufacturing was the use of matte black printing material in place of tough resin. This material was used to reduce any visual interference with the laser and PIV setup that may have occurred with the semi-translucent rough resin. Further, because the water tunnel model would not be subject to rotation, the higher strength of the tough resin was not as critical. A square interlock system was integrated into the water tunnel models which allowed three sections to be mated together and mounted in the water tunnel. The two outer sections were solid airfoil designs, while the middle section was swapped between three different self-aspirated VGJ configurations and a baseline configuration (the baseline configurations had a VGJ array, however the inlets were covered using packing tape to prevent flow). The water tunnel models were scaled up in airfoil size, jet/inlet area, and jet spacing by a factor of three to achieve the desired Reynolds number range given the water tunnel's maximum speed capability.

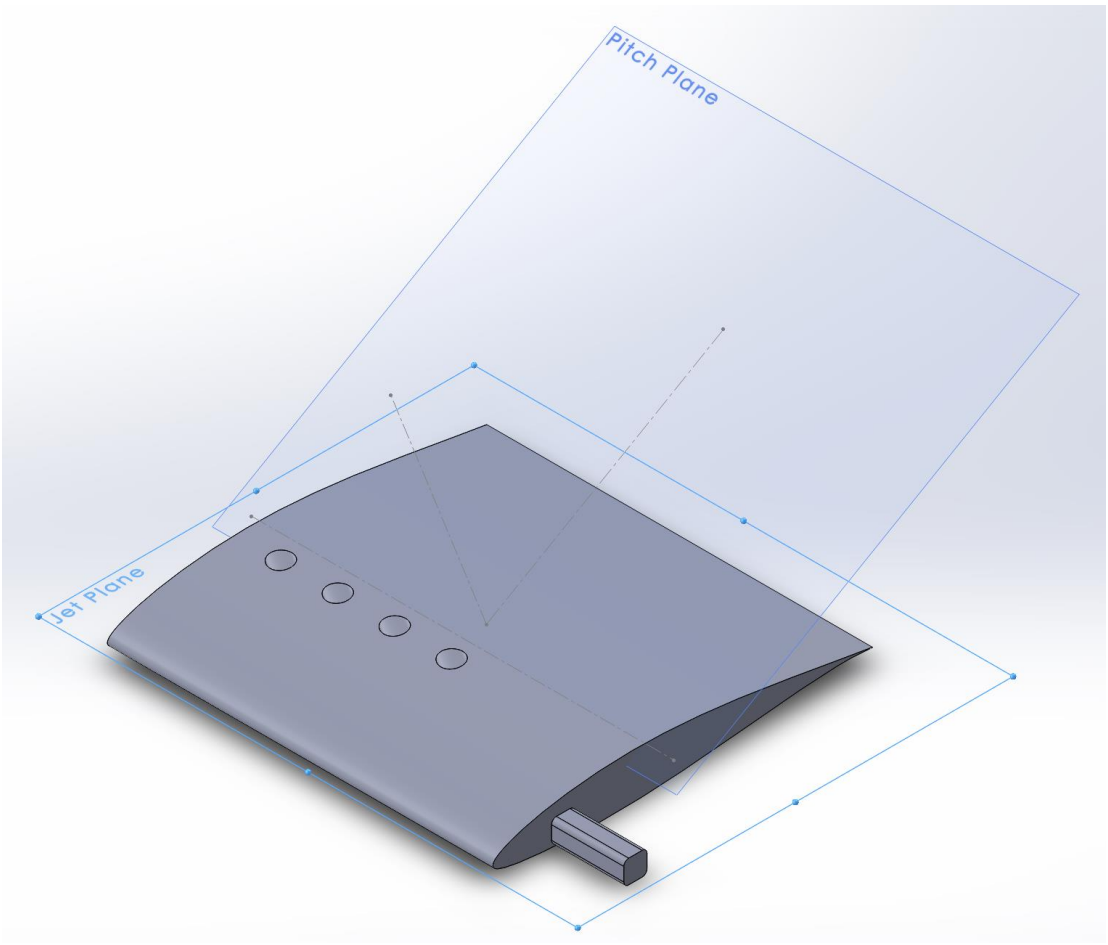

Figure 18. Detail of VGJ Definition in Scaled airfoil CAD Model

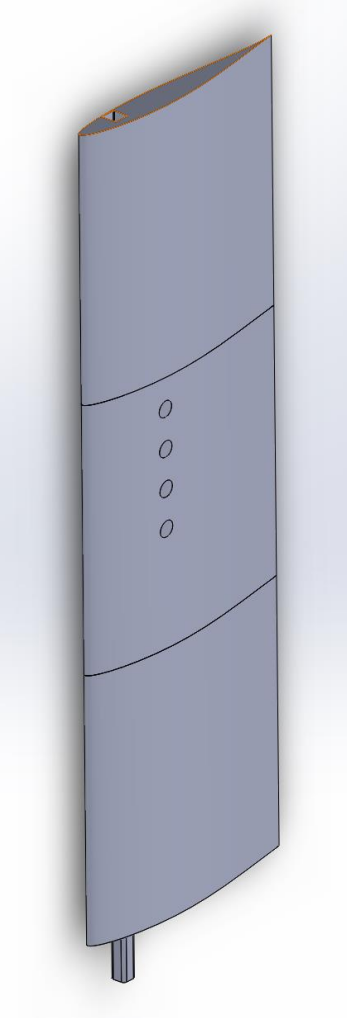

Figure 19. Scaled Airfoil Assembly CAD Model

3.5 Experimental Setup

3.5.1 Water Tunnel Facility

In order to characterize the effect of self-aspirated VGJ presence on an airfoil shape, a PIV study was conducted on the scaled airfoil models in the Oklahoma State University low speed water tunnel facility. This facility is a closed loop, dual pump water tunnel with test section dimensions of 30 cm x 30 cm x 100 cm. The system was designed by Engineering Laboratory Design, Inc.

and has two 7.5 HP electric motors, each connected to a Gusher pump (model PGL 4X6-105EH-C-B) and controlled by a variable frequency drive (VFD). According to the calibration sheet for the water tunnel, the maximum theoretical speed of the tunnel is 1.2 m/s (3.94 ft/s) at an operating frequency of 70.0 Hz for both VFD's. This is based on experimental testing conducted by Engineering Laboratory Designs, which revealed that a change of 0.1 Hz on both VFD's resulted in a test section velocity change of 0.0166 m/s (0.0545 ft/s). This calculation assumes linear relationships between both the VFD frequency and motor/pump RPM and the pump RPM and tunnel velocity. The water tunnel was filled with tap water filtered through a Whirlpool WHKF-DWHZV filter, which removed all particles larger than 5 μm ($1.969x10^{-4}$ inches). The water was then seeded with 18 μm ($7.087x10^{-4}$ inches) hollow glass spheres to scatter light from the laser.

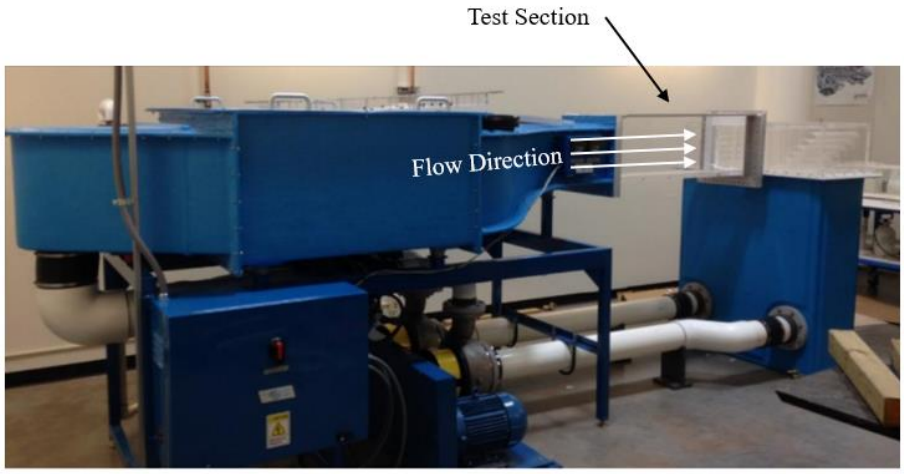

Figure 20. Oklahoma State University Low Speed Water Tunnel

3.5.2 Laser System

In order to precisely illuminate suspended particles in the camera focus plane, dual Nd-YAG lasers manufactured by New Wave Research were triggered at various frequencies to release 200 mJ pulses. These laser pulses were guided through a series of optics to achieve the correct

location and minimal laser sheet thickness. In particular, a focusing lens, two prisms, and a thin cylindrical lens were arranged on an optical bench located beneath the tunnel.

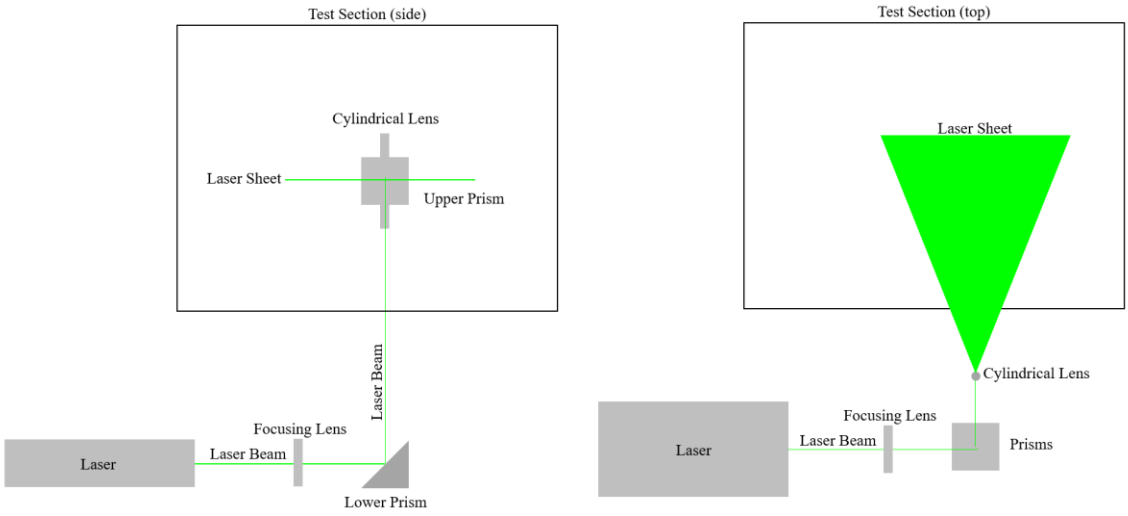

Figure 21. PIV Laser Optics Setup Side View (left) and Top View (right)

3.5.3 Recording System

In conjunction with the laser system, a high speed camera system was utilized to collect images of suspended particles in the flow stream. This camera was manufactured by LaVision and equipped with a 2560x2160 pixel sCMOS sensor having a maximum capture rate of 50 Hz. A 60 mm focal length Nikon Nikkor lens was affixed to the camera, allowing for manual zoom, focus, and aperture adjustment. This camera was mounted to the same optical bench as the laser, and placed directly under the test article, such that the camera was facing directly upward. The camera was then focused and calibrated using a dual plane stereo PIV calibration target provided by LaVision. This calibration sheet was affixed to a metal sheet and mounted to a small stand, which was placed in the test section, adjacent to the test article and at the proper height (aligned with one of the center jets). This same setup was also used to set the vertical location of the laser sheet, to ensure good camera focus and particle illumination. Camera images were acquired using the Motion Studio application and were processed using the DaVis image processing software.

The built-in camera calibration macro in DaVis was used for calibration and resulted in a standard deviation of fit of 1.1438 px.

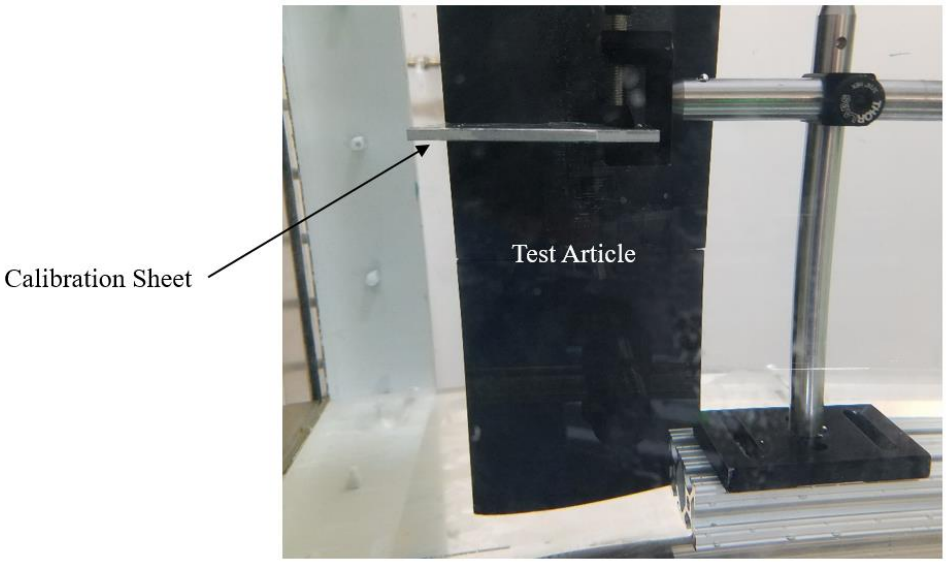

Figure 22. Camera Calibration Sheet in Test Section Adjacent to Test Article (Side View)

3.6 Test Procedures

During water tunnel PIV tests, the ambient lab temperature was measured to be between 66.5° and 71.1° Fahrenheit. These conditions correspond to a kinematic viscosity of 0.890 cP and density of 62.3 lbm/ft^3 for water. Water tunnel tests were conducted at various tunnel speeds and angles of attack for each of the three VGJ configurations and the baseline model. The speeds were selected to produce certain chord-based Reynolds numbers that may occur for the propeller during different mission phases. Based on these desired Reynolds number values, the tunnel speeds and VFD frequencies to achieve those speeds were calculated. Due to limited control resolution, the actual frequencies were rounded to the nearest 0.1 Hz. Additionally, the pulse separation time (Δt) for the camera and lasers must be modified in order to achieve approximately 10 px of mean particle displacement between image pairs, a condition required for optimal accuracy in the image processing algorithms. Experimental data showed good results for Δt=500

μs at maximum VFD frequency of 70.0 Hz. This information was used to calculate the optimal pulse separation time at other speeds for the same test setup, assuming a linear correlation between pulse separation time and tunnel speed.

Table 1 – VFD Frequencies to Achieve Selected Reynolds Numbers and Associated Camera Timing Differential

Reynolds Number	Tunnel Velocity (m/s -fps)	VFD Frequency (Hz)	Δt (s)
15,000	0.175 / 0.574	10.6	3,710
30,000	0.350 / 1.148	21.1	1,855
45,000	0.526 / 1.726	31.7	1,237
60,000	0.701 / 2.300	42.2	928
75,000	0.876 / 2.874	52.8	742
90,000	1.051 / 3.448	63.3	618

For each of these resulting tunnel speeds, three different angles of attack were evaluated in order to produce three different scenarios for the airfoil shape: completely attached flow (0° AoA), nearly separated flow (15° AoA), and completely detached flow (30° AoA).

In order to make reasonable comparisons between the scaled airfoil test conditions and actual propeller operating conditions, both Reynolds number and advance ratio must be matched. Reynolds number is directly proportional to velocity, which was a controlled variable in this study. Advance ratio, however, must be correlated to the angle of attack variable used in the experiments. To accomplish this, various combinations of rotational velocities and freestream velocities were selected. These combinations represent operating conditions that a small UAS

may experience during flight. Based on the two velocities, both advance ratio and relative angle of attack were calculated. For each freestream velocity, the relationship between angle of attack and advance ratio is logarithmic.

Table 2 – Simulated Propeller Operating Conditions and Associated Angle of Attack and Advance Ratio

V_inf (mph):	ω (rpm):	J:	α_rel (deg):
10	2000	0.528	64.7
10	4000	0.264	46.6
10	6000	0.176	35.1
10	8000	0.132	27.8
10	10000	0.1056	22.9
20	2000	1.056	76.7
20	4000	0.528	64.7
20	6000	0.352	54.6
20	8000	0.264	46.6
20	10000	0.2112	40.2
30	2000	1.584	81.0
30	4000	0.792	72.5
30	6000	0.528	64.7
30	8000	0.396	57.7
30	10000	0.3168	51.7
40	2000	2.112	83.2
40	4000	1.056	76.7
40	6000	0.704	70.4
40	8000	0.528	64.7
40	10000	0.4224	59.4

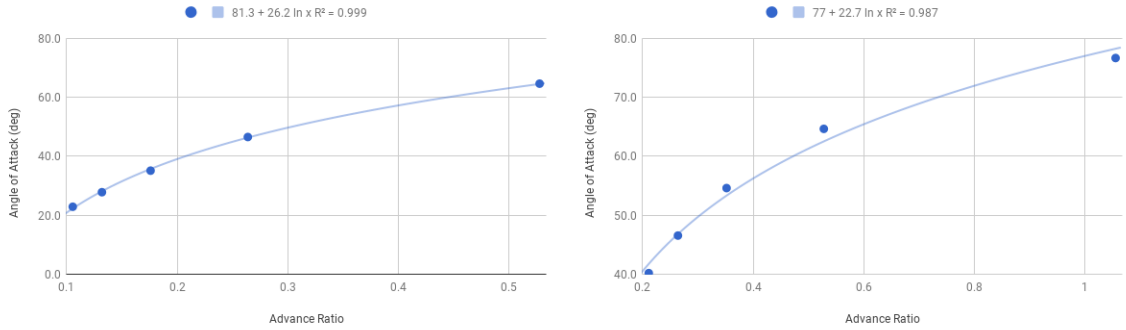

Figure 23. Angle of Attack vs Advance Ratio Curves for Freestream Velocities of 10 mph (left) and 20 mph (right)

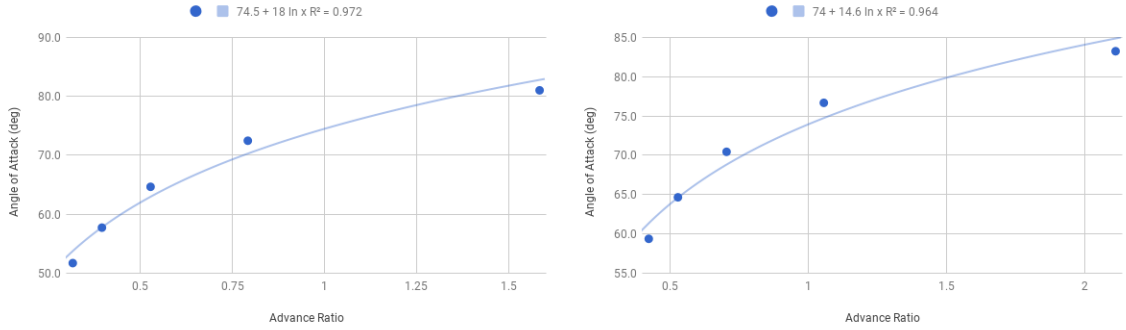

Figure 24. Angle of Attack vs Advance Ratio Curves for Freestream Velocities of 30 mph (left) and 40 mph (right)

The angles of attack presented above are total angle of attack values, meaning that they do not account for the pitch angle of the blade at various radial locations. To determine the relative angle of attack, the pitch angle at the location of interest must be subtracted from the total angle of attack values presented above, which typically results in relative angles of attack between 0° and 30°.

To conduct each of the 64 tests, the following procedure was used:

1. Mount model with configuration to test in the water tunnel test section, setting the desired angle of attack using protractor.
2. Turn on laser power supplies.
3. Set lasers to external timing and power level 6.
4. Activate lasers.
5. Set appropriate Δt on timing unit.
6. Power up camera and connect using Motion Studio software.
7. Set VFD's to desired frequency and wait until pumps have spun up.
8. Turn off laboratory lights.
9. Activate timing units (lasers are now pulsing).
10. Record 200 images (100 image pairs) using Motion Studio software.
11. Deactivate timing unit (laser are now off).
12. Adjust VFD Frequency and/or angle of attack and repeat.

Upon conclusion of laboratory testing, the resulting data was processed using the DaVis processing software. As each data set was imported into the program, the correct Δt was assigned. The following operations were performed on the data to produce PIV results:

1. Create multi-frame buffers from time series
2. PIV image preprocessing – Subtract sliding background (3 px scale), subtract offset counts (5 counts)
3. Mask definition – manually defined and inspected for each dataset
4. Vector calculation
5. Vector postprocessing
6. Vector statistics (vector field result) – Average and standard deviation

This processing produced a vector field for each dataset, containing velocity vectors and vector field statistics which are useful for making observations about the test articles.

4 FINDINGS

4.1 Baseline Airfoil – 15,000 Reynolds Number, 15° Angle of Attack

The baseline airfoil (without any SAVGJ's) encounters flow separation at an angle of attack of 15° in 15,000 Reynolds number flow conditions as shown in Figure 22. This separation occurs at approximately 15% chord and does not reattach to the airfoil surface. Small UAS propellers experience similar operating conditions during certain mission segments, although the separation location may vary due to the rotational velocity component.

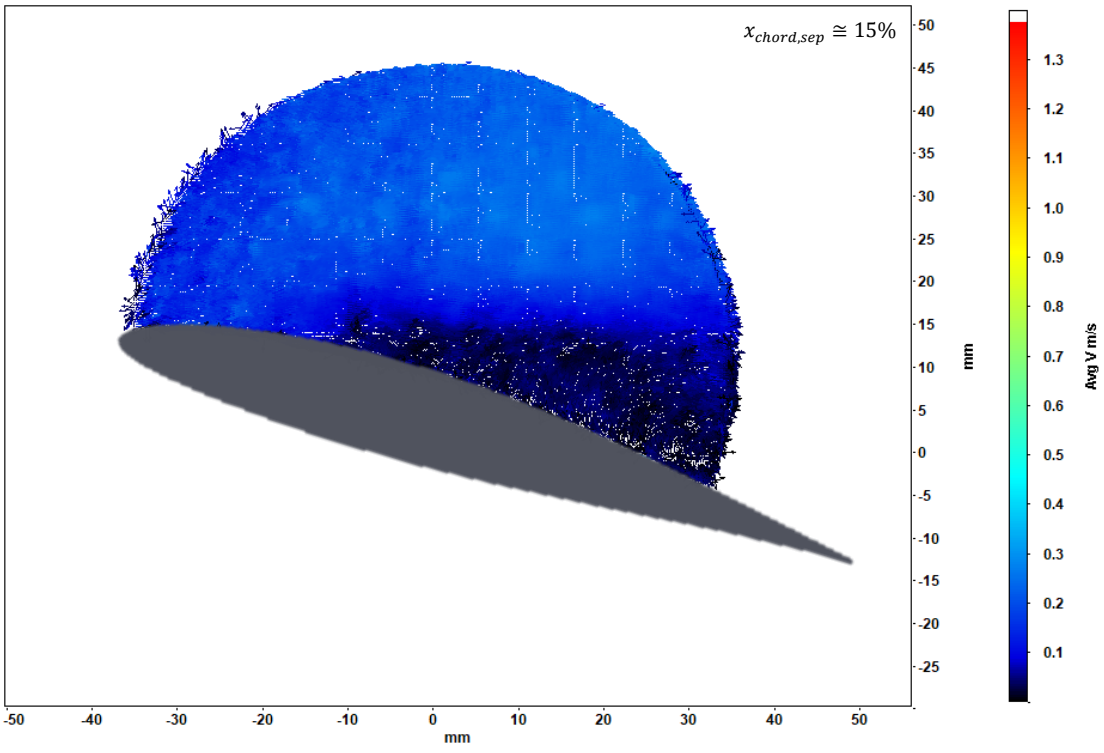

Figure 25. Separation Location of Scaled Airfoil at 15° AoA and 15,000 Re

4.2 Baseline Airfoil – Reynolds Number Effect at 15° Angle of Attack

In order to characterize additional operating conditions small UAS propellers may experience, a study of the effect of Reynolds number on separation chord location ($x_{chord,\ sep}$) was conducted. Results show the separation location ranging from approximately 15% chord to 60% chord for Reynolds number ranging from 15k to 75k. No flow separation was observed for the Re = 90k case.

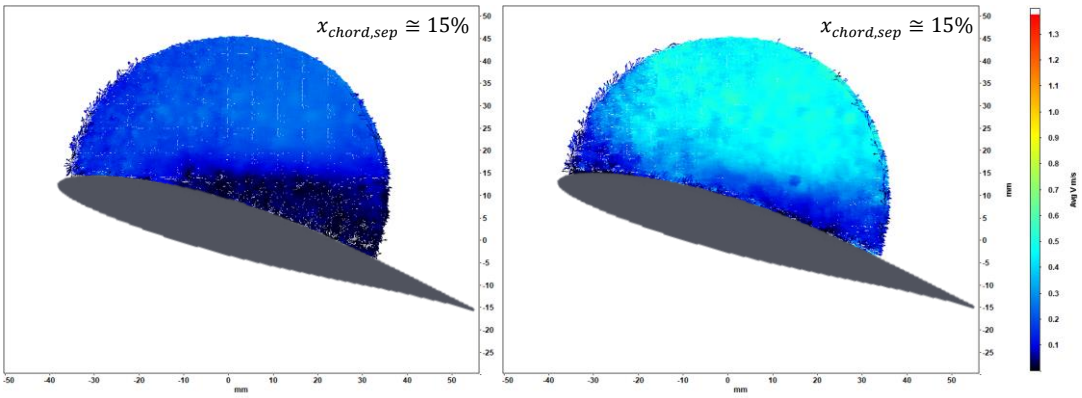

Figure 26. The Effect of Reynolds Number on Separation Location of Scaled Airfoils at 15° AoA, 15,000 Re (left) and 30,000 Re (right)

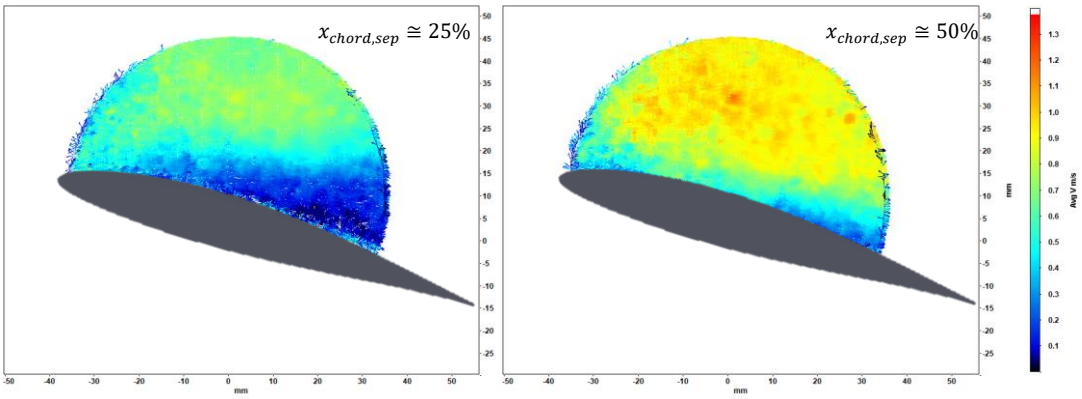

Figure 27. The Effect of Reynolds Number on Separation Location of Scaled Airfoils at 15° AoA, 45,000 Re (left) and 60,000 Re (right)

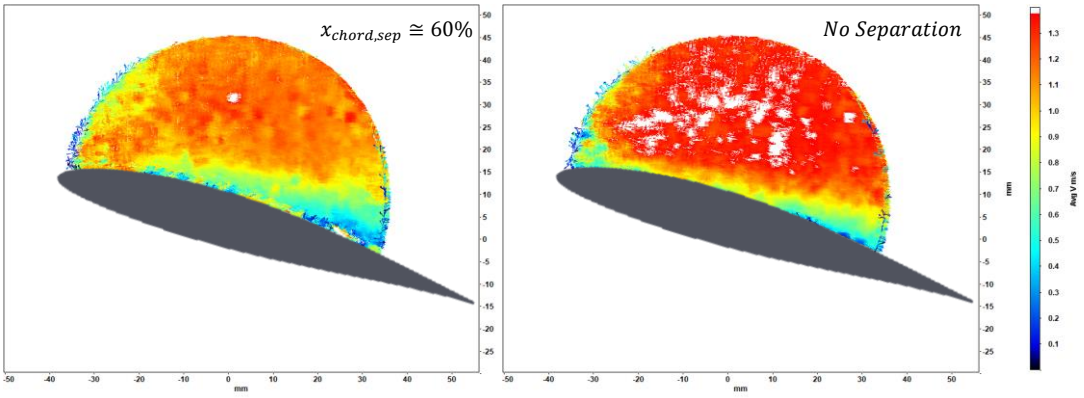

Figure 28. The Effect of Reynolds Number on Separation Location of Scaled Airfoils at 15° AoA, 75,000 Re (left) and 90,000 Re (right)

4.3 Baseline Airfoil – Angle of Attack Effect at 15,000 Reynolds Number

In addition to Reynolds number, the separation chord location of the scaled airfoil cross section was also a function of angle of attack. Sensitivity to this effect was greatest at 15,000 Reynolds number, as expected due to lower freestream flow momentum. The 0° AoA condition did not exhibit any flow separation, while the most extreme case of 30° AoA separated flow at the leading edge (0% chord). The baseline case (15° AoA) exhibited flow separation at approximately 15% chord.

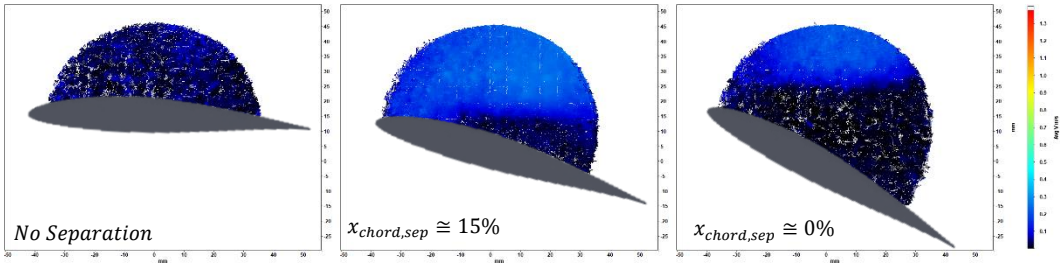

Figure 29. The Effect of Angle of Attack on Separation Location of Scaled Airfoils at 15,000 Re, 0° AoA (left), 15° AoA (center), and 30° AoA (right)

4.4 Reynolds Number Effect on SAVGJ Array at 50% Chord

Results of the baseline airfoil study revealed significant flow separation at nearly every tested Reynolds number for an angle of attack of 15°. Test configuration 2 (SAVGJ array at 50% chord) was tested across the same conditions where flow separation is known to occur. Results showed what appears to be a vortex rooted at or near the SAVGJ array occurring most Reynolds numbers. One key characteristic that indicates a vortex is the two thin flow regions with nearly zero streamwise velocity, one near the airfoil suction surface and the other adjacent to the freestream (noted in Figure 27). These two thin regions are likely the vortex wall and show no streamwise velocity because the flow is moving either into or out of the camera image plane recorded in the 2D PIV images. Centered between these two regions is a third region with significant streamwise velocity, which is most likely the vortex core.

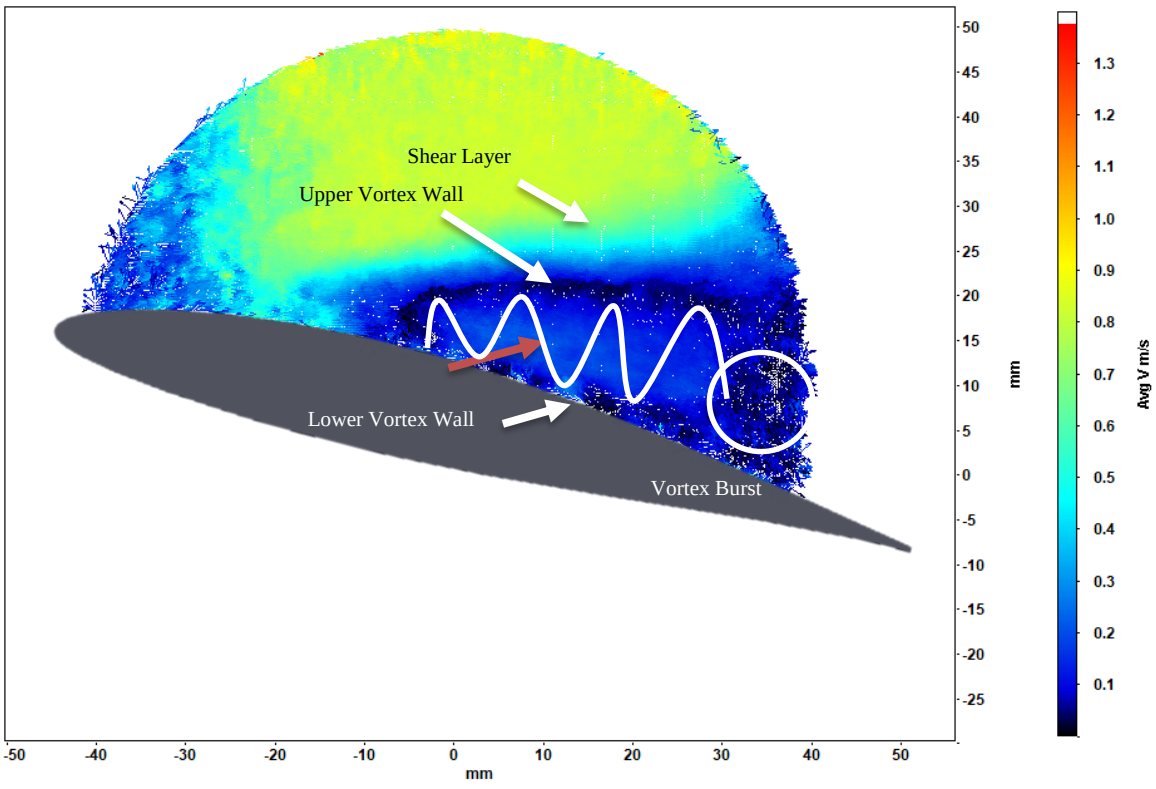

Figure 30. Detail of Vortex Elements on Scaled Airfoil with SAVGJ Array at 50% Chord at 15° AoA and 60,000 Re

Vortex elements can be seen in PIV images at most of the tested Reynolds number conditions. The vortex appears to be most developed in the 45,000 Re and 60,000 Re images. At 90,000 Re, the lower vortex wall is not apparent, however the upper vortex wall and core appear to remain developed. No evidence of vortex formation is present in the 30,000 Re image, which is strange because similar vortices appear in the 15,000 Re and 45,000 Re images.

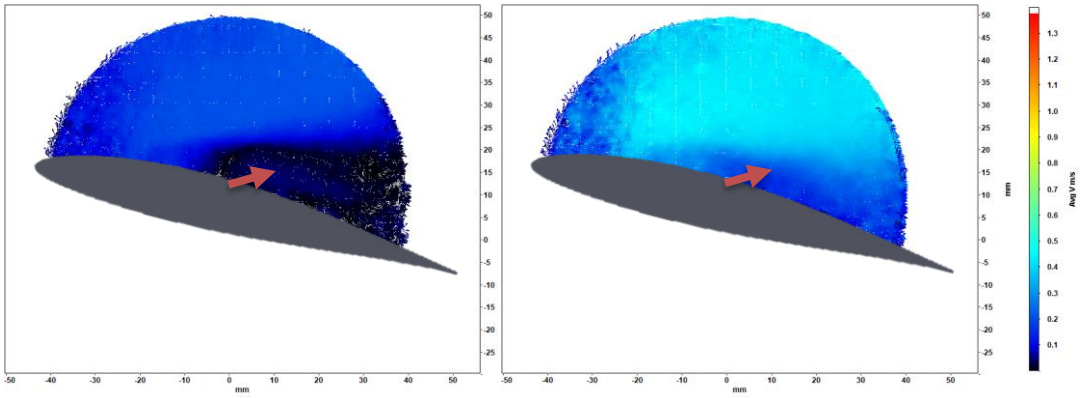

Figure 31. The Effect of Reynolds Number on Separation Location of Scaled Airfoil with SAVGJ Array at 50% Chord at 15° AoA, 15,000 Re (left) and 30,000 Re (right)

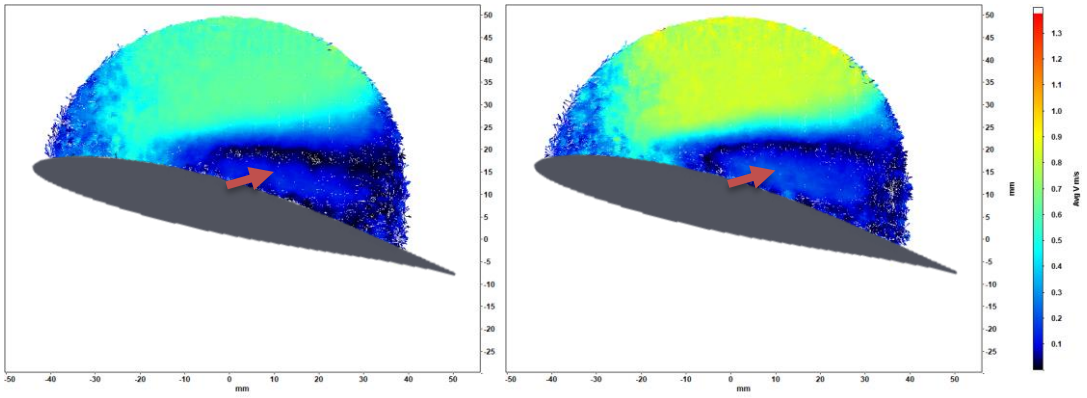

Figure 32. The Effect of Reynolds Number on Separation Location of Scaled Airfoil with SAVGJ Array at 50% Chord at 15° AoA, 45,000 Re (left) and 60,000 Re (right)

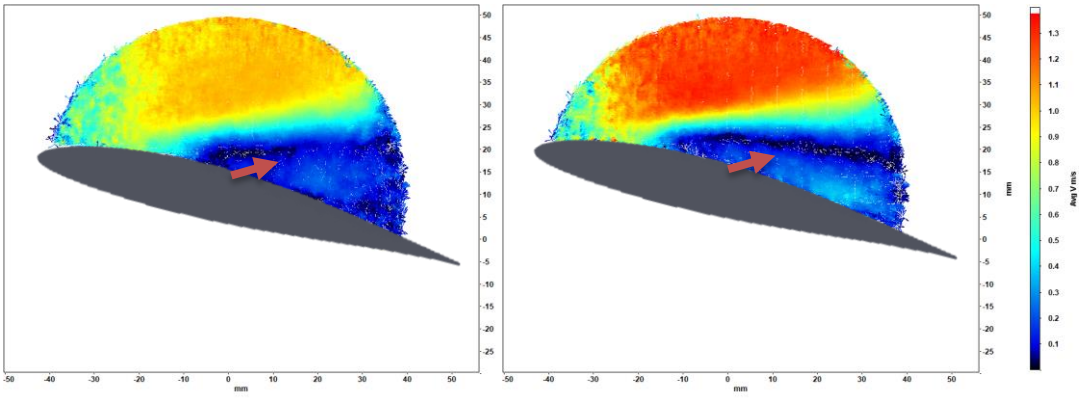

Figure 33. The Effect of Reynolds Number on Separation Location of Scaled Airfoil with SAVGJ Array at 50% Chord at 15° AoA, 75,000 Re (left) and 90,000 Re (right)

4.5 Angle of Attack Effect on SAVGJ Array at 50% Chord

In order characterize the propeller operating conditions where the SAVGJ array is active and effective, three different angles of attack were tested. The effect of angle of attack on SAVGJ activation is most clear at 45,000 Re. At 0° the flow remains attached, no vortex is generated, and boundary layer growth is absent. At 15° a vortex appears, rooted just upstream of the SAVGJ Array at 45% chord ($x_{chord,\,vtx}$ = 45%). Total separation occurs at 30° with no vortex elements.

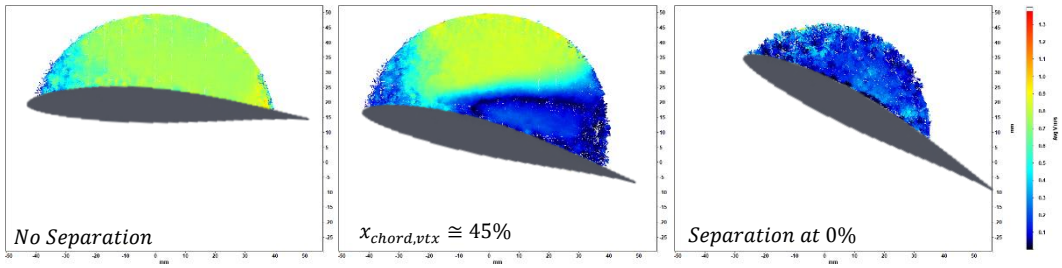

Figure 34. The Effect of Angle of Attack on Separation Location of Scaled Airfoil with SAVGJ Array at 50% Chord at 45,000 Re, 0° AoA (left), 15° AoA (center), and 30° AoA (right)

4.6 Effect of SAVGJ Array Chord Location

In addition to the SAVGJ array at 50% chord, two other locations were tested: 40% and 60%. For the 15,000 Re flow condition at 15° angle of attack, results show weak vortices at 40% and 60% chord, while a stronger vortex occurs at 50% chord. For the 90,000 Re flow condition at 15° angle of attack, results show strong vortices at 40% and 50% chord, while a weaker vortex occurs at 60% chord.

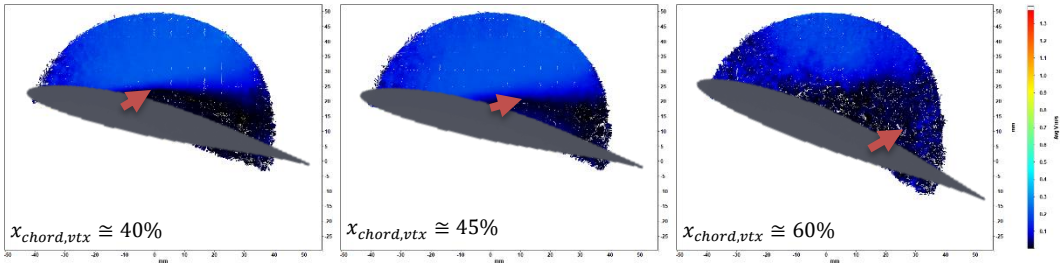

Figure 35. The Effect of Chord Location on Vortex Formation at 15,000 Re for a Scaled Airfoil with SAVGJ Array at 40% Chord (left), 50% Chord (center), and 60% Chord (right)

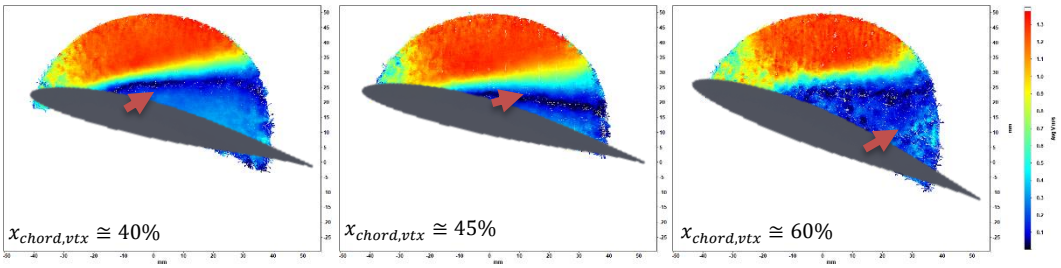

Figure 36. The Effect of Chord Location on Vortex Formation at 90,000 Re for a Scaled Airfoil with SAVGJ Array at 40% Chord (left), 50% Chord (center), and 60% Chord (right)

Coherent structures can clearly be seen above the suction surface of the airfoil. To qualitatively compare the effect of these structures on the flow, 2D streamlines can be drawn over the vortex core to show the direction of the flow. This flow direction can then be compared to the directions of the shear layer on the baseline case to show how much the flow has turned. As flow is turned to remain nearly parallel to the airfoil surface, it is accelerated more and in turn generates more

lift. At low Reynolds numbers, the SAVGJ arrays are more effective at changing flow direction. This visualization technique also revealed that a SAVGJ array at 60% chord was less advantageous, as the flow did not turn as significantly as the 40% or 50% chord locations.

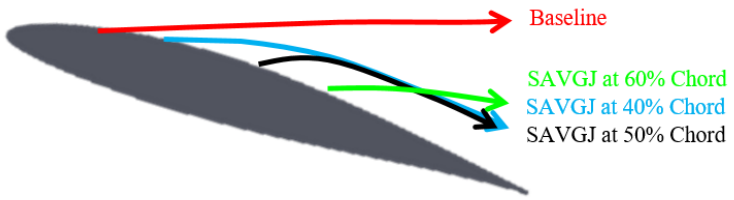

Figure 37. Flow Directions of SAVGJ Configurations and Baseline at 15,000 Reynolds Number and 15° Angle of Attack

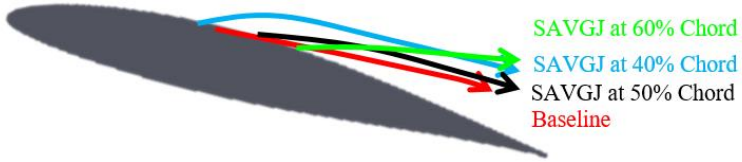

Figure 38. Flow Directions of SAVGJ Configurations and Baseline at 90,000 Reynolds Number and 15° Angle of Attack

A direct comparison between the baseline airfoil and each SAVGJ array configuration reveals significant changes in the behavior of the fluid in the separation bubble. All baseline configurations show turbulent flow in the separation bubble, likely produced by massive amounts of tiny eddies in the flow. However, in nearly all configurations of SAVGJ arrays produced coherent structures in at least two operating conditions. PIV images of these coherent structures show evidence of vortex generation, which is very distinctly different from the baseline configurations.

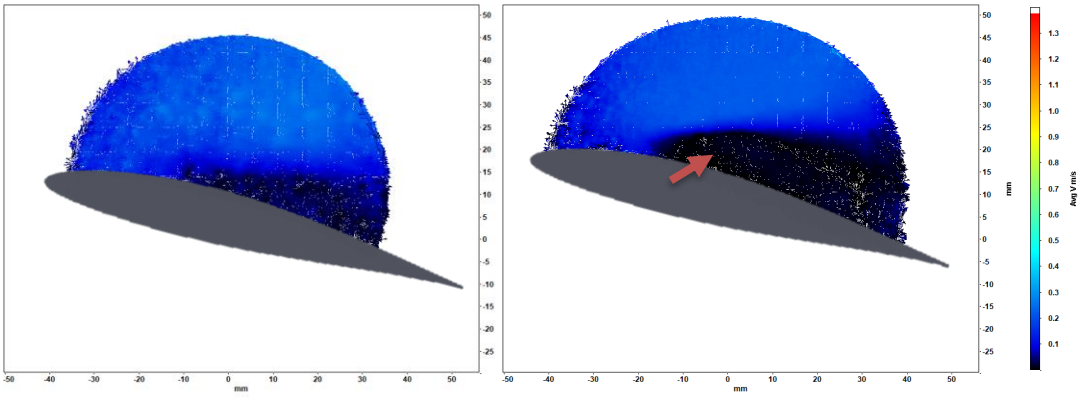

Figure 39. Scaled Airfoil Without SAVGJ Array (left) and with SAVGJ Array at 40% Chord (right) at 15° Angle of Attack and 15,000 Reynolds Number

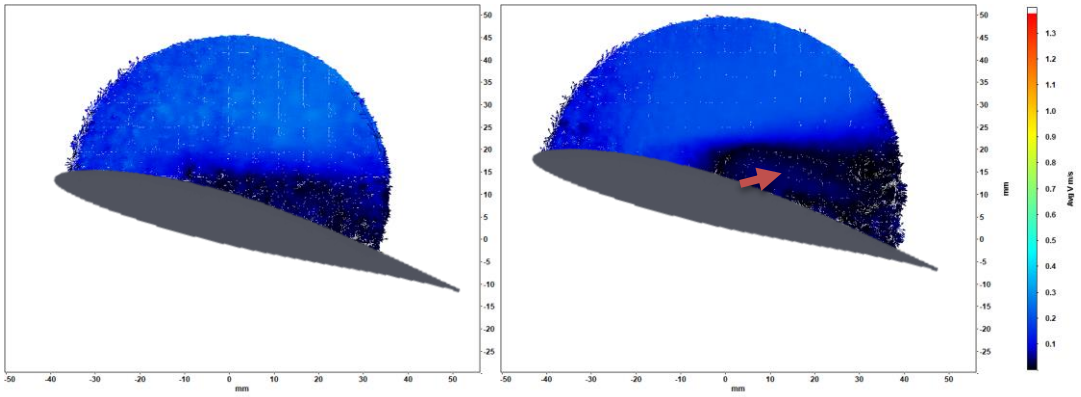

Figure 40. Scaled Airfoil Without SAVGJ Array (left) and with SAVGJ Array at 50% Chord (right) at 15° Angle of Attack and 15,000 Reynolds Number

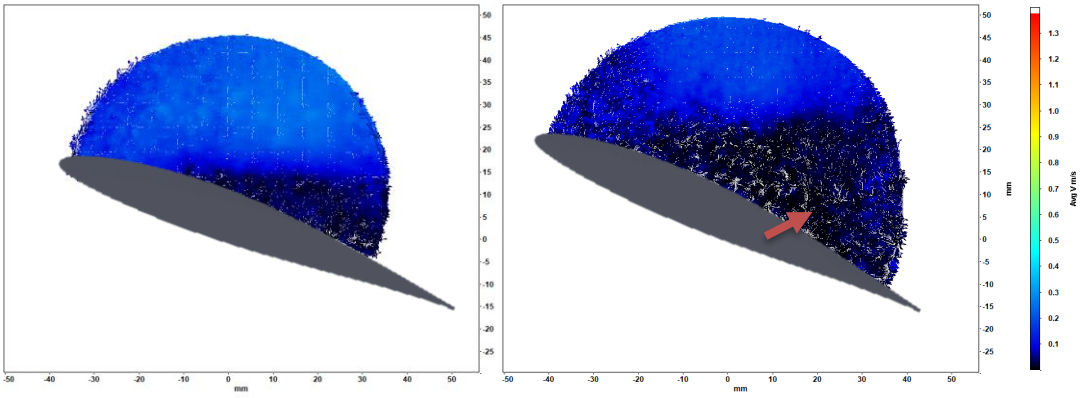

Figure 41. Scaled Airfoil Without SAVGJ Array (left) and with SAVGJ Array at 60% Chord (right) at 15° Angle of Attack and 15,000 Reynolds Number

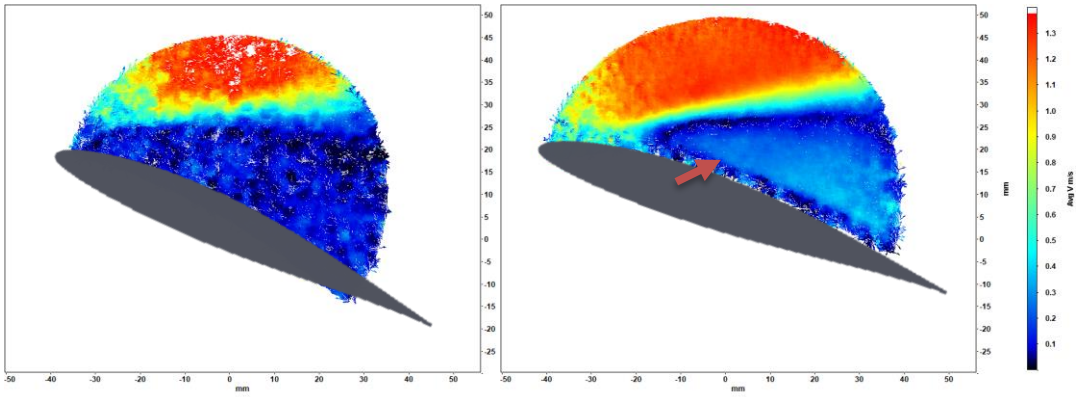

Figure 42. Scaled Airfoil Without SAVGJ Array (left) and with SAVGJ Array at 40% Chord (right) at 15° Angle of Attack and 90,000 Reynolds Number

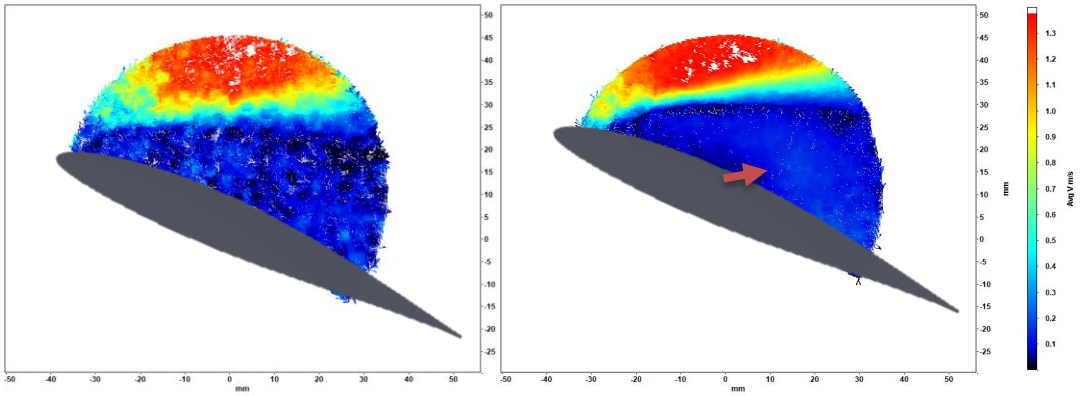

Figure 43. Scaled Airfoil Without SAVGJ Array (left) and with SAVGJ Array at 50% Chord (right) at 15° Angle of Attack and 90,000 Reynolds Number

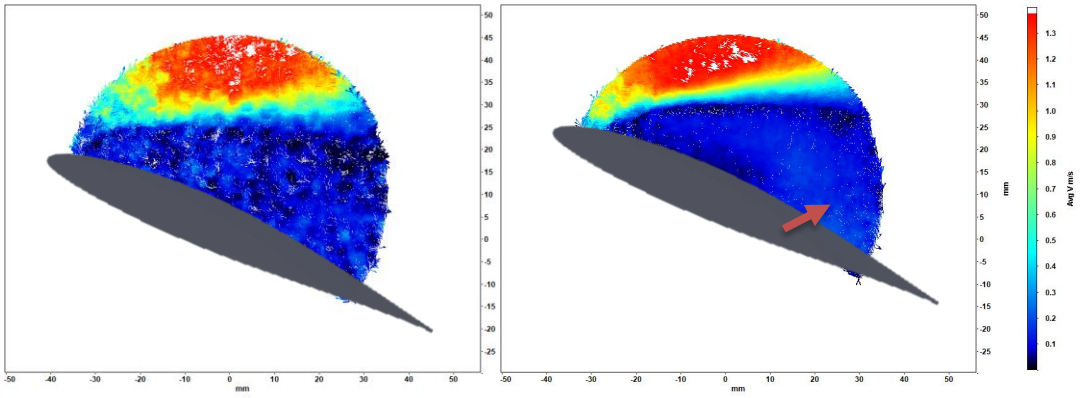

Figure 44. Scaled Airfoil Without SAVGJ Array (left) and with SAVGJ Array at 60% Chord (right) at 15° Angle of Attack and 90,000 Reynolds Number

While vortex formation was optimal at 15° angle of attack, the SAVGJ arrays also had a significant effect on the flow at 0°. Significant boundary layer acceleration was observed at several Reynolds numbers for every array chord location. This effect will likely result in increased lift and/or decreased drag compared to the baseline airfoil.

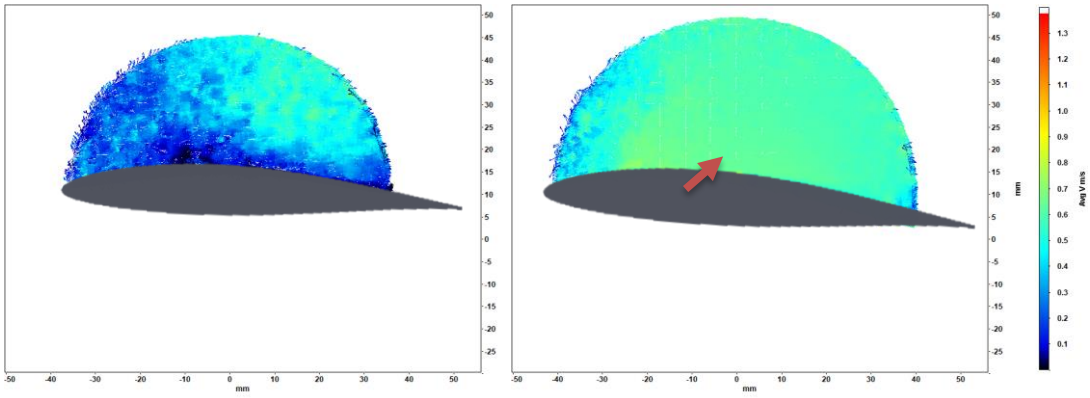

Figure 45. Scaled Airfoil Without SAVGJ Array (left) and with SAVGJ Array at 40% Chord (right) at 0° Angle of Attack and 45,000 Reynolds Number

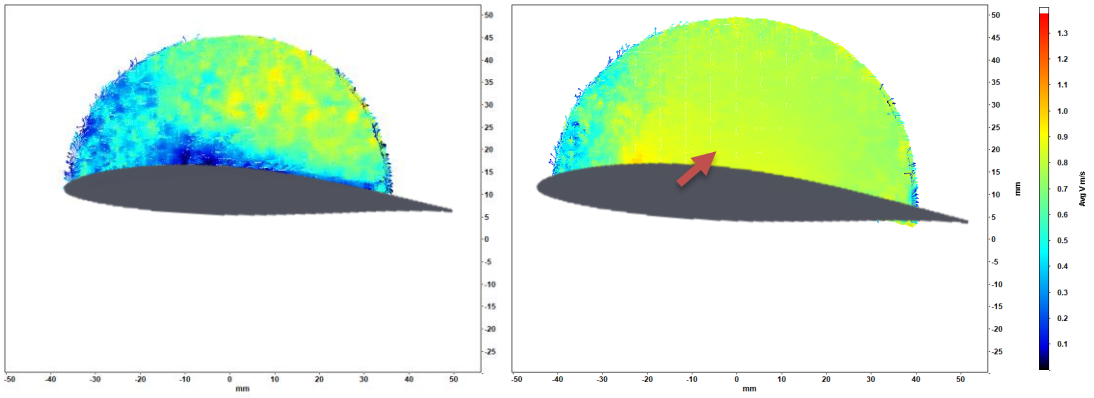

Figure 46. Scaled Airfoil Without SAVGJ Array (left) and with SAVGJ Array at 40% Chord (right) at 0° Angle of Attack and 60,000 Reynolds Number

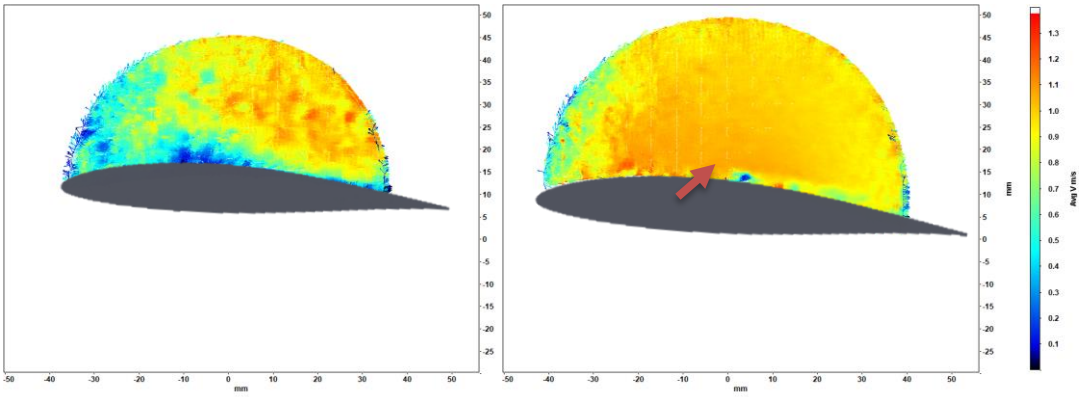

Figure 47. Scaled Airfoil Without SAVGJ Array (left) and with SAVGJ Array at 40% Chord (right) at 0° Angle of Attack and 75,000 Reynolds Number

To allow for comparison to other flow control techniques, the coefficient of momentum (C_μ) was calculated for the jets at several operating conditions. Coefficient of momentum is the ratio of jet momentum to freestream momentum and as defined below. In this equation, suction surface area (S) is used to calculate the freestream momentum (McQuilling and Jacob, 2004). Jet mass flowrate was derived using Bernoulli's equation, and using pressures calculated from the XFOIL software package. Jet velocity was calculated from the mass flow rate using the continuity equation.

$$C_\mu = \frac{2\dot{m}_{jet}V_{jet}}{\rho S V_\infty}$$

$$\dot{m}_{jet} = A_{jet}\sqrt{\frac{2(P_{pres} - P_{suc})}{\rho}}$$

$$V_{jet} = \frac{\dot{m}_{jet}}{A_{jet}}$$

Coefficient of momentum was calculated at four operating conditions. Pressure distributions were found to have little sensitivity to changing Reynolds number over the evaluated range, however they were found to be very sensitive to changes in angle of attack. Variation in pressure distributions led to significant changes in coefficient of momentum. As expected, jet chord location also had a significant effect on pressure and coefficient of momentum. The 30° cases were not included in this analysis, as they are outside the domain of XFOIL's analysis capabilities, making accurate pressure distributions impossible to obtain without further experimentation.

Table 3 – Coefficient of Momentum at Varying Chord Locations, Reynolds Numbers, and Angles of Attack

Jet Location:	Re=15k, 0deg:	Re=15k, 15deg:	Re=90k, 0deg:	Re=90k, 15deg:
0.40:	0.00947	0.00170	0.04626	0.00833
0.50:	0.00716	0.00129	0.03712	0.00668
0.60:	0.00501	0.00090	0.03255	0.00586

4.7 Uncertainty Analysis

The manufacturer of the PIV software used in this study (LaVision) estimates the uncertainty of their measurements to be approximately ±0.1 pixels, which is approximately ±1% of

the measured values, based on a 10 pixel average particle displacement. This error is caused by false correlation peak detection when analyzing image pairs for particle displacement. Many factors can effect this phenomenon, such as: out of plane motion, image noise, and low seeding density. Sciacchitano et al. (2013) developed a mathematical model for calculating the uncertainty of each individual vector in a PIV data set. A Matlab code was developed from this model, which accepts raw PIV images and displacement fields and outputs the uncertainty field. This uncertainty field was then converted into percentages of measured values and averaged. PIV data from the 15,000 Reynolds number, 15° angle of attack baseline configuration was input into the algorithm. The result, ironically, was ±1.018%, which is very similar to the estimated uncertainty provided by LaVision and thus corroborates the precision of the experimental setup.

5 CONCLUSIONS

5.1 Baseline Airfoil vs. SAVGJ Array

For 15,000 Re flow at 15° angle of attack, the 40% chord and 60% chord SAVGJ configurations appear to increase the thickness of the separation bubble which occurred on the baseline propeller. This is most likely due to low jet momentum, caused by low freestream momentum (as evidenced by the low Reynolds number). Low jet momentum is less likely to penetrate the freestream flow and promote the mixing required to generate a vortex. The 50% chord configuration shows evidence of a weak vortex. This vortex weak because the momentum difference between the freestream flow and quiescent boundary layer is very small. Testing at 90,000 Re revealed vortex formation at nearly for the SAVGJ array at 40% chord, while no vortices were generated by the array at 50% chord or 60% chord. This is most likely because the jet array was located significantly downstream of the separation location and thus unable to create a stable vortex to promote the mixing of the quiescent boundary layer and freestream flow.

In addition to vortex generation, the SAVGJ arrays also accelerate boundary layer flow over a certain Reynolds range. For Reynolds numbers ranging from 45,000 to 75,000, at 0° angle of attack the SAVGJ arrays at all three chord locations accelerate the boundary layer flow significantly, resulting in less drag. At lower Reynolds numbers the boundary layer was blown off by the jets, while at higher Reynolds numbers the flow field remained unchanged. This finding shows that SAVGJ arrays can be beneficial over a wide range of operating conditions, not just at one particular condition, making them perfectly suited for propeller performance augmentation. Results of the water PIV experiment on the 3:1 scaled airfoil cross section models revealed

several SAVGJ array configurations which successfully generate vortices. If similar operating conditions were achieved on a propeller, a noticeable performance gain may occur.

The ideal chord location of the SAVGJ array is at or slightly ahead of the flow separation location of the blade. This location changes dynamically based on the operating conditions of the blade (relative angle of attack, Reynolds number). If the SAVGJ array is located downstream of the separation chord location, no vortices will be generated and the performance losses resulting from flow separation will persist. Both Reynolds number and relative angle of attack are functions of rotational speed, which varies span-wise (radially) along the blade. Therefore, the separation chord location (and consequently the ideal SAVGJ array chord location) also varies as a function of span location. This information can be used to determine the optimal jet array angle (β) required to locate each jet at the appropriate chord location for a given span location.

Results from this study represent the effect of SAVGJ arrays on an airfoil shape in a 2D flow field. However, a propeller has rotational velocity which results in a 3D flow field. Although propellers are designed to minimize span-wise flow, there are still significant effects caused by the centripetal forces on the flow. This may be advantageous for the SAVGJ if the skew angle is oriented towards to propeller tip. Such orientation may cause the generated vortex to be stretched span-wise toward the propeller tip, promoting boundary layer energizing across a large portion of the propeller surface. However, the rotational velocity of the propeller may also cause the blade surface to be swept away from the vortex. In this scenario, the array would have no effect on the boundary layer separation and would also reduce the overall thrust of the propeller because pressure differential between the pressure and suction surfaces of the blade would be decreased due to the flow lost through the SAVGJ array.

Based on PIV results of the flow separation chord location, the optimal SAVGJ location for each Reynolds number can be calculated. Since Reynolds number varies radially along the propeller

blade, the optimal SAVGJ chord location also varies radially. This information can be captured in the jet array angle (β). For the propeller presented in this study operating at 8,000 RPM and 40 mph, a SAVGJ array with 4 jets that is centered at 50% span should be located at 23% chord with an array angle of 3.1°. The optimal array angle for other operating conditions may be calculated using the Matlab code in Appendix B.

5.2 Future Research

While this study examined the effect of chord location at various Reynolds numbers and angles of attack and successfully identified many conditions where vortices are generated, there remain 9 other SAVGJ parameters which should be explored. Most notably, inlet geometry and jet area ratio should be explored, as they most directly affect the jet momentum ratio. Maximizing the jet momentum ratio increases vortex strength and most effectively energizes the boundary layer, which ultimately results in propeller performance gains. In this study, the inlets were simple circular cross sections, which are known to be non-optimal geometry. In particular, the use of a converging inlet should be explored to optimize the air intake on the pressure side of the propeller. Related to this study is the effect of jet area ratio, which is dependent upon the inlet geometry. The jet area ratio should be chosen to achieve the desired jet momentum ratio while accounting for orifice flow losses, which will require and experimental data to calculate.

In addition to studying SAVGJ design parameters, implementation on different propeller geometries should also be studied. As the propeller diameter is decreased, the SAVGJ geometry must also decrease. At these smaller geometries, viscous forces will likely dominate the flow inside the flow channel between the inlet and jet, causing a significant reduction in jet momentum. As propeller diameter is increased, the effects of stress concentrations around the SAVGJ array features will be magnified. More detailed structural analysis will be required in to

design and manufacture propellers with integrated SAVGJ arrays that can withstand the centripetal loading caused by the rotational velocity component.

After significant progress has been made to optimize SAVGJ design parameters and integration techniques, flight tests should be conducted to validate range and endurance improvement estimates from dynamometer performance data. This data should then be used to construct carpet plots to be used for parameter selection when designing SAVGJ arrays for certain operating conditions.

The integration of a SAVGJ array into a propeller may increase propeller noise as the jets from the array will likely create a whistling noise. However, the magnitude of this noise may be indistinguishable from the overall propeller noise. Further, noise generated by the propeller may be reduced due to the wake filling effect of the vortices, which could potentially result in an overall noise reduction. To study this effect, the noise of a baseline propeller should be compared to the noise of a propeller with integrated SAVGJ array across a range of operating conditions. In particular, noise occurring at frequencies near the propeller rotational speed.

Previous studies have demonstrated that pulsed jets are more effective at manipulating flow than steady jets. A propeller with pulsed SAVGJ array could be achieved with the inclusion of a spring leaf value in the flow channel of the SAVGJ array. To achieve a desired pulsing frequency, the spring constant should be chosen based on the pressure at the inlet location and the pressure at the jet location, both of which are dependent upon operating conditions of the propeller. Further, the spring leaf could also be tuned to remain closed until a certain pressure differential is achieved, allowing the SAVGJ array to remain deactivated while boundary layer flow is attached. Such a system would be classified as passive flow control, while having the benefit of delayed activation which is typically only available to active flow control methods. This feature adds two additional design parameters which must be considered: activation pressure and pulsing frequency.

REFERENCES

"APC Performance Data." *APC*. N.p., n.d. Web. 27 Oct. 2017.

Deters, Robert W., Ananda, Gavin K., and Selig, Michael S. “Reynolds Number Effects on the Performance of Small-Scale Propellers,” *Applied Aerodynamics Conference, AIAA*, 32 (2014), 2014-2151.

Findanis, Ahmed, & Findanis, N. (2014). FLOW STUDIES OF A FORWARD SWEPT WING FITTED WITH ACTIVE FLOW CONTROL. *Advances and Application in Fluid Mechanics,15*(2), 163.

Freestone, M. ‘Preliminary tests at low speeds on the vorticity produced by air-jet vortex-generators’, Research Memo Aero. 85/1, City University London, Feb. 1985.

Gamble, Dustin Eli. “Automated Dynamic Propeller Testing at Low Reynolds Numbers,” Master’s Thesis, Oklahoma State University. Stillwater, Oklahoma, Dec. 2009.

Huang, Junhui, Thomas C. Corke, and Flint O. Thomas. "Unsteady plasma actuators for separation control of low-pressure turbine blades." *AIAA journal* 44.7 (2006): 1477-1487.

Johnston, J. P., & Nishi, M. (1990). Vortex generator jets-means for flow separation control. *AIAA journal*, *28*(6), 989-994.

Kline, S. J., and McClintock, F. A., "Describing Uncertainties in Single Sample Experiments," Mechanical Engineering, Jan. 1953.

Kordik, J., Brouckova, Z., & Travnicek, J. (2015). Impinging jet-based fluidic diodes for hybrid synthetic jet actuators. *Journal Of Visualization, 18*(3), 449-458.

Lin, J., Robinson, S., McGhee, R., & Valarezo, W. (1994). Separation Control on High-Lift Airfoils via Micro-Vortex Generators. *Journal of Aircraft, 31*(6), 1317.

Lin, JC Muti, and Laura L. Pauley. "Low-Reynolds-number separation on an airfoil." *AIAA journal* 34.8 (1996): 1570-1577.

McCormick, Barnes W. *Aerodynamics, Aeronautics, and Flight Mechanics*. 2nd ed. N.p.: Pennsylvania State U, 1994. Print.

McQuilling, Mark, and Jacob, Jamey. "Effect of Chord Location on Separation Control with Vortex Generator Jets on Low Pressure Turbine Blades," *Flow Control Conference, AIAA*, 2 (2004), 2004-2205.

Mueller, Thomas J., and Stephen M. Batill. "Experimental studies of separation on a two-dimensional airfoil at low Reynolds numbers." *AIAA journal* 20.4 (1982): 457-463.

Prince, S., Badalamenti, C., & Regas, C. (2017). The application of passive air jet vortex-generators to stall suppression on wind turbine blades. *Wind Energy, 20*(1), 109-123.

Roth, J. Reece, Daniel M. Sherman, and Stephen P. Wilkinson. *Boundary layer flow control with a one atmosphere uniform glow discharge surface plasma*. American Institute of Aeronautics and Astronautics, 1998.

Sciacchitano, Andrea, Wieneke, Bernhard, and Scarano, Fulvio. "PIV Uncertainty Quantification by Image Matching," Measurement Science and Technology, vol. 24, 2013, 2013-045302.

Seifert, A., Bachar, T., Koss, D., Shepshelovich, M., and Wyganski, I., 1993, "Oscillatory Blowing: A Tool to Delay Boundary-Layer Separation," AIAA Journal, Vol. 31, No. 11, pp. 2052-2060.

Seifert, A., Eliahu, S., Greenblatt, D., and Wygnanski, I., "Use of Piezoelectric Actuators for Airfoil Separation Control," *AIAA Journal*, vol. 36, 1998, pp. 1535–1537.

Shun, S., & Ahmed, N. (2011). Airfoil Separation Control Using Multiple-Orifice Air-Jet Vortex Generators. *Journal of Aircraft, 48*(6), 2164-2169.

Sondergaard, Rolf, Richard B. Rivir, and Jeffrey P. Bons. "Control of low-pressure turbine separation using vortex-generator jets." *Journal of propulsion and power* 18.4 (2002): 889-895.

Tilmann, Carl P., Langan, Kevin J., Betterton, John G., and Wilson, Mark J. "Characterization of Pulsed Vortex Generator Jets for Active Flow Control," RTO AVT Symposium, Braunschweig, Germany, May 2000.

Uhlig, Daniel V., and Selig, Michael S. "Post Stall Propeller Behavior at Low Reynolds Numbers," *Aerospace Sciences Meeting and Exhibit, AIAA*, 46 (2008), 2008-407.

Volino, & Ibrahim. (2012). Separation control on high lift low-pressure turbine airfoils using pulsed vortex generator jets. *Applied Thermal Engineering, 49*, 31-40.

Volino, R., & Ashpis, D. (2005). Synthetic Vortex Generator Jets Used to Control Separation on Low-Pressure Turbine Airfoils. *Research and Technology 2004,* (Ogy 2004), Research and Technology 2004; NASA/TM-2005-213419.

Volino, Ralph J. "Passive flow control on low-pressure turbine airfoils." *ASME Turbo Expo 2003, collocated with the 2003 International Joint Power Generation Conference*. American Society of Mechanical Engineers, 2003.

Volino, Ralph J. "Passive flow control on low-pressure turbine airfoils." *ASME Turbo Expo 2003, collocated with the 2003 International Joint Power Generation Conference*. American Society of Mechanical Engineers, 2003.

Warsop, Clyde, Hucker, Martyn, Press, Andrew J., and Dawson, Paul. "Pulsed Air-Jet Actuator for Flow Separation Control." *Flow Turbulence Combustion* 78 (2007): 255-281.

APPENDIX A – Raw PIV Images

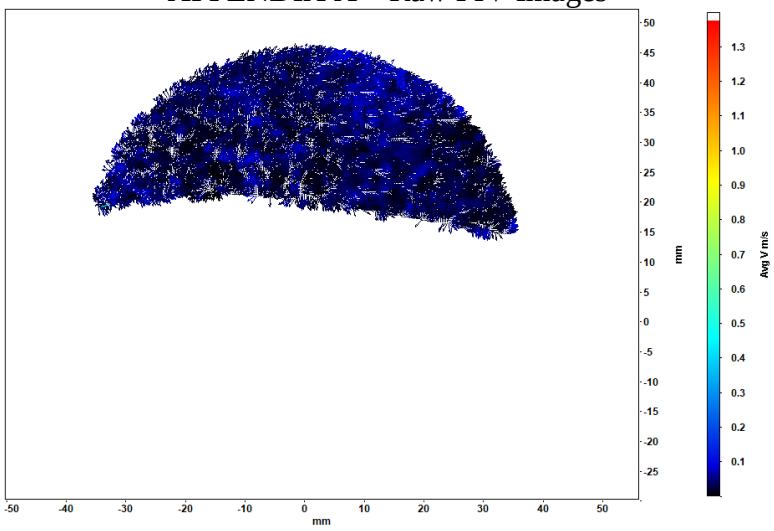

Figure 48. PIV Vector Image of Scaled Airfoil without SAVGJ Array, 0° Angle of Attack, and 15,000 Reynolds Number

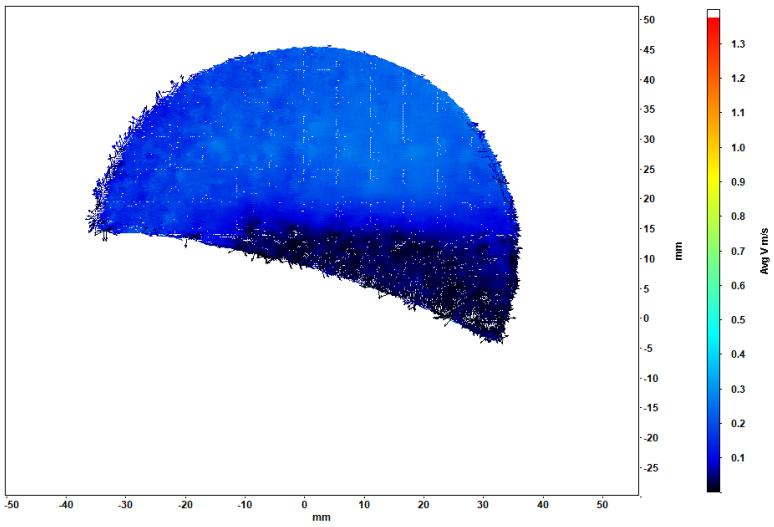

Figure 49. PIV Vector Image of Scaled Airfoil without SAVGJ Array, 15° Angle of Attack, and 15,000 Reynolds Number

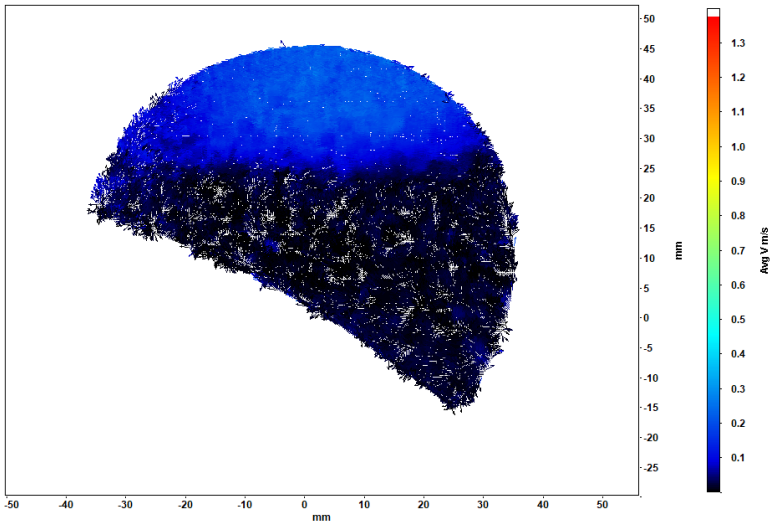

Figure 50. PIV Vector Image of Scaled Airfoil without SAVGJ Array, 30° Angle of Attack, and 15,000 Reynolds Number

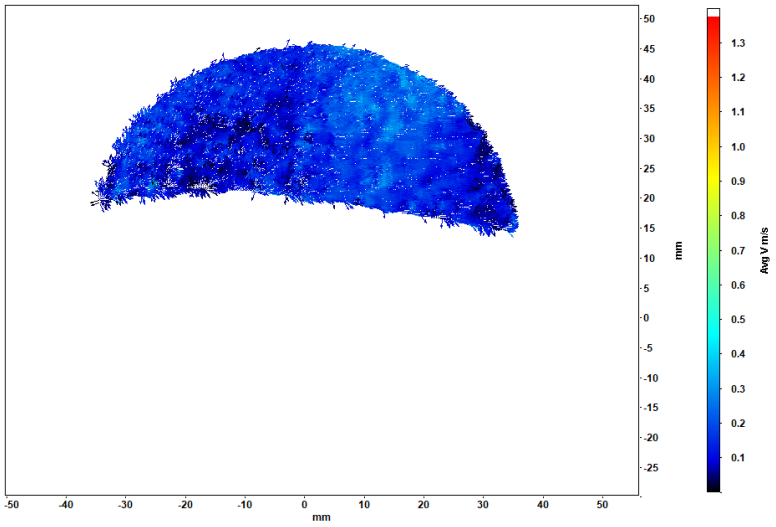

Figure 51. PIV Vector Image of Scaled Airfoil without SAVGJ Array, 0° Angle of Attack, and 30,000 Reynolds Number

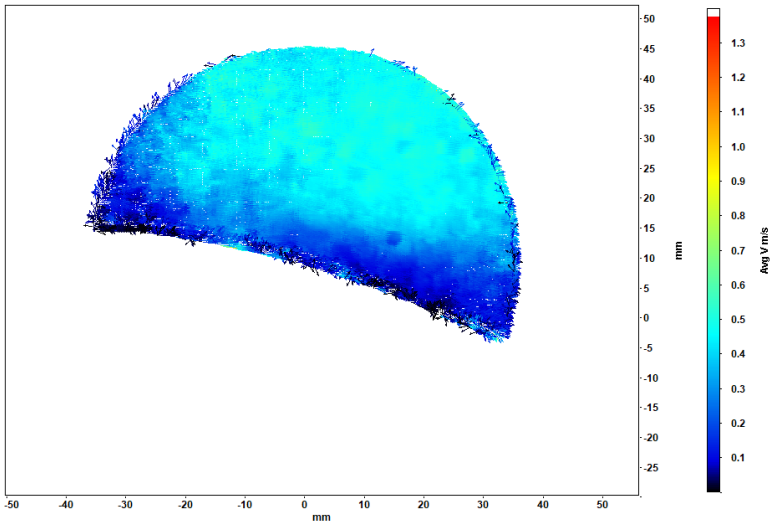

Figure 52. PIV Vector Image of Scaled Airfoil without SAVGJ Array, 15° Angle of Attack, and 30,000 Reynolds Number

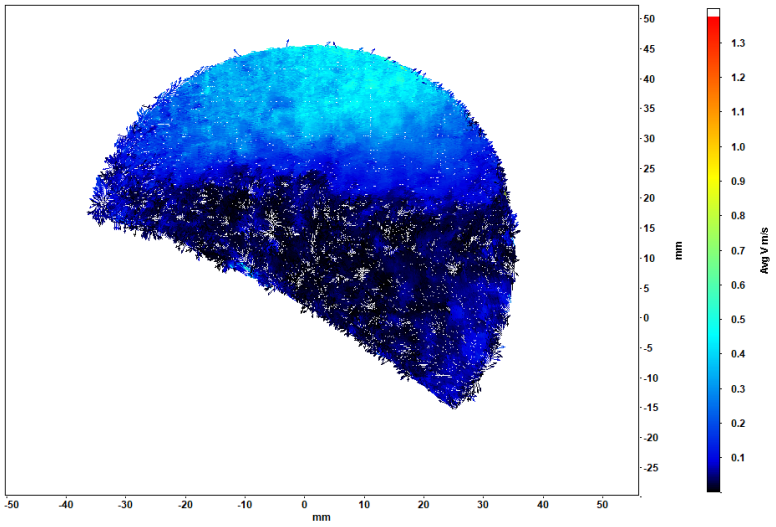

Figure 53. PIV Vector Image of Scaled Airfoil without SAVGJ Array, 30° Angle of Attack, and 30,000 Reynolds Number

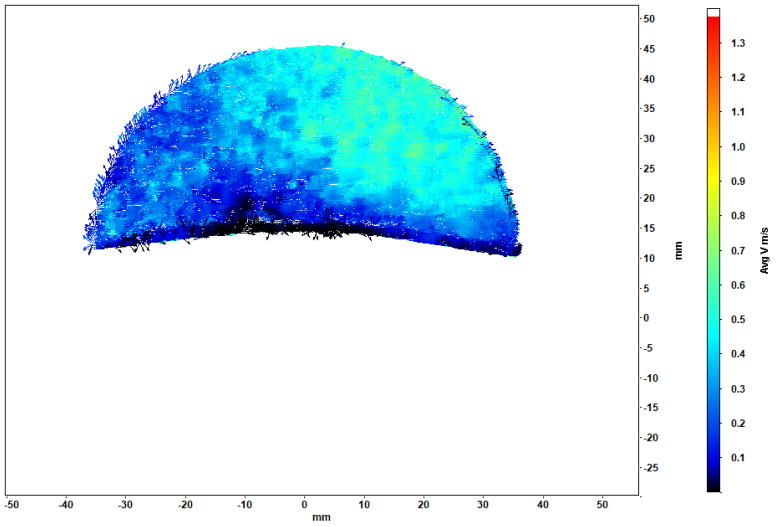

Figure 54. PIV Vector Image of Scaled Airfoil without SAVGJ Array, 0° Angle of Attack, and 45,000 Reynolds Number

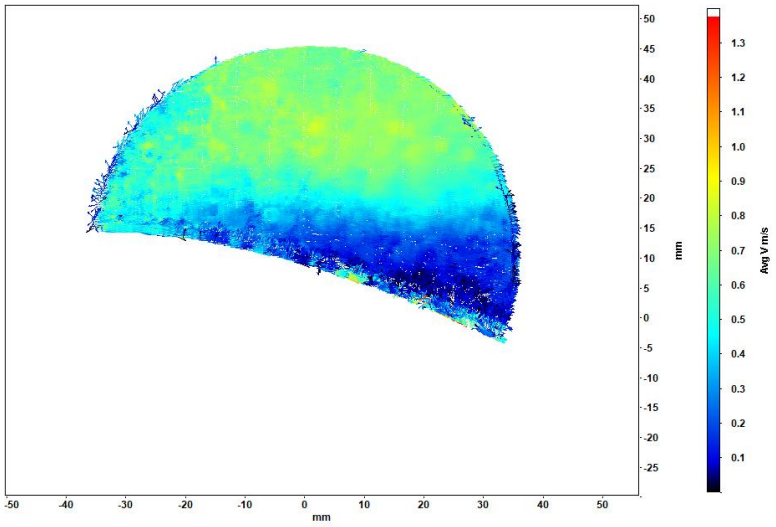

Figure 55. PIV Vector Image of Scaled Airfoil without SAVGJ Array, 15° Angle of Attack, and 45,000 Reynolds Number

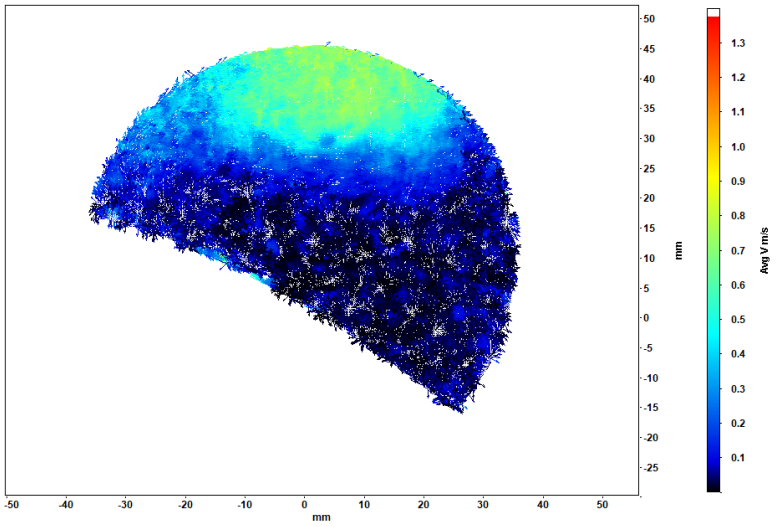

Figure 56. PIV Vector Image of Scaled Airfoil without SAVGJ Array, 30° Angle of Attack, and 45,000 Reynolds Number

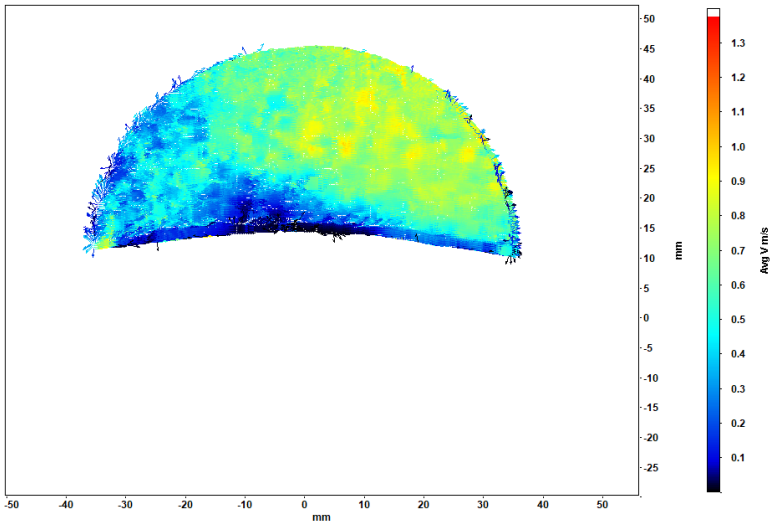

Figure 57. PIV Vector Image of Scaled Airfoil without SAVGJ Array, 0° Angle of Attack, and 60,000 Reynolds Number

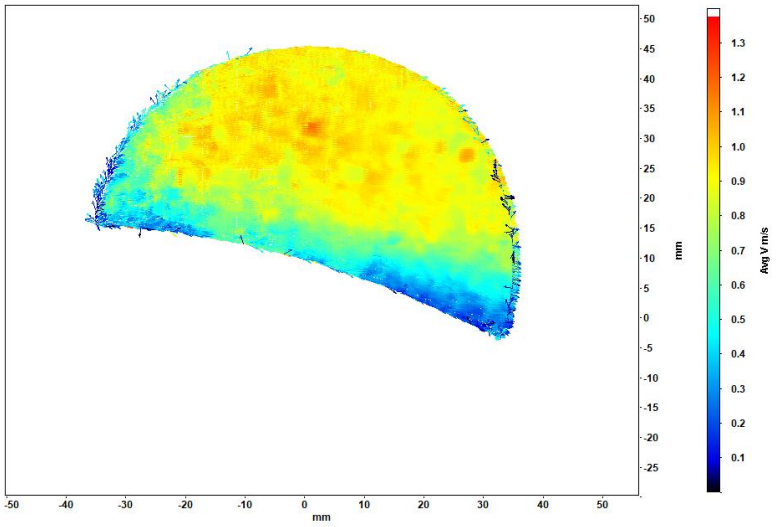

Figure 58. PIV Vector Image of Scaled Airfoil without SAVGJ Array, 15° Angle of Attack, and 60,000 Reynolds Number

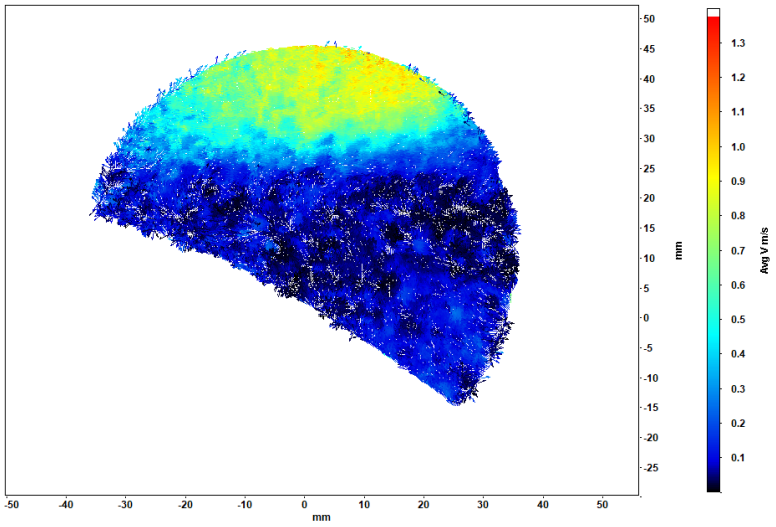

Figure 59. PIV Vector Image of Scaled Airfoil without SAVGJ Array, 30° Angle of Attack, and 60,000 Reynolds Number

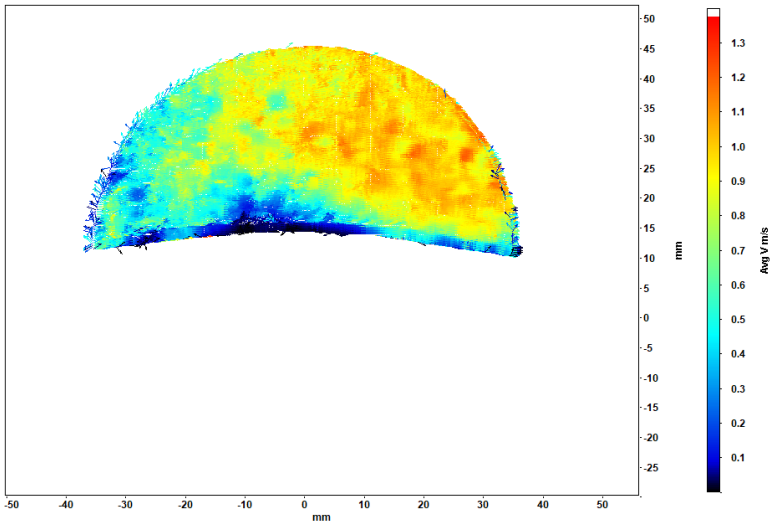

Figure 60. PIV Vector Image of Scaled Airfoil without SAVGJ Array, 0° Angle of Attack, and 75,000 Reynolds Number

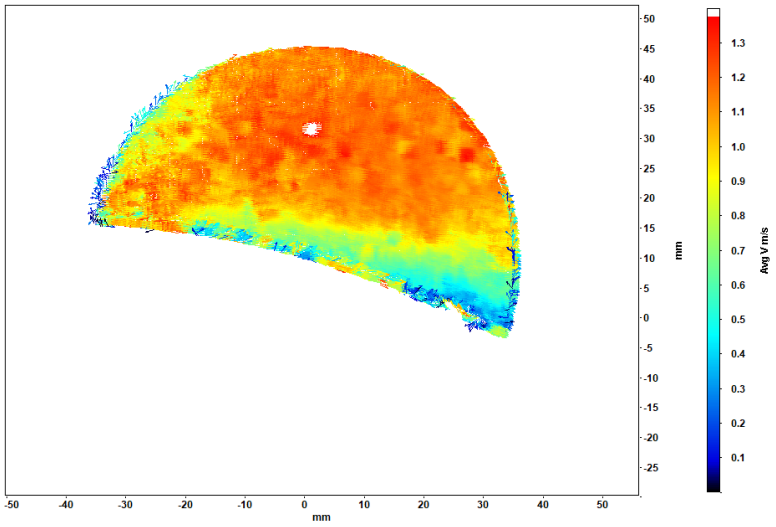

Figure 61. PIV Vector Image of Scaled Airfoil without SAVGJ Array, 15° Angle of Attack, and 75,000 Reynolds Number

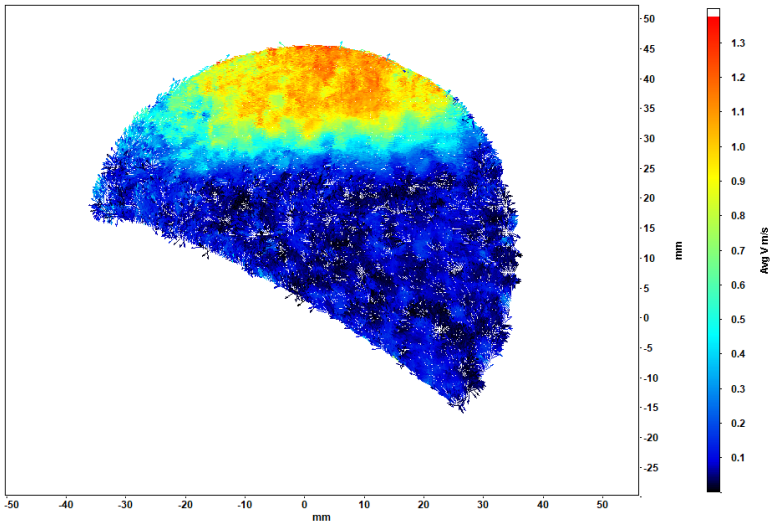

Figure 62. PIV Vector Image of Scaled Airfoil without SAVGJ Array, 30° Angle of Attack, and 75,000 Reynolds Number

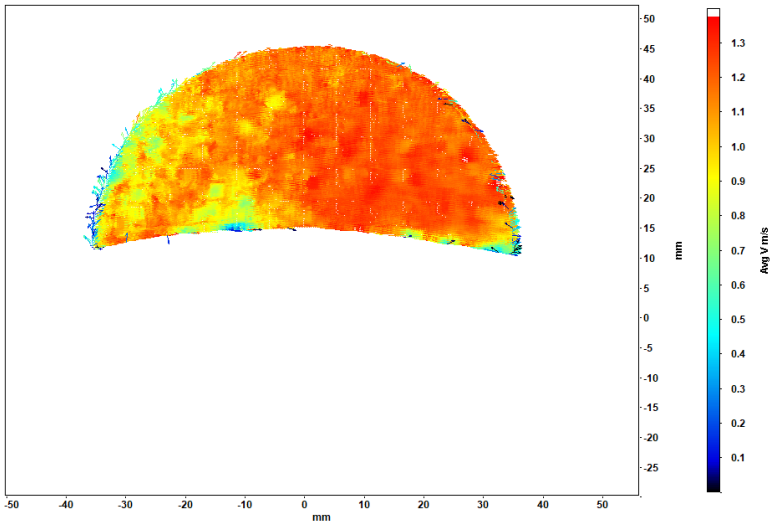

Figure 63. PIV Vector Image of Scaled Airfoil without SAVGJ Array, 0° Angle of Attack, and 90,000 Reynolds Number

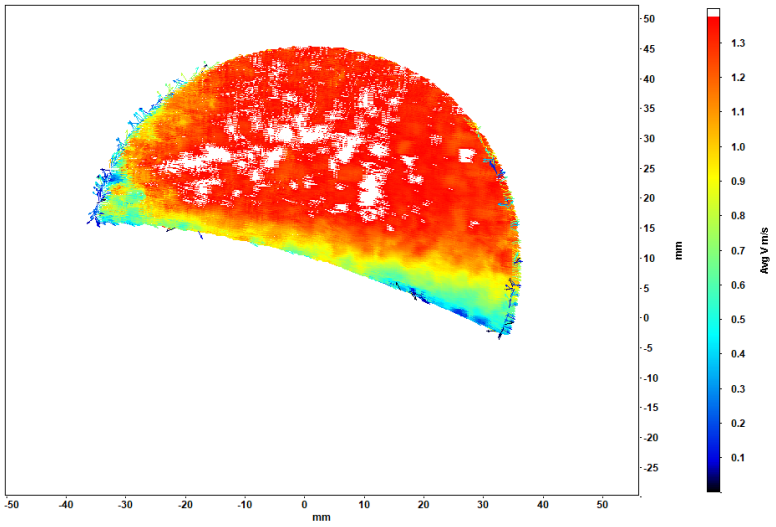

Figure 64. PIV Vector Image of Scaled Airfoil without SAVGJ Array, 15° Angle of Attack, and 90,000 Reynolds Number

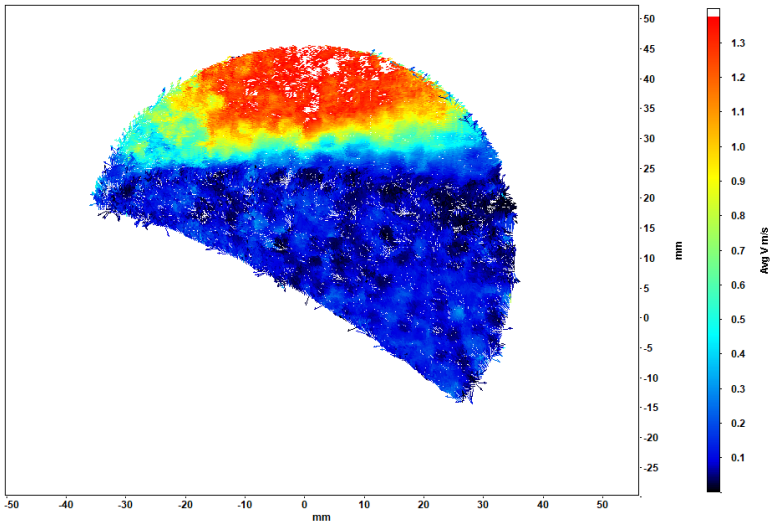

Figure 65. PIV Vector Image of Scaled Airfoil without SAVGJ Array, 30° Angle of Attack, and 90,000 Reynolds Number

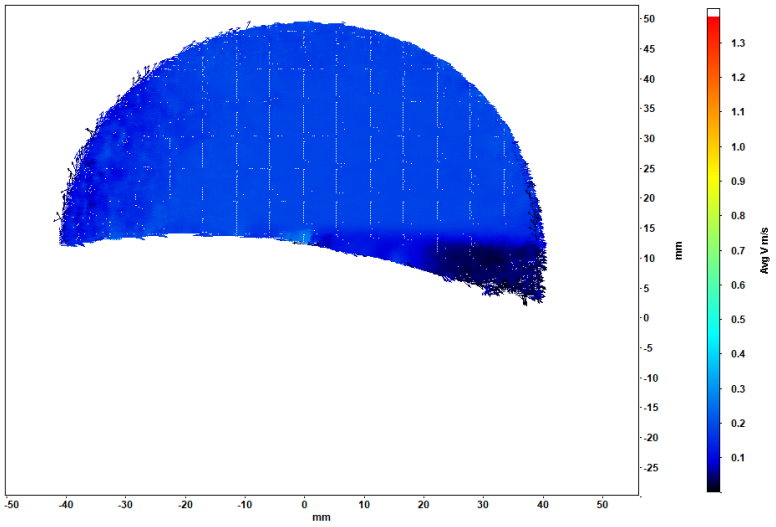

Figure 66. PIV Vector Image of Scaled Airfoil with SAVGJ Array at 40% Chord, 0° Angle of Attack, and 15,000 Reynolds Number

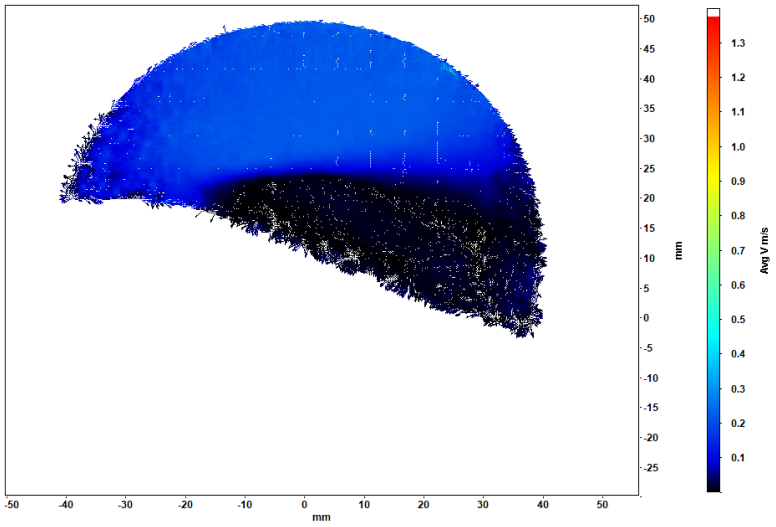

Figure 67. PIV Vector Image of Scaled Airfoil with SAVGJ Array at 40% Chord, 15° Angle of Attack, and 15,000 Reynolds Number

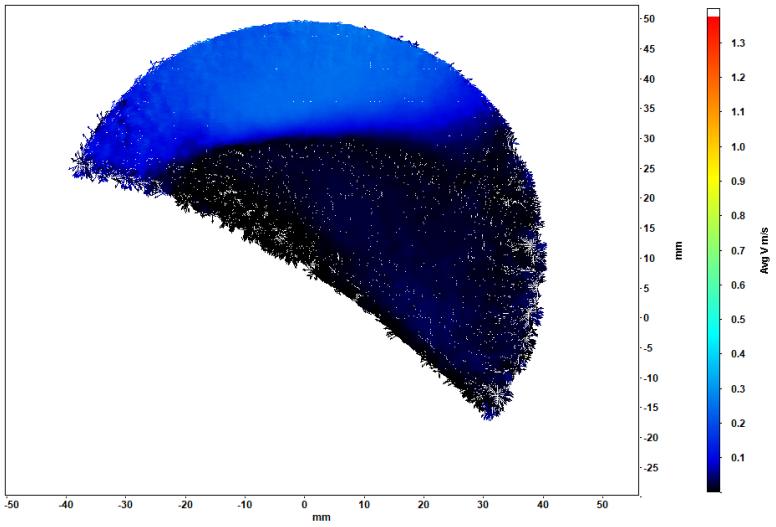

Figure 68. PIV Vector Image of Scaled Airfoil with SAVGJ Array at 40% Chord, 30° Angle of Attack, and 15,000 Reynolds Number

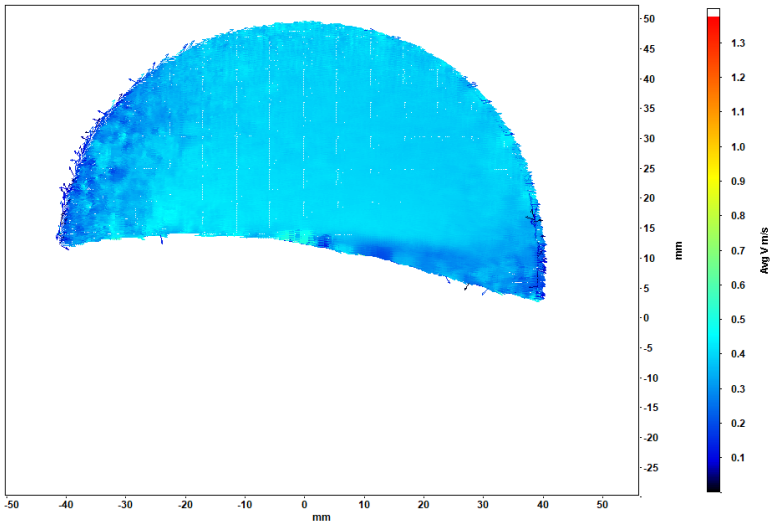

Figure 69. PIV Vector Image of Scaled Airfoil with SAVGJ Array at 40% Chord, 0° Angle of Attack, and 30,000 Reynolds Number

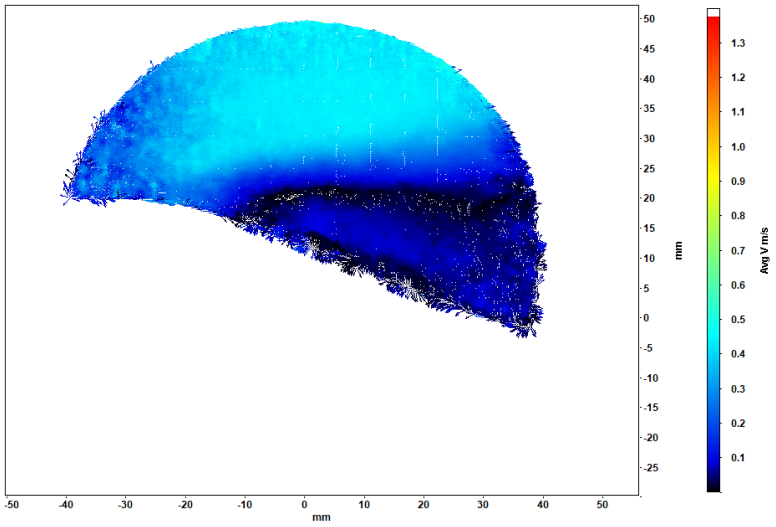

Figure 70. PIV Vector Image of Scaled Airfoil with SAVGJ Array at 40% Chord, 15° Angle of Attack, and 30,000 Reynolds Number

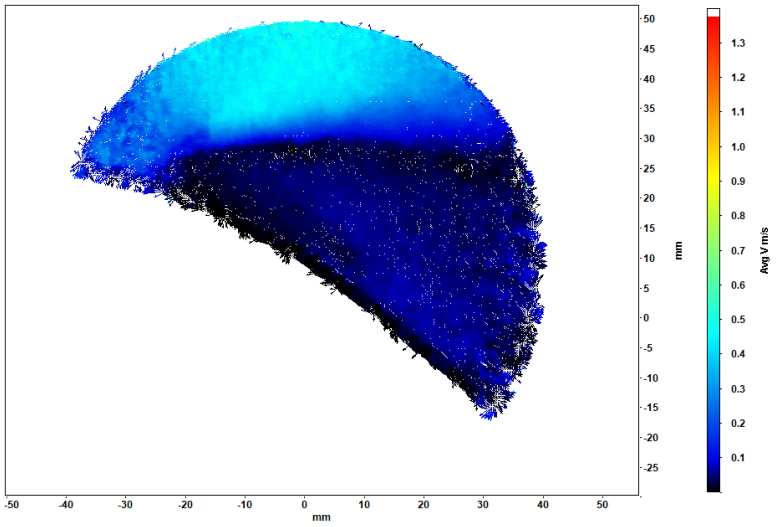

Figure 71. PIV Vector Image of Scaled Airfoil with SAVGJ Array at 40% Chord, 30° Angle of Attack, and 30,000 Reynolds Number

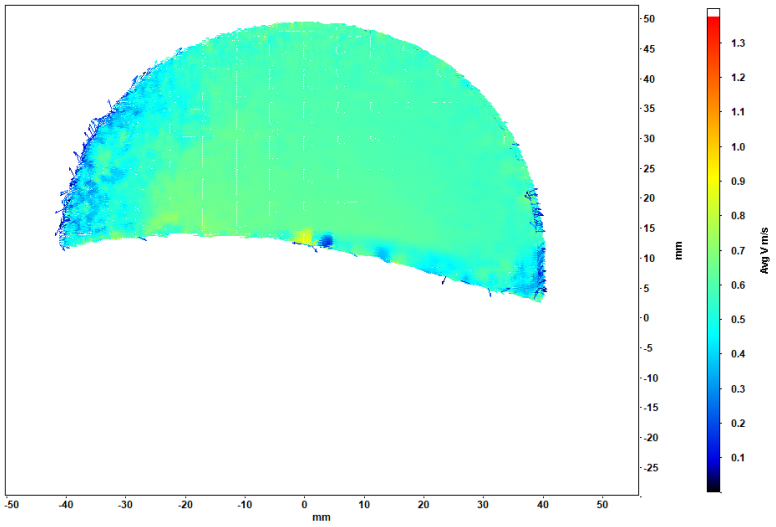

Figure 72. PIV Vector Image of Scaled Airfoil with SAVGJ Array at 40% Chord, 0° Angle of Attack, and 45,000 Reynolds Number

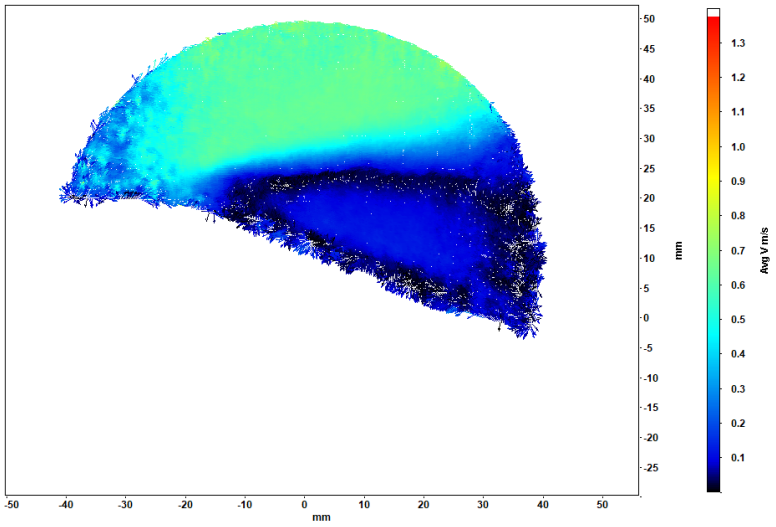

Figure 73. PIV Vector Image of Scaled Airfoil with SAVGJ Array at 40% Chord, 15° Angle of Attack, and 45,000 Reynolds Number

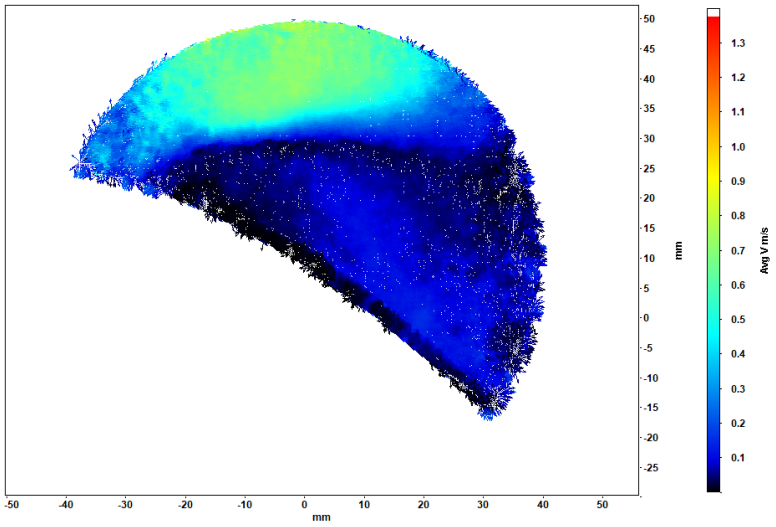

Figure 74. PIV Vector Image of Scaled Airfoil with SAVGJ Array at 40% Chord, 30° Angle of Attack, and 45,000 Reynolds Number

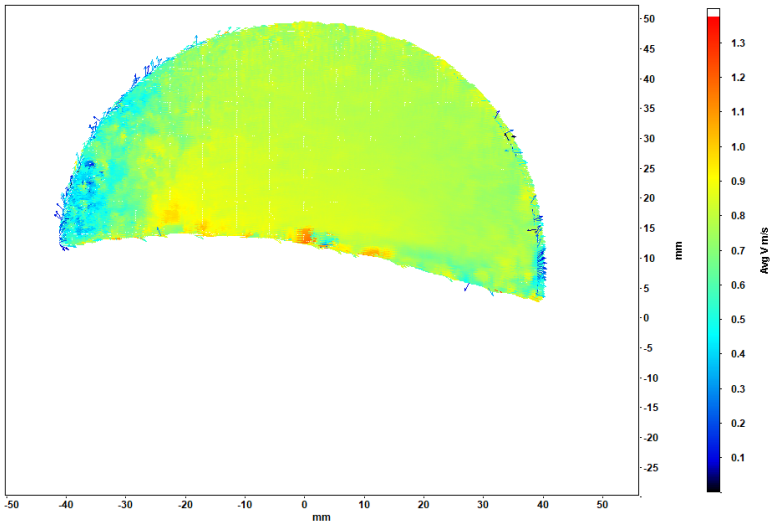

Figure 75. PIV Vector Image of Scaled Airfoil with SAVGJ Array at 40% Chord, 0° Angle of Attack, and 60,000 Reynolds Number

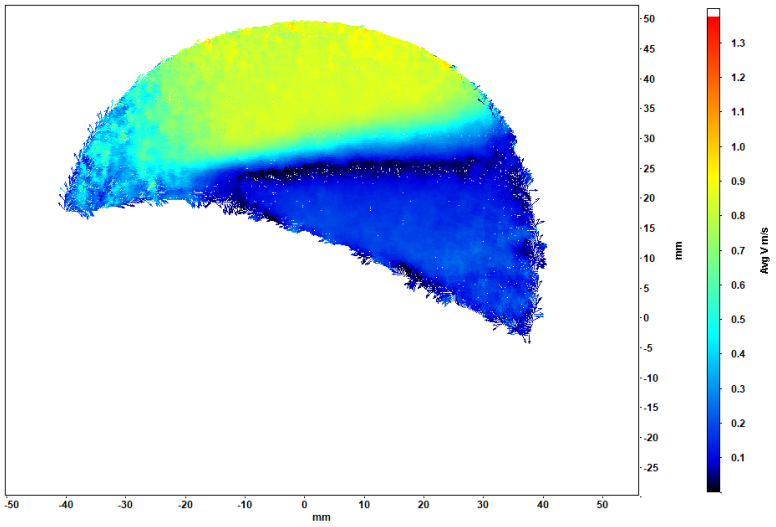

Figure 76. PIV Vector Image of Scaled Airfoil with SAVGJ Array at 40% Chord, 15° Angle of Attack, and 60,000 Reynolds Number

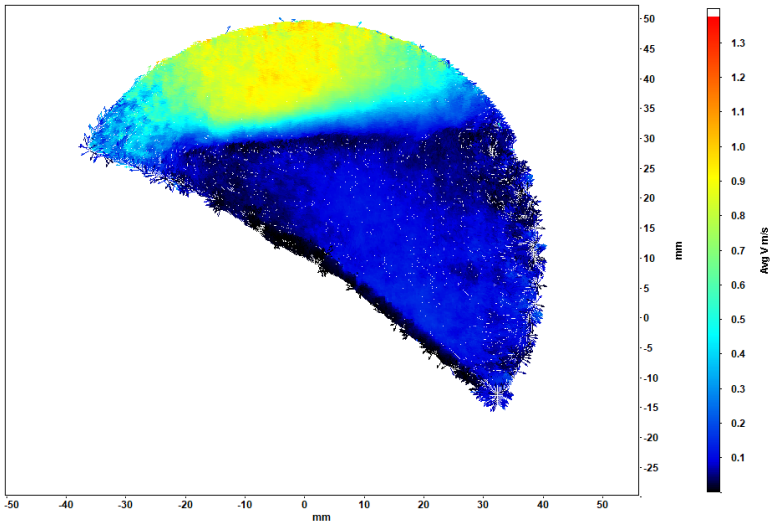

Figure 77. PIV Vector Image of Scaled Airfoil with SAVGJ Array at 40% Chord, 30° Angle of Attack, and 30,000 Reynolds Number

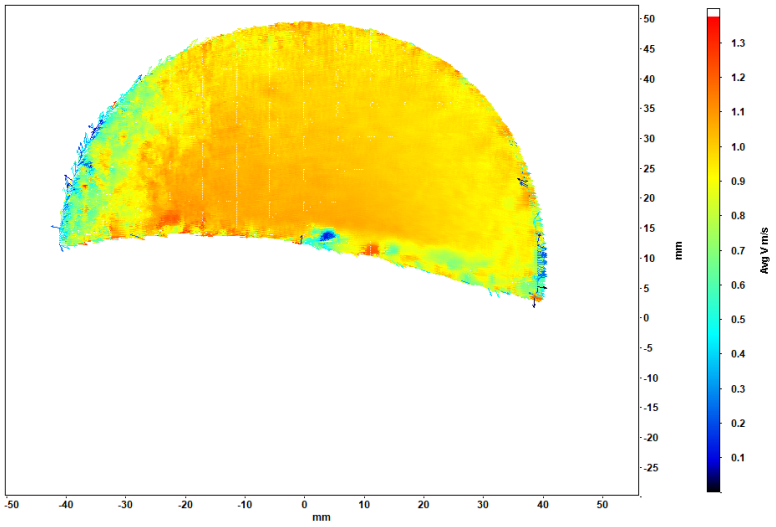

Figure 78. PIV Vector Image of Scaled Airfoil with SAVGJ Array at 40% Chord, 0° Angle of Attack, and 75,000 Reynolds Number

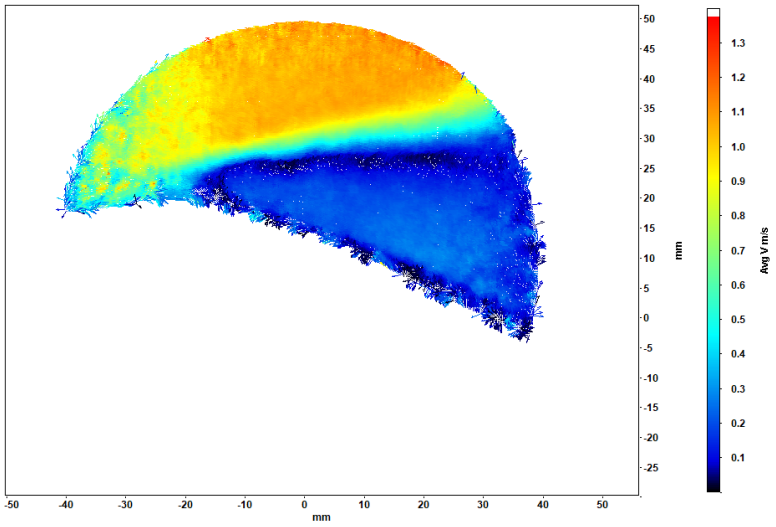

Figure 79. PIV Vector Image of Scaled Airfoil with SAVGJ Array at 40% Chord, 15° Angle of Attack, and 75,000 Reynolds Number

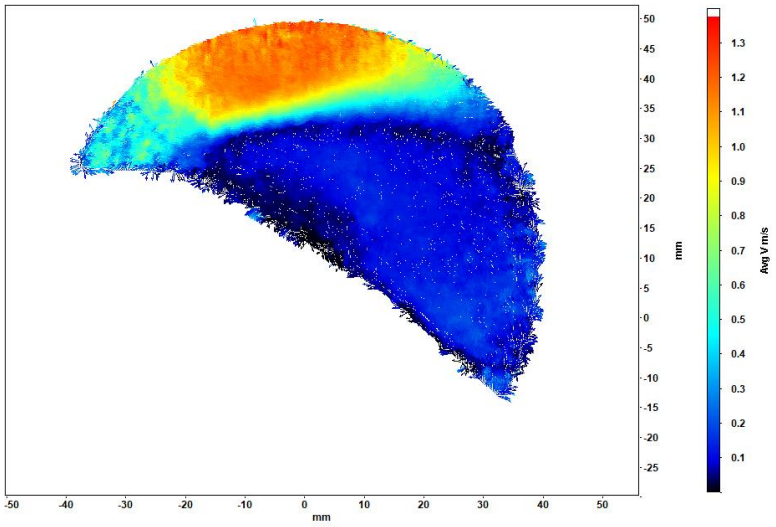

Figure 80. PIV Vector Image of Scaled Airfoil with SAVGJ Array at 40% Chord, 30° Angle of Attack, and 75,000 Reynolds Number

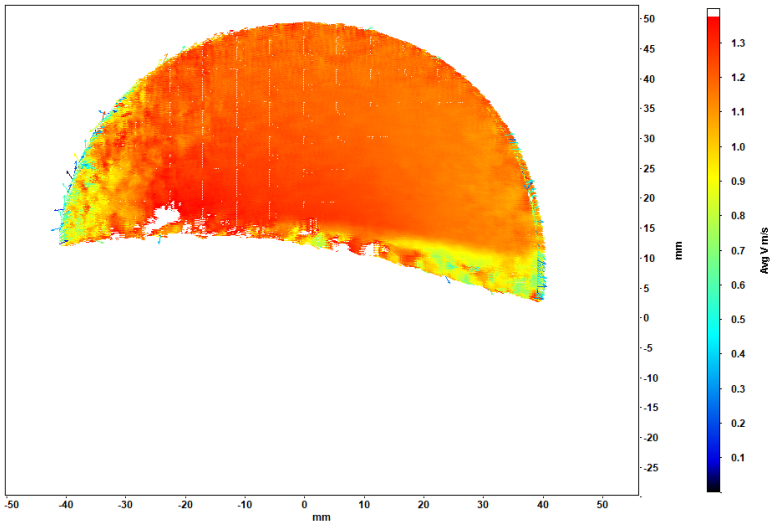

Figure 81. PIV Vector Image of Scaled Airfoil with SAVGJ Array at 40% Chord, 0° Angle of Attack, and 90,000 Reynolds Number

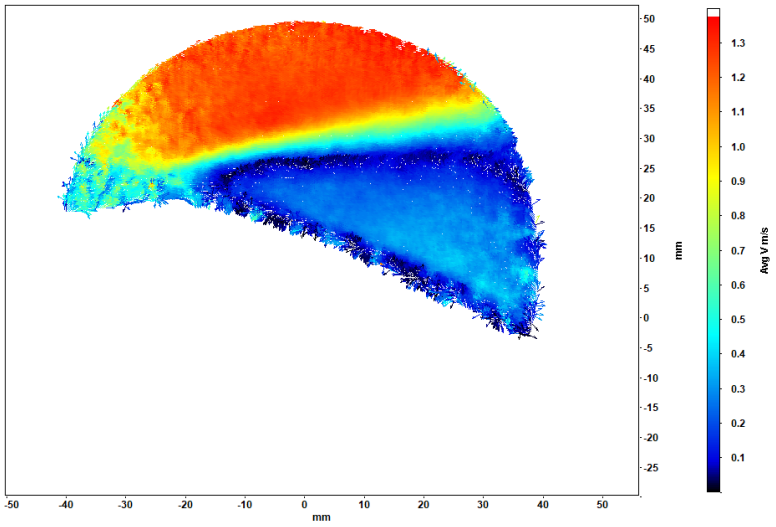

Figure 82. PIV Vector Image of Scaled Airfoil with SAVGJ Array at 40% Chord, 15° Angle of Attack, and 90,000 Reynolds Number

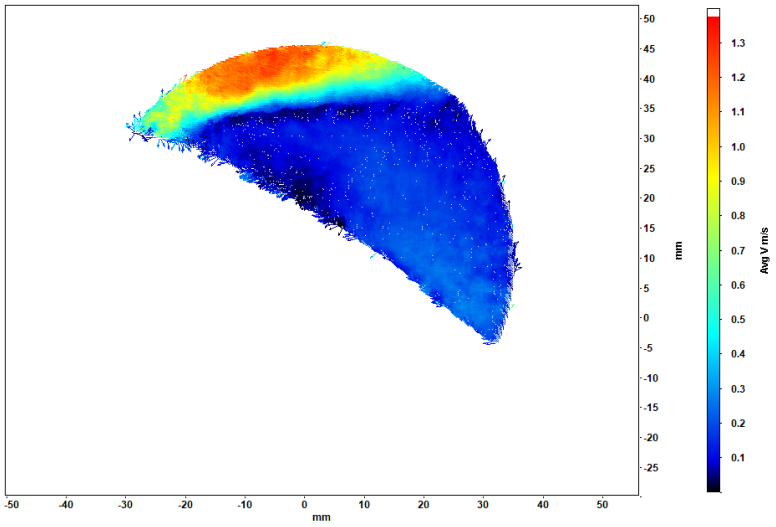

Figure 83. PIV Vector Image of Scaled Airfoil with SAVGJ Array at 40% Chord, 30° Angle of Attack, and 90,000 Reynolds Number

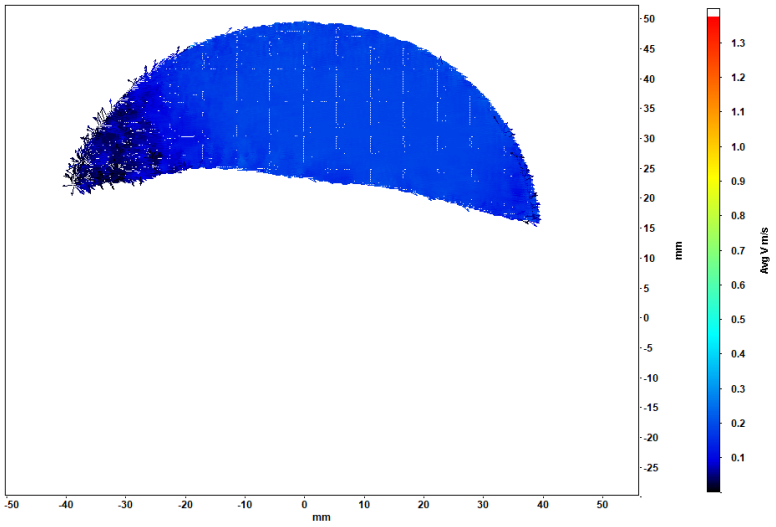

Figure 84. PIV Vector Image of Scaled Airfoil with SAVGJ Array at 50% Chord, 0° Angle of Attack, and 15,000 Reynolds Number

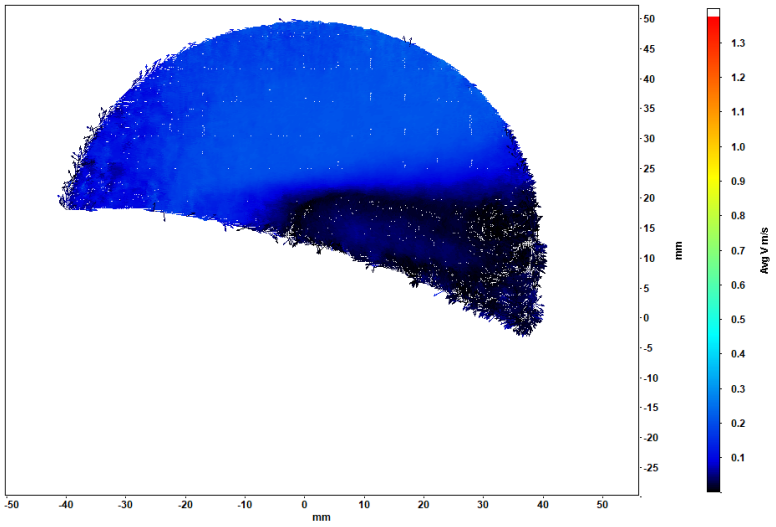

Figure 85. PIV Vector Image of Scaled Airfoil with SAVGJ Array at 50% Chord, 15° Angle of Attack, and 15,000 Reynolds Number

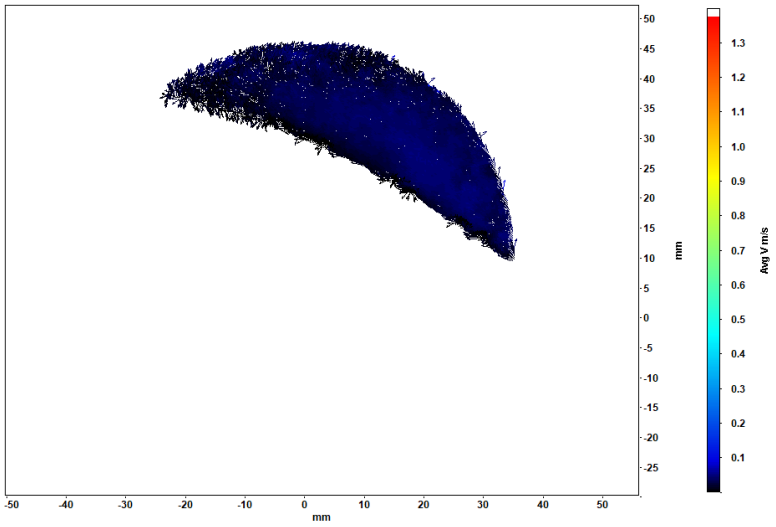

Figure 86. PIV Vector Image of Scaled Airfoil with SAVGJ Array at 50% Chord, 30° Angle of Attack, and 15,000 Reynolds Number

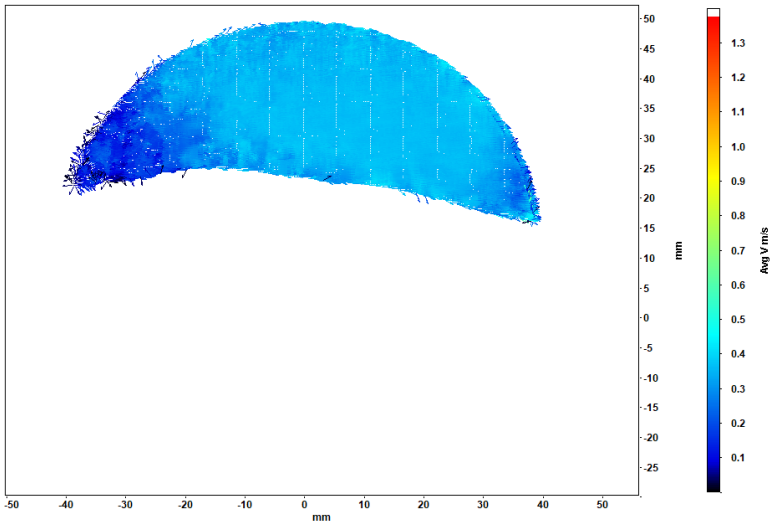

Figure 87. PIV Vector Image of Scaled Airfoil with SAVGJ Array at 50% Chord, 0° Angle of Attack, and 30,000 Reynolds Number

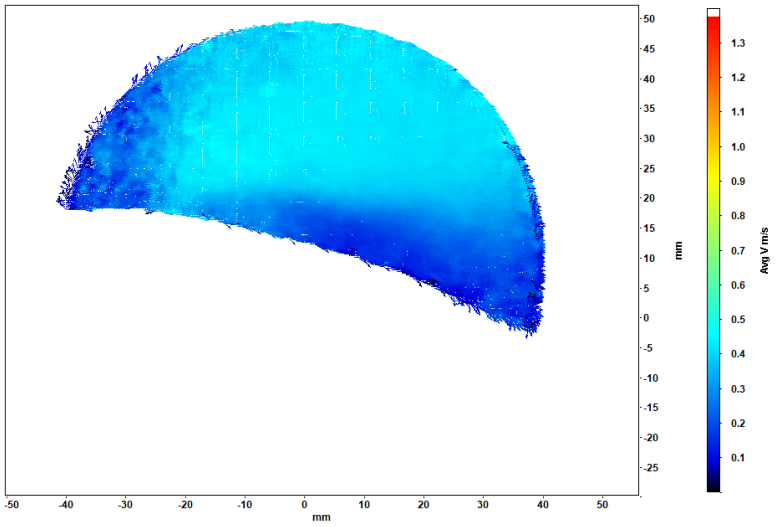

Figure 88. PIV Vector Image of Scaled Airfoil with SAVGJ Array at 50% Chord, 15° Angle of Attack, and 30,000 Reynolds Number

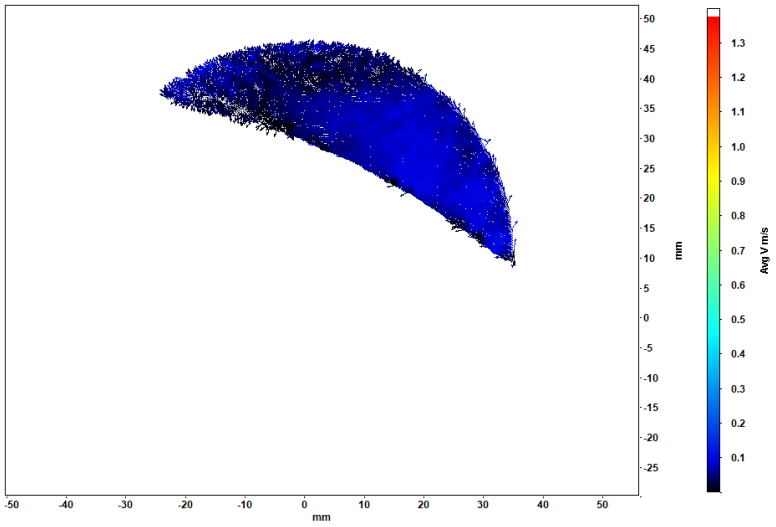

Figure 89. PIV Vector Image of Scaled Airfoil with SAVGJ Array at 50% Chord, 30° Angle of Attack, and 30,000 Reynolds Number

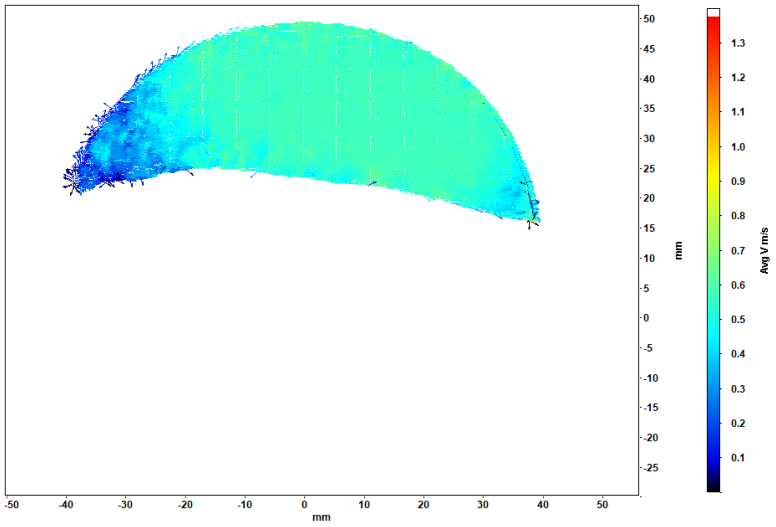

Figure 90. PIV Vector Image of Scaled Airfoil with SAVGJ Array at 50% Chord, 0° Angle of Attack, and 45,000 Reynolds Number

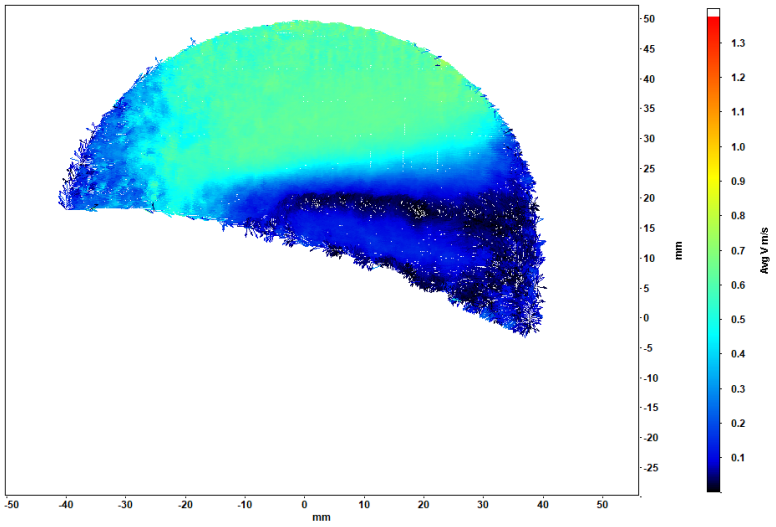

Figure 91. PIV Vector Image of Scaled Airfoil with SAVGJ Array at 50% Chord, 15° Angle of Attack, and 45,000 Reynolds Number

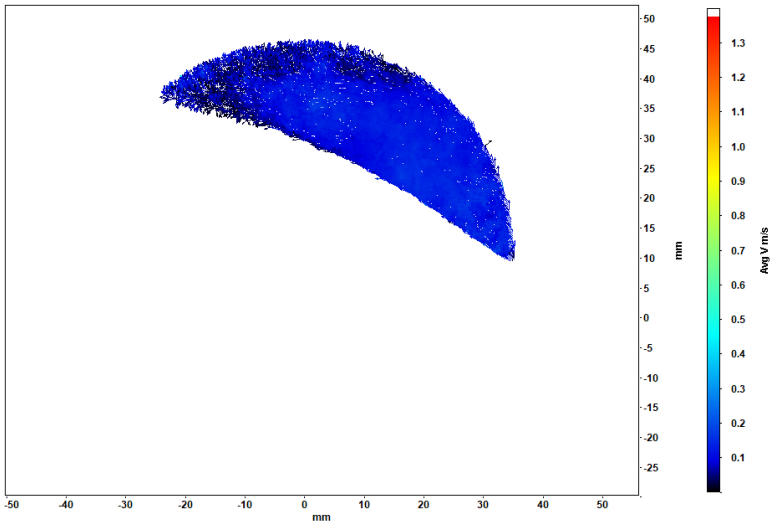

Figure 92. PIV Vector Image of Scaled Airfoil with SAVGJ Array at 50% Chord, 30° Angle of Attack, and 45,000 Reynolds Number

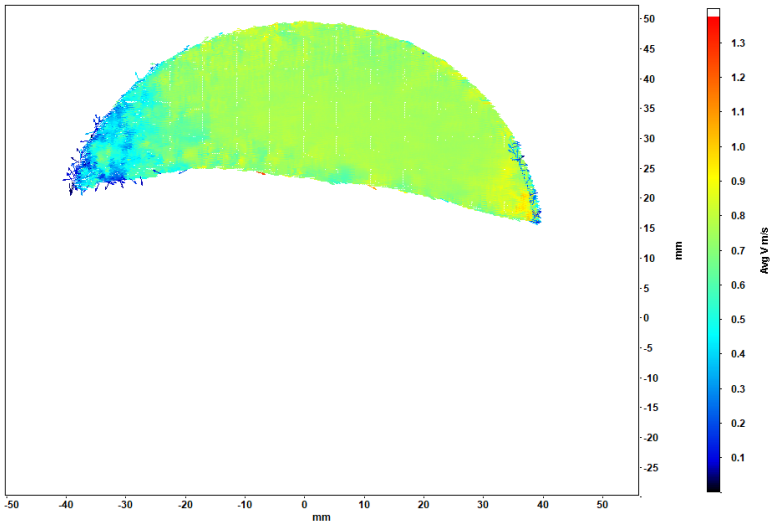

Figure 93. PIV Vector Image of Scaled Airfoil with SAVGJ Array at 50% Chord, 0° Angle of Attack, and 60,000 Reynolds Number

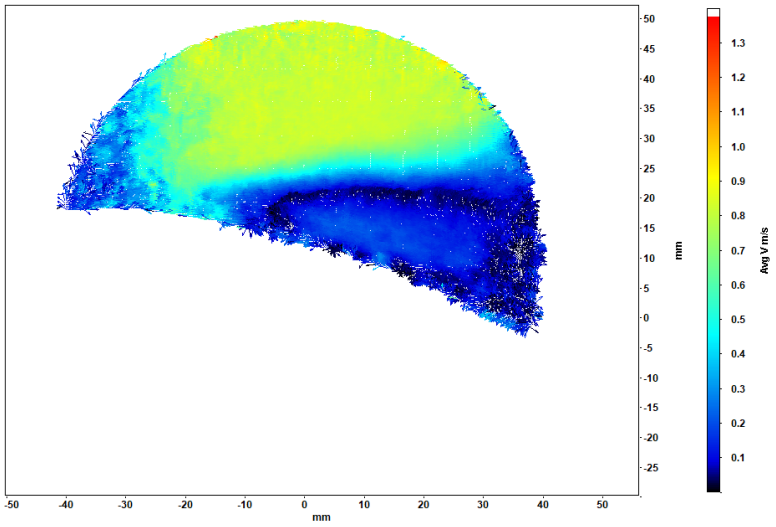

Figure 94. PIV Vector Image of Scaled Airfoil with SAVGJ Array at 50% Chord, 15° Angle of Attack, and 60,000 Reynolds Number

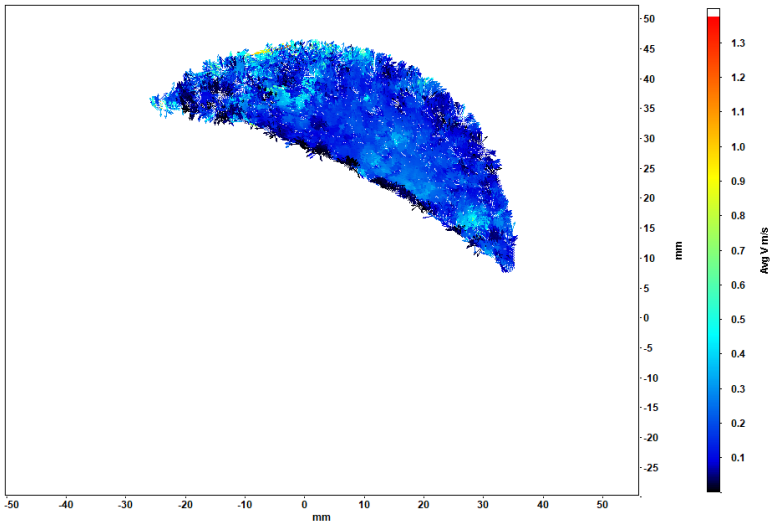

Figure 95. PIV Vector Image of Scaled Airfoil with SAVGJ Array at 50% Chord, 30° Angle of Attack, and 60,000 Reynolds Number

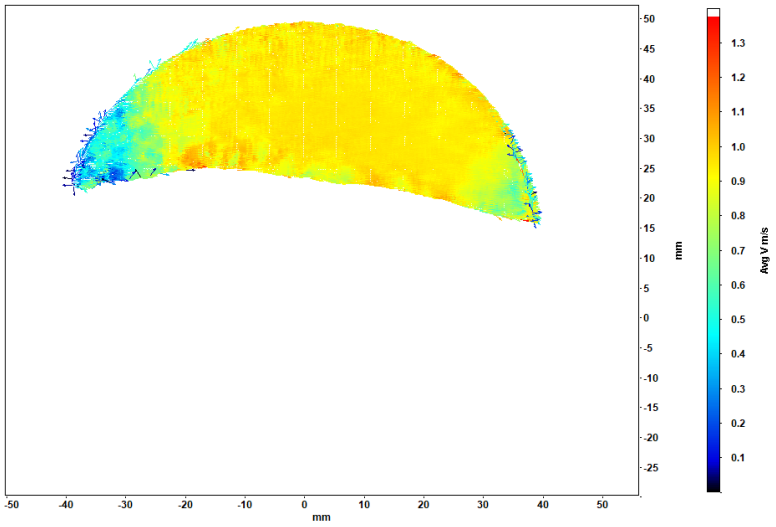

Figure 96. PIV Vector Image of Scaled Airfoil with SAVGJ Array at 50% Chord, 0° Angle of Attack, and 75,000 Reynolds Number

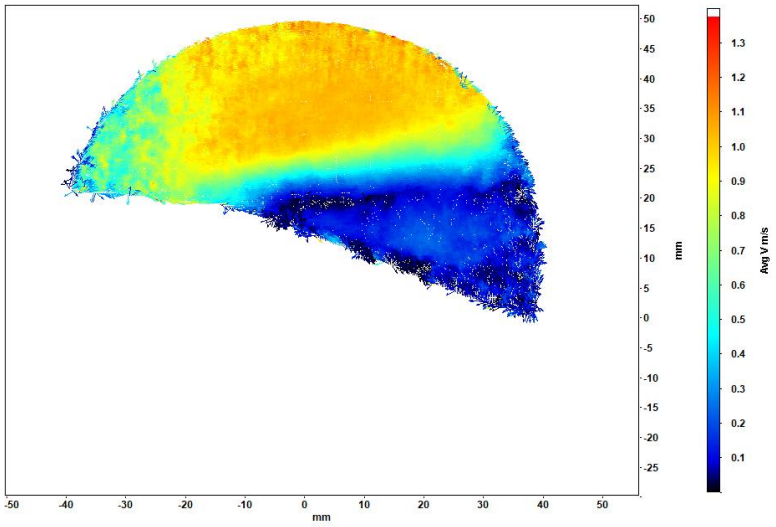

Figure 97. PIV Vector Image of Scaled Airfoil with SAVGJ Array at 50% Chord, 15° Angle of Attack, and 75,000 Reynolds Number

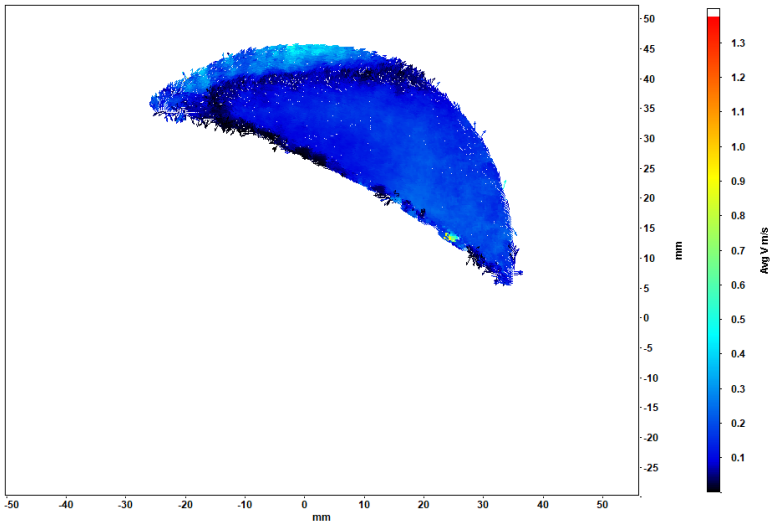

Figure 98. PIV Vector Image of Scaled Airfoil with SAVGJ Array at 50% Chord, 30° Angle of Attack, and 75,000 Reynolds Number

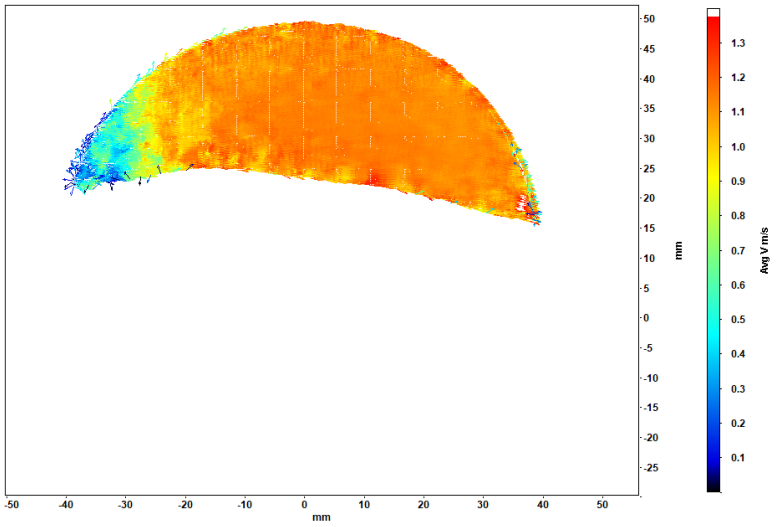

Figure 99. PIV Vector Image of Scaled Airfoil with SAVGJ Array at 50% Chord, 0° Angle of Attack, and 90,000 Reynolds Number

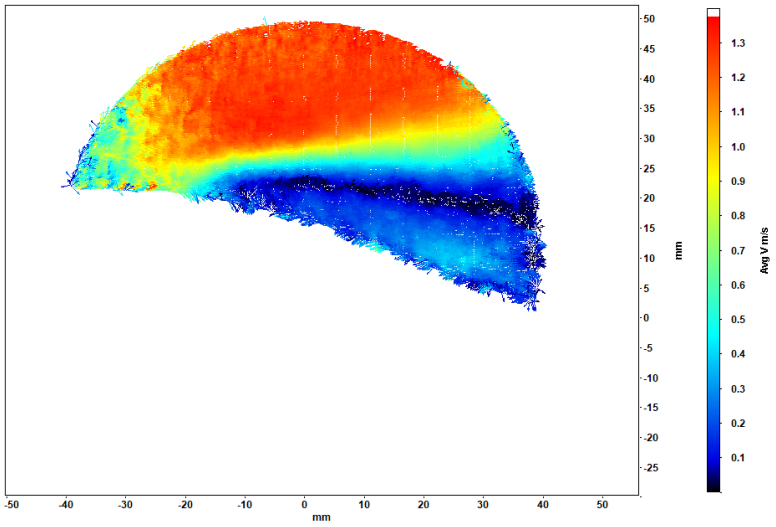

Figure 100. PIV Vector Image of Scaled Airfoil with SAVGJ Array at 50% Chord, 15° Angle of Attack, and 90,000 Reynolds Number

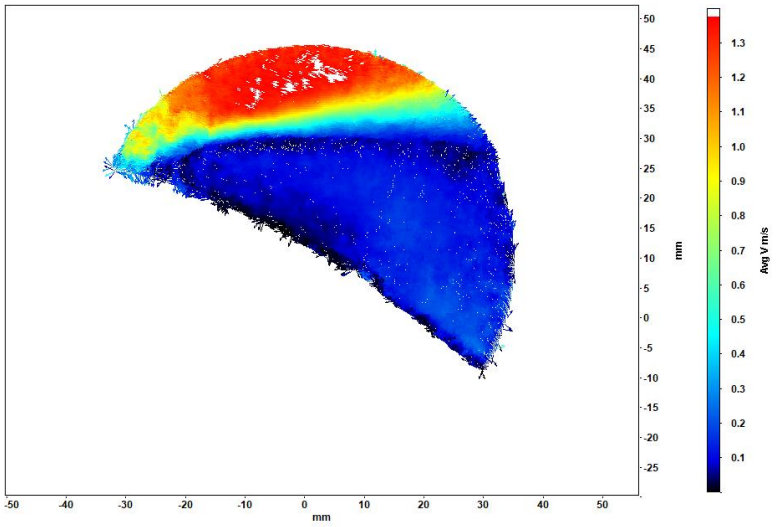

Figure 101. PIV Vector Image of Scaled Airfoil with SAVGJ Array at 50% Chord, 30° Angle of Attack, and 90,000 Reynolds Number

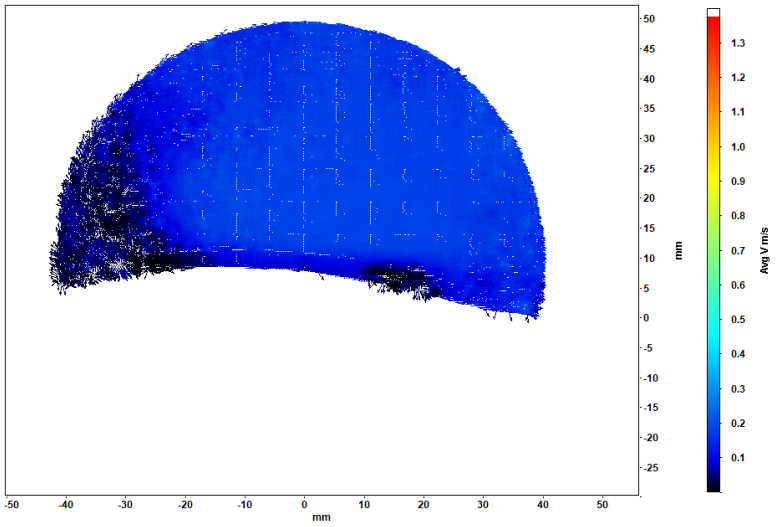

Figure 102. PIV Vector Image of Scaled Airfoil with SAVGJ Array at 60% Chord, 0° Angle of Attack, and 15,000 Reynolds Number

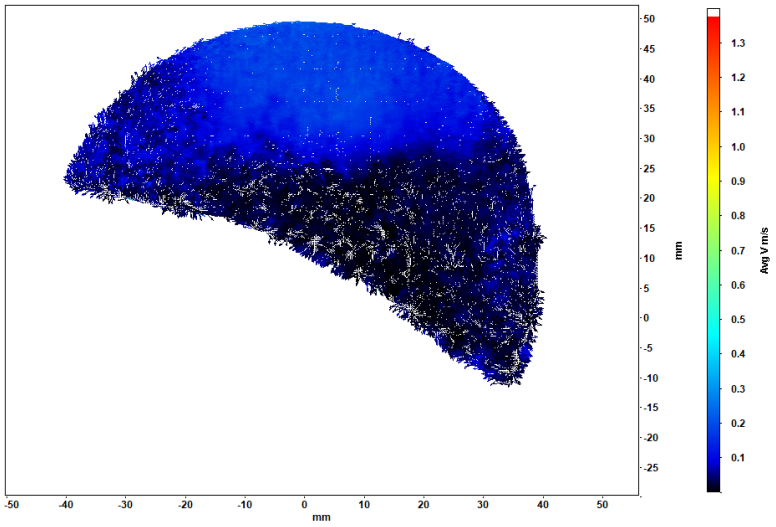

Figure 103. PIV Vector Image of Scaled Airfoil with SAVGJ Array at 60% Chord, 15° Angle of Attack, and 15,000 Reynolds Number

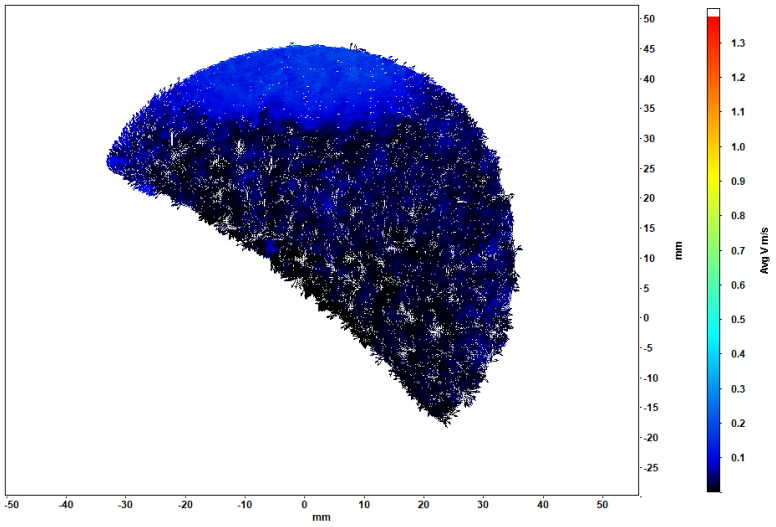

Figure 104. PIV Vector Image of Scaled Airfoil with SAVGJ Array at 60% Chord, 30° Angle of Attack, and 15,000 Reynolds Number

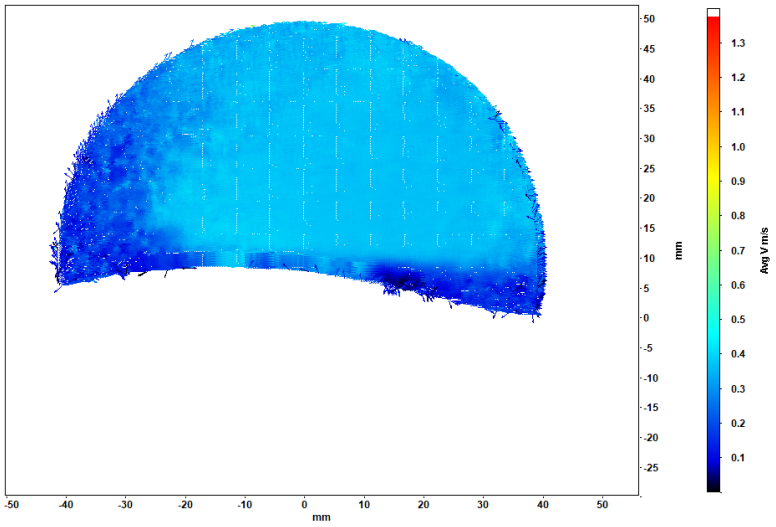

Figure 105. PIV Vector Image of Scaled Airfoil with SAVGJ Array at 60% Chord, 0° Angle of Attack, and 30,000 Reynolds Number

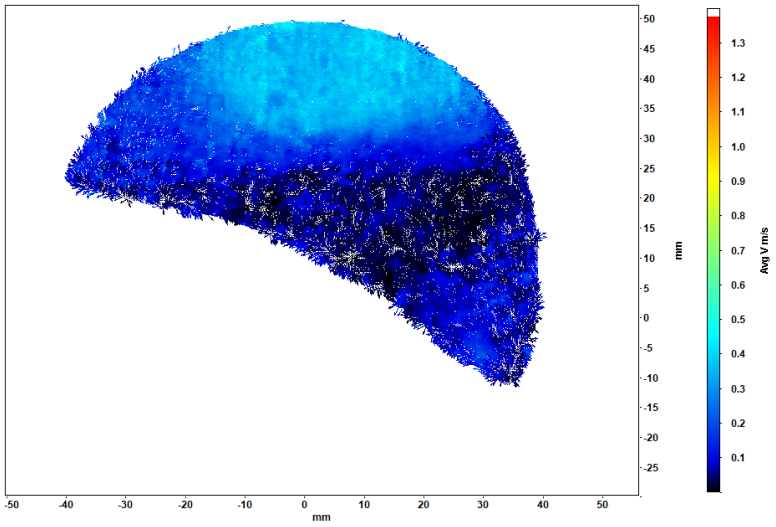

Figure 106. PIV Vector Image of Scaled Airfoil with SAVGJ Array at 60% Chord, 15° Angle of Attack, and 30,000 Reynolds Number

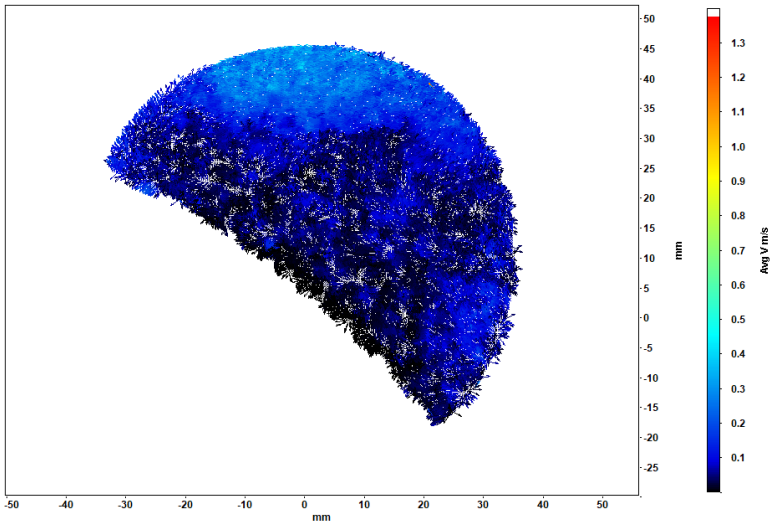

Figure 107. PIV Vector Image of Scaled Airfoil with SAVGJ Array at 60% Chord, 30° Angle of Attack, and 30,000 Reynolds Number

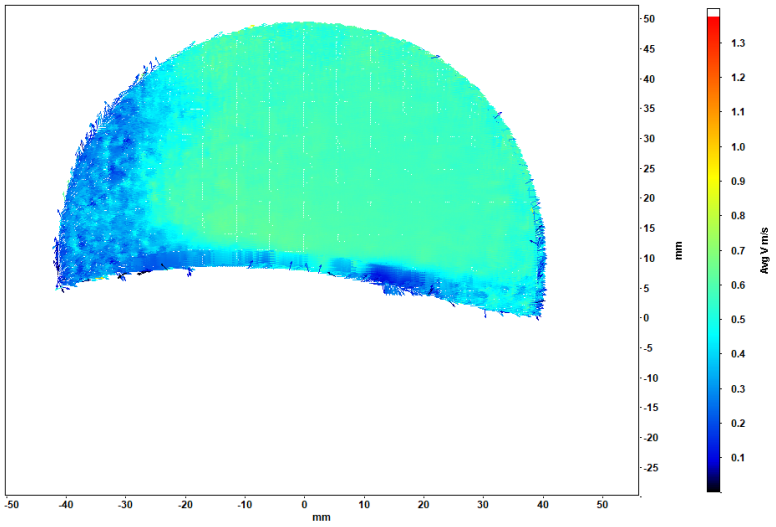

Figure 108. PIV Vector Image of Scaled Airfoil with SAVGJ Array at 60% Chord, 0° Angle of Attack, and 45,000 Reynolds Number

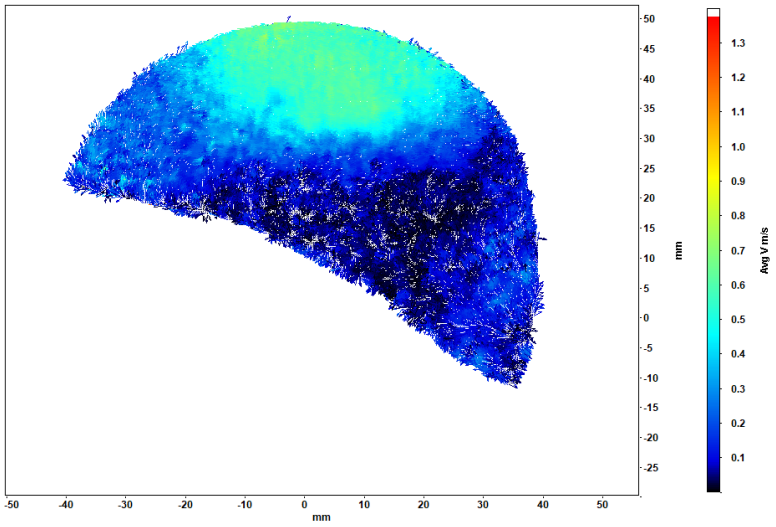

Figure 109. PIV Vector Image of Scaled Airfoil with SAVGJ Array at 60% Chord, 15° Angle of Attack, and 45,000 Reynolds Number

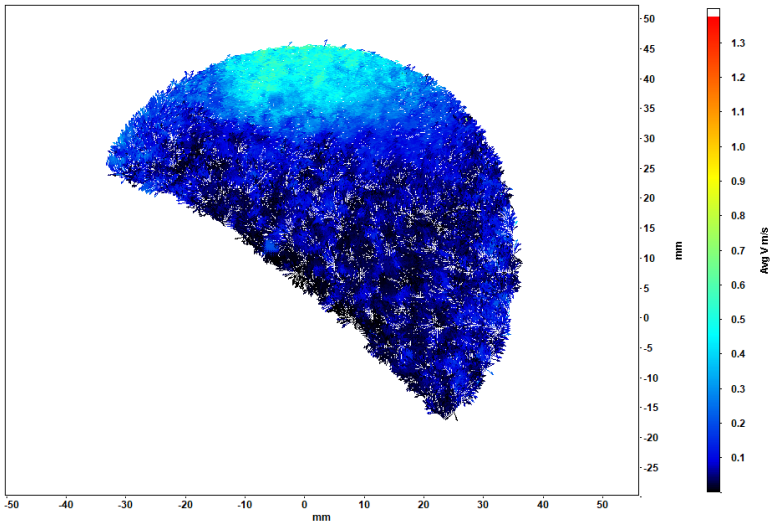

Figure 110. PIV Vector Image of Scaled Airfoil with SAVGJ Array at 60% Chord, 30° Angle of Attack, and 45,000 Reynolds Number

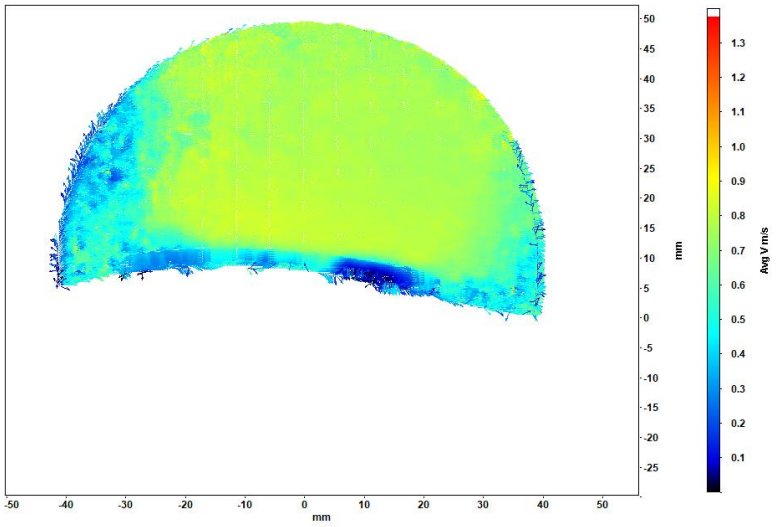

Figure 111. PIV Vector Image of Scaled Airfoil with SAVGJ Array at 60% Chord, 0° Angle of Attack, and 60,000 Reynolds Number

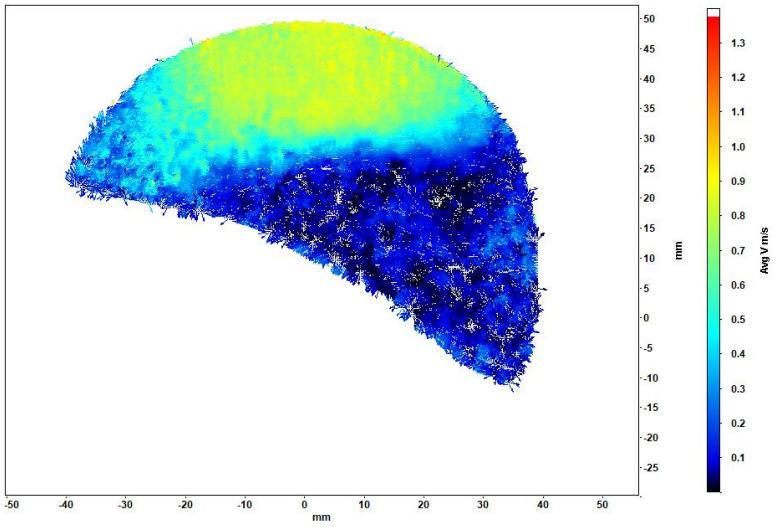

Figure 112. PIV Vector Image of Scaled Airfoil with SAVGJ Array at 60% Chord, 15° Angle of Attack, and 60,000 Reynolds Number

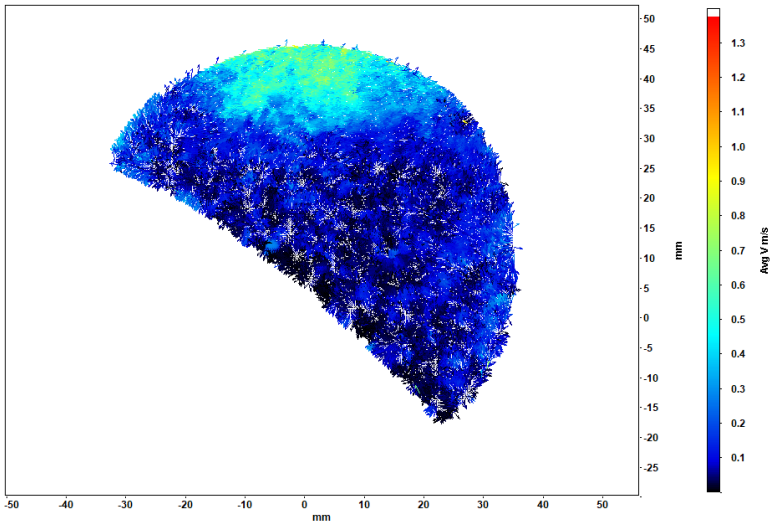

Figure 113. PIV Vector Image of Scaled Airfoil with SAVGJ Array at 60% Chord, 30° Angle of Attack, and 60,000 Reynolds Number

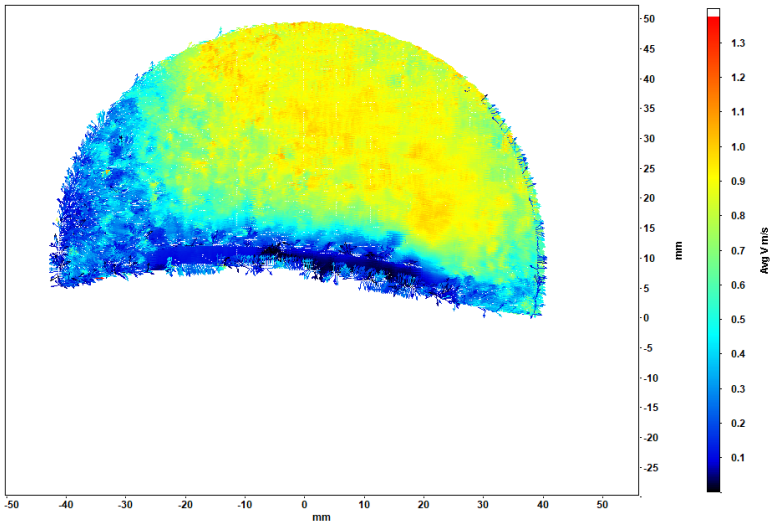

Figure 114. PIV Vector Image of Scaled Airfoil with SAVGJ Array at 60% Chord, 0° Angle of Attack, and 75,000 Reynolds Number

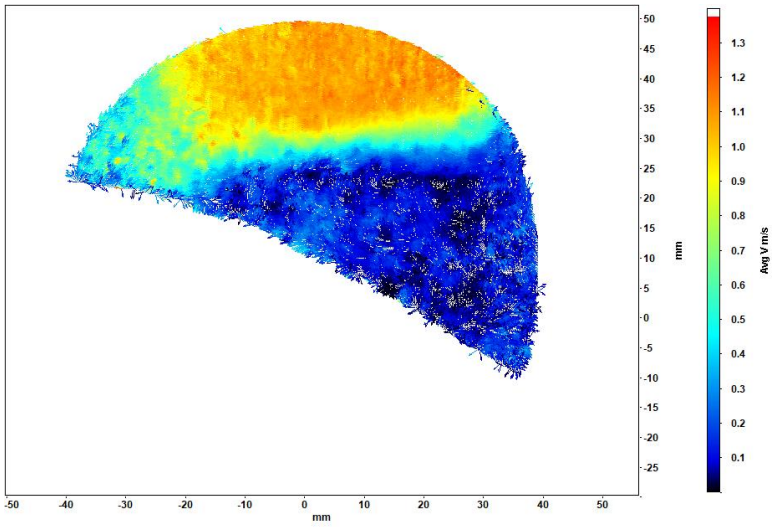

Figure 115. PIV Vector Image of Scaled Airfoil with SAVGJ Array at 60% Chord, 15° Angle of Attack, and 75,000 Reynolds Number

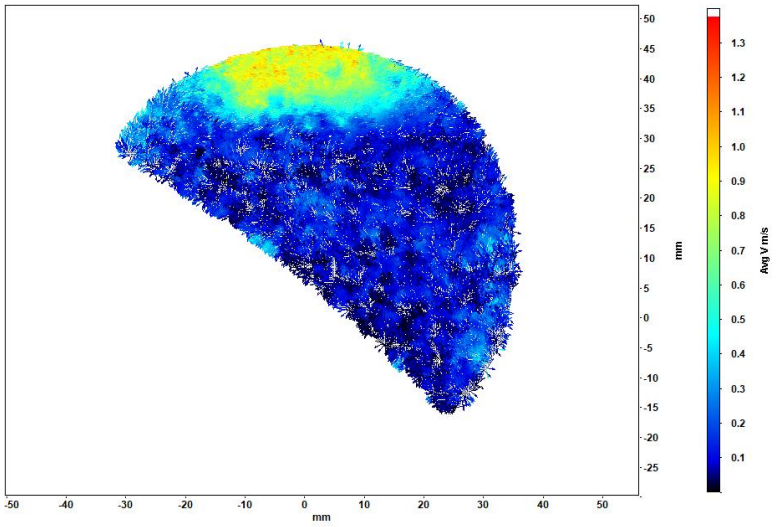

Figure 116. PIV Vector Image of Scaled Airfoil with SAVGJ Array at 60% Chord, 30° Angle of Attack, and 75,000 Reynolds Number

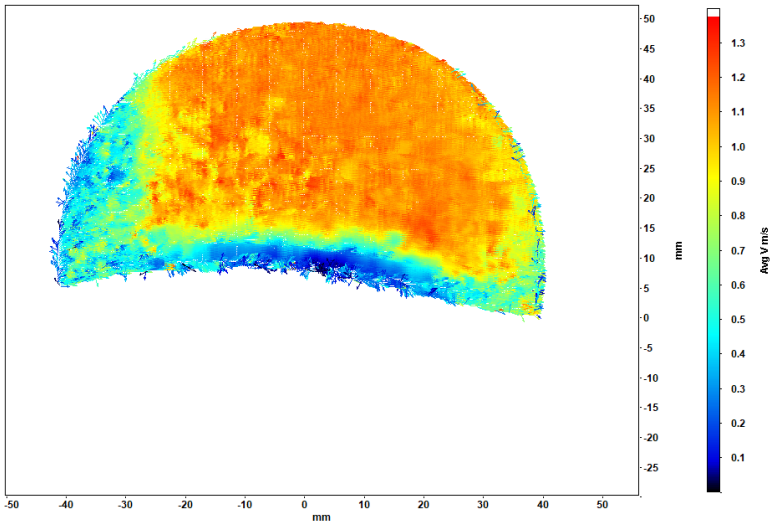

Figure 117. PIV Vector Image of Scaled Airfoil with SAVGJ Array at 60% Chord, 0° Angle of Attack, and 90,000 Reynolds Number

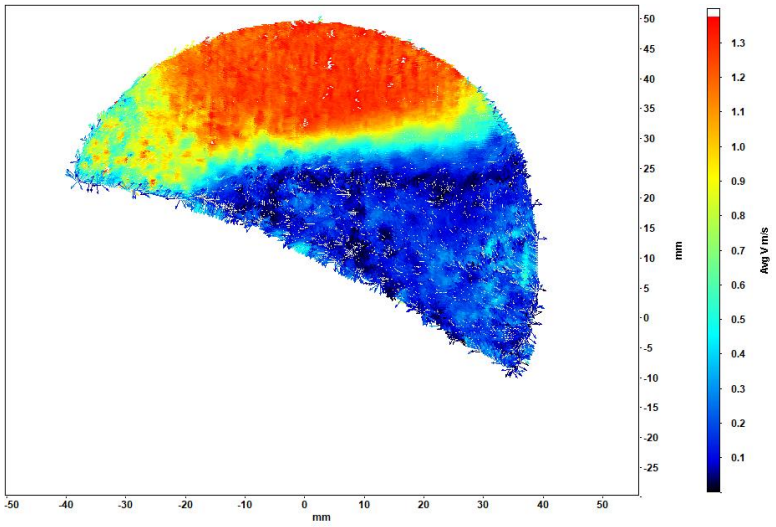

Figure 118. PIV Vector Image of Scaled Airfoil with SAVGJ Array at 60% Chord, 15° Angle of Attack, and 90,000 Reynolds Number

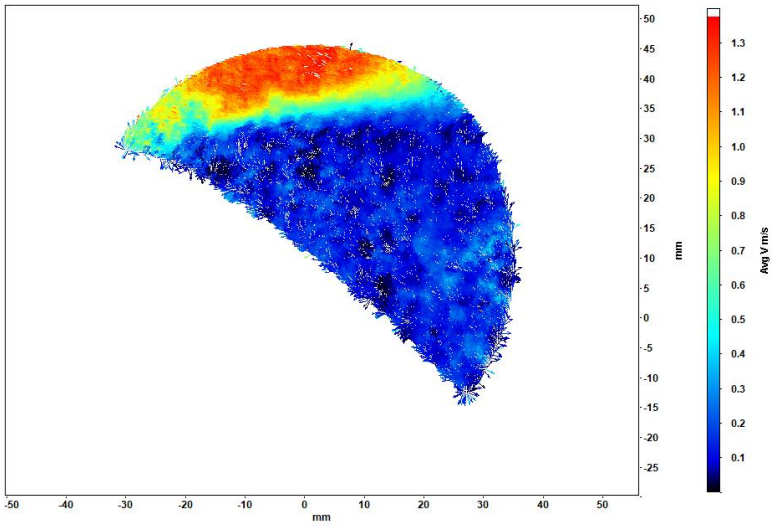

Figure 119. PIV Vector Image of Scaled Airfoil with SAVGJ Array at 60% Chord, 30° Angle of Attack, and 90,000 Reynolds Number

APPENDIX B – Matlab Code

```
% SAVGJ Design Program
% Drew Bellcock

% Inputs:
d_prop=10;              % propeller diameter (in)
pitch=5;                % propeller pitch (in)
chord=0.67;             % propeller chord (in)
alpha_stall=14;         % airfoil stall angle (deg)

v_inf=30;               % freestream velocity (m/sec)
rpm=8000;               % rotational speed (rpm)

rho=1.225;                % density of air (kg/m^3)
mu=1.81*10^-5;          % kinematic viscousity of air (kg/m*sec)

% Calculations:
d_prop=d_prop*0.0254;    % convert to m
chord=chord*0.0254;      % convert to m
r_prop=d_prop/2;        % calculate radius (m/sec)
r_prop=linspace(0,r_prop);      % descritize radius
omega=rpm/60;                   % convert to rot/sec
v_rot=omega*r_prop;          % calculate rotational velocity along the
radius (m/sec)
v_tot=sqrt(v_inf^2+v_rot.^2);   % calculate total velocity along radius
(m/sec)
Re_tot=(rho*chord*v_tot)/mu;    % calculate Reynolds number along
radius
J=v_inf/(omega*d_prop);       % calculate advance ratio along radius
alpha_tot=atan2d(v_rot,v_inf);        % calculate total angle of attack
pitch_angle=atan2d(pitch*pi*r_prop,2);       % calculate pitch angle
along radius (deg)
alpha_rel=pitch_angle-alpha_tot;                % calculate relative
angle of attack (deg)
[max_alpha_rel,max_alpha_rel_chord]=max(alpha_rel);     % max relative
angle of attack (deg), chord loc (%)
sep_chord_loc=(100-15)*(Re_tot-15000)./(90000-15000);   % calculate
flow separation chord location

for i=1:100
    % separation only at high AoA:
    if alpha_rel(i)<alpha_stall-0.1
        sep_chord_loc(i)=sep_chord_loc(i)-10;
    else
        if alpha_rel(i)<alpha_stall-0.5
            sep_chord_loc(i)=sep_chord_loc(i)-5;
        else
            if alpha_rel(i)<alpha_stall
                sep_chord_loc(i)=sep_chord_loc(i);
            end
        end
    end
    % adjust domain of chord location:
    if sep_chord_loc(i)>=100
        sep_chord_loc(i)=100;
```

```
    else
        if sep_chord_loc(i)<=06
            sep_chord_loc(i)=0;
        end
    end
    % define jet array locations:
    if sep_chord_loc(i)>=10
        jet_chord_loc(i)=sep_chord_loc(i);
        offset(i)=i;
    end
end

% define other jet parameters:
D_jet=0.002;                % jet diameter (m)
A_jet=D_jet*pi/4;           % jet area in m^2
s_jet=2.5;                  % set jet spacing
d_jet=D_jet*s_jet;          % calculate adjacent jet distance (m)
[~,n]=size(jet_chord_loc);  % measure number of eligible jet locations
jet_chord_loc=linspace(jet_chord_loc(1),jet_chord_loc(n),(jet_chord_loc
(n)-jet_chord_loc(1))/s_jet+1)/100*chord;    %create chord locations
(m)
[~,m]=size(jet_chord_loc);
k=find(sep_chord_loc);
k_min=min(k);
k_max=max(k);
array_angle=atan2d(jet_chord_loc(m)-jet_chord_loc(1),k_max-k_min)
```

VITA

Andrew C. Bellcock

Candidate for the Degree of

Master of Science

Thesis: SELF-ASPIRATED VORTEX GENERATOR JET APPLICATION FOR PROPELLER BOUNDARY LAYER SEPARATION SUPPRESSION

Major Field: Mechanical and Aerospace Engineering

Biographical:

Education:

Completed the requirements for the Master of Science/Arts in Mechanical and Aerospace Engineering at Oklahoma State University, Stillwater, Oklahoma in May, 2018.

Completed the requirements for the Bachelor of Science/Arts in Mechanical Engineering at Oklahoma Christian University, Edmond, Oklahoma in 2016.

Experience:

3D Processes Intern, Dasault Falcon Jet, Little Rock, Arkansas in 2014
Manufacturing Technology Intern, Niagara Bottling, Dallas, Texas in 2015
Manufacturing Technology Intern, Niagara Bottling, Ontario, California in 2016
Ignition Developer, Niagara Bottling, Ontario, California in 2016/2017
Graduate Research Assistant, Oklahoma State University, Stillwater, Oklahoma in 2017/2018

Professional Memberships:

American Society of Mechanical Engineers (ASME)
American Institute of Aeronautics and Astronautics (AIAA)
Society of Automotive Engineers (SAE)